SYNTHESIS, CHARACTERIZATION AND EVALUATION OF SKIN TISSUE ENGINEERING POTENTIAL OF POLY(LACTIC ACID)-NANOCLAY COMPOSITE SCAFFOLDS DOPED WITH VARIOUS BORON COMPONENTS

ÇEŞİTLİ BOR BİLEŞENLERİ İLE KATKILANDIRILMIŞ POLİ(LAKTİK ASİT)-NANOKİL KOMPOZİT DOKU İSKELELERİNİN SENTEZİ, KARAKTERİZASYONU VE DERİ DOKU MÜHENDİSLİĞİ POTANSİYELİNİN DEĞERLENDİRİLMESİ

Sara ASGHARI DILMANI

Supervisor

Prof. Dr. Menemşe GÜMÜŞDERELİOĞLU

Submitted to Graduate School of Science and Engineering of Hacettepe University as a Partial Fulfillment to the Requirements for the Award of the Degree of Master of Science in Bioengineering

2023

ABSTRACT

SYNTHESIS, CHARACTERIZATION AND EVALUATION OF SKIN TISSUE ENGINEERING POTENTIAL OF POLY(LACTIC ACID)-NANOCLAY COMPOSITE SCAFFOLDS DOPED WITH VARIOUS BORON COMPONENTS

Sara ASGHARI DILMANI

Master Degree, Department of Bioengineering

Supervisor: Prof. Dr. Menemşe GÜMÜŞDERELİOĞLU

January 2023, 118 pages

This study aims to investigate the characteristic features of boron (B) and nanoclay containing micro/nanocomposites and their effect on the normal human dermal fibroblast (NHDF) cells as a potential material to be used as a wound dressing. In the first part of this study, hybrid composites were fabricated by solvent-casting and electrospinning, and the impact of fabrication methods on resulting scaffolds was investigated. In this regard, montmorillonite (MMT) was modified with trimethyl octadecyl ammonium bromide (TMOD) as a quaternary ammonium salt. Then, B compounds, boron nitride (BN), zinc borate (ZB), or phenylboronic acid (PBA) were adsorbed on organomodified MMT (OMMT), and poly(lactic acid) (PLA) based PLA-OMMT/B hybrid composites were fabricated by solvent-casting and electrospinning. Modification of MMT nanoparticles with TMOD occurred through an ion-exchange reaction, leading to a series of critical changes in characteristic properties of the resulting composite: better distribution,

enhanced mechanical and thermal properties, faster biodegradation, and higher crystallinity. Although the modification of MMT improved the overall properties of hybrid composites produced by both fabrication methods, electrospun scaffolds demonstrated superior characteristics to solvent-cast membranes. Consequently, fibrous scaffolds were chosen for antibacterial tests and cell culture studies. Scaffolds containing OMMT in their structure exhibited dramatic inhibition against gram-positive bacteria. Moreover, hybrid composites with ZB and PBA demonstrated both bacteriostatic and bactericidal effects for gram-positive *Staphylococcus aureus* (*S. aureus*) and gram-negative *Escherichia coli* (*E. coli*). The 100%, 50%, and 25% (v/v) extracts of the PLA-OMMT scaffolds showed a modest cytotoxic effect on the NHDFs at the second-day culture that probably originated from TMOD. These results were evaluated as PLA-OMMT/B scaffolds, thanks to their antibacterial, morphological, and chemical properties can be used as a wound dressing that supports the early stages of wound healing, where it will show limited interaction with cells.

In the second part of this study, BN, ZB, and PBA were adsorbed on neat MMT, and PLA-based MMT/B micro composites were fabricated by electrospinning. The incorporation of neat MMT into the polymer matrix not only enhanced thermal properties and water uptake capacity but also led to the generation of porous nanofibers with antibacterial effects against *S. aureus*. The composites with BN, ZB, and PBA demonstrated bacteriostatic effects against both *E. coli* and *S. aureus*. *In-vitro* cell culture studies performed with NHDF indicated the non-toxic effect of utilized B compounds. The scanning electron microscope (SEM) and live/dead staining of cell-containing scaffolds showed that the incorporation of MMT supported cell adhesion and proliferation, and the further addition of B compounds, especially PBA, increased cell viability for 14 days. The cells retained their healthy morphology and viability in all groups, meaning that functionalized fibrous scaffolds were suitable for skin tissue engineering applications.

Keywords: Boron compounds; montmorillonite; poly(lactic acid); wound dressing; antibacterial characteristics.

ÖZET

ÇEŞİTLİ BOR BİLEŞENLERİ İLE KATKILANDIRILMIŞ POLİ(LAKTİK ASİT)-NANOKİL KOMPOZİT DOKU İSKELELERİNİN SENTEZİ, KARAKTERİZASYONU VE DERİ DOKU MÜHENDİSLİĞİ POTANSİYELİNİN DEĞERLENDİRİLMESİ

Sara ASGHARI DILMANI

Yüksek Lisans, Biyomühendislik Bölümü

Tez Danışmanı: Prof. Dr. Menemşe GÜMÜŞDERELİOĞLU

Ocak 2023, 118 sayfa

Bu çalışmada, bor (B) ve nanokil içeren mikro/nano kompozitlerin karakteristik özelliklerinin ve bu kompozitlerin yara örtüsü olarak kullanım potansiyelinin normal insan dermal fibroblast (NHDF) hücreleri üzerindeki etkisinin incelenmesi amaçlanmıştır. Tez çalışmasının ilk aşamasında, çözücü-döküm ve elektroeğirme yöntemleriyle hibrit kompozitler üretilmiş ve üretim yöntemlerinin kompozit yapılar üzerindeki etkisi incelenmiştir. Bu amaçla, montmorillonit (MMT), kuaterner amonyum tuzu olan trimetil oktadesil amonyum bromür (TMOD) ile modifiye edilmiştir. Daha sonra organomodifiye MMT (OMMT) üzerine B bileşikleri olan boron nitrür (BN), çinko borat (ZB) veya fenilboronik asit (PBA) adsorbe edilmiş ve poli(laktik asit) (PLA) temelli PLA-OMMT/B hibrit kompozitler çözücü-döküm ve elektroeğirme yöntemleri ile üretilmiştir. Montmorillonit nanoparçacıklarının TMOD ile modifikasyonu iyon değişim reaksiyonu ile gerçekleşmiş ve elde edilen kompozitte nanopartiküllerin daha iyi dağılması, gelişmiş mekanik ve termal özellikler, daha hızlı biyobozunurluk ve yüksek kristalinite gibi karakteristik özelliklerde anlamlı değişikliklere yol açtığı görülmüştür. Montmorillonitin modifikasyonu her iki fabrikasyon yönteminde de üretilen hibrit kompozitlerin genel özelliklerini iyileştirmesine rağmen, elektroeğirme ile üretilen fıbroz iskelelerin çözücü-döküm yöntemi ile üretilen membranlara göre üstün özellikler

sergilediği görülmüştür. Sonuç olarak, antibakteriyel testler ve hücre kültürü çalışmaları için fibroz doku iskeleleri seçilmiştir. Yapılarında OMMT içeren nano kompozitler, gram-pozitif bakterilerde inhibisyon etkisi göstermiştir. Ayrıca, ZB ve PBA içeren hibrit kompozitler hem gram-pozitif *Staphylococcus aureus* (*S. aureus*), hem de gram-negatif *Escherichia coli* (*E. coli*) bakterilere karşı bakteriyostatik ve bakterisidal etkiler göstermiştir. Sitotoksisite testinin ikinci gününde PLA-OMMT doku iskelelerinin hacimce %100, %50 ve %25 ekstraktları, NHDF hücreleri üzerinde TMOD'den kaynaklanması muhtemel orta düzeyde sitotoksik etki göstermiştir. Bu sonuçlar, PLA-OMMT/B iskelelerinin sahip oldukları antibakteriyel, morfolojik ve kimyasal özellikleri sayesinde, hücrelerle sınırlı etkileşim göstereceği, yara iyileşmesinin erken aşamalarını destekleyen yara örtüsü olarak kullanılabileceği şeklinde değerlendirilmiştir.

Çalışmanın ikinci bölümünde, B'un hücreler üzerindeki etkisini gözlemleyebilmek için BN, ZB ve PBA, modifiye edilmemiş MMT üzerine adsorbe edilmiş ve elektroeğirme yöntemi kullanılarak gözenekli fiber morfolojisine sahip PLA-MMT/B doku iskeleleri üretilmiştir. Modifiye edilmemiş MMT polimer matrisin termal özelliklerini ve su alma kapasitesini arttırmanın yanı sıra *S. aureus'a* karşı antibakteriyel etki göstermiştir. Yapılarında BN, ZB ve PBA içeren kompozitler hem *E. coli* hem de *S. aureus* için bakteriyostatik etki göstermiştir. Normal insan dermal fibroblast hücreleri ile yapılan *in-vitro* hücre kültürü çalışmaları kullanılan bor bileşiklerinin herhangi bir toksik etki yaratmadığını göstermiştir. Taramalı elektron mikroskobu (SEM) ve canlı/ölü boyama sonuçları MMT içeren kompozitlerin hücre yapışmasını ve çoğalmasını desteklediğini ve ayrıca B bileşiklerinin, özellikle PBA'nın eklenmesi ile 14 gün boyunca hücre canlılığını arttırdığını göstermiştir. Hücreler, sağlıklı morfolojilerini ve canlılıklarını tüm gruplarda korumuş ve bu durum üretilen fibröz iskelelerin deri doku mühendisliği uygulamalarında kullanılabileceğini göstermiştir.

Anahtar Kelimeler: Bor bileşikleri; montmorillonit; polil(aktik asit); yara örtüsü; antibakteriyel özellikler.

ACKNOWLEDGEMENTS

I would like to express my sincere gratitude toward my supervisor Prof. Dr. Menemşe GÜMÜŞDERELİOĞLU for her endless compassion, support, encouragement, and guidance. I have learned a lot under her supervision during my studies. It has been a great honor and pleasure to be her student.

I wish to thank all the members of Cell and Tissue Engineering Research Group for their kindness, understanding, and assistance. Special thanks to Dr. Özge Ekin Akdere for sharing her experience with me, and Sena KOÇ for her contribution and help during the whole process. I would like to thank Dr. Ülkü BOZOĞLU from the bottom of my heart for her unlimited kindness, understanding, and support. Thanks to her, I never felt lonely during this challenging process.

There is no word to describe how thankful I am to be a part of my family and how delightful and grateful I am to have them. My dear mother and father, my sister and her beloved son who encouraged me even though I was far from them, my brother who guided and supported me by all means, her lovely wife who helped me during exams and became a dear friend to me, my uncle and his precious wife and their adorable children who are my second family, I cannot explain how valuable they are to me, I am eternally grateful for your existence in my life.

TABLE OF CONTENT

LIST OF TABLES

LIST OF FIGURES

SYMBOLS AND ABBREVIATIONS

Symbols

$AgNO_3$	Silver nitrate
AgBr	Silver bromide
CO_2	Carbon dioxide
NaOH	Sodium hydroxide
T_g	Glass transition temperature
T_m	Melting temperature
Br^-	Bromine ion
OH^-	Hydroxyl ion
-OH	Hydroxyl group
Na^+	Sodium ion
Ca^{2+}	Calcium ion
Zn^{2+}	Zinc ion
MPa	Mega Pascal
°C	Degree Celsius
°	Degree
v/v	Volume per volume
w/v	Weight per volume
w/w	Weight per weight

Abbreviations

ATR-FTIR	Attenuated Total Reflectance -Fourier Transform Infrared Spectroscopy
CEC	Cation Exchange Capacity
SEM	Scanning Electron Microscope

CTEM	Contrast Transmission Electron Microscopy
DSC	Differential Scanning Calorimetry
TGA	Thermogravimetric Analyses
PLA	Poly(lactic acid)
B	Boron
BN	Boron Nitride
ZB	Zinc Borate
PBA	Phenylboronic Acid
MMT	Montmorillonite
OMMT	Organomodfied Montmorillonite
TMOD	Trimethyl Octadecyl Ammonium Bromide
ECM	Extracellular Matrix
NHDF	Normal Human Dermal Fibroblast
TCPS	Tissue Culture Polystyrene
PBS	Phosphate-Buffered Saline
FDA	Food and Drug Administration
UV	Ultra Violet
ROS	Reactive Oxygen Species
HFIP	1,1,1,3,3,3-Hexafluoro-2-Propanol
MTT	3-[4, 5-dimethylthiazol-2-yl]- diphenyltetrazolium bromide
VEGF	Vascular Endothelial Growth Factor
MDGF	Macrophage-Derived Growth Factor
TNF-α	Tumor Necrosis Factor
HSP 70	Heat-Shock Proteins
FBS	Fetal Bovine Serum
DMEM-HG	Dulbecco's Modified Eagle's Medium-High Glucose

DMEM-LG	Dulbecco's Modified Eagle's Medium-Low Glucose
3D	3-Dimensional
pH	Potential Htydrogen
T	Tetrahedral
O	Octahedral
cmol	centimol
meq	milliequivalent
µg	Microgram
mg	Milligram
kg	Kilogram
h	Hour
J	Joule
µL	Microliter
mL	Milliliter
nm	Nanometre
µm	Micrometre
cm	Centimetre
mm	Milimetre
min	Minute

1. INTRODUCTION

With its distinctive layered structure, skin tissue fulfills vital duties, including physical protection and thermal regulation. Wounding endangers the integrity of skin tissue, making the body vulnerable to microorganism invasion. Since survival is the priority of the human body, the healing cascade is based on repair rather than regeneration. To shift the healing process from reparative to regenerative, novel dressings are needed to support the process as much as possible (Gurtner et al. 2008).

Researchers have made endeavors to fabricate ideal dressings for wound treatment. The type of dressing for wound treatment is determined by the sort, depth, location, extent, amount of exudate, infection, and adhesion of the wound. Currently, conventional dressings, e.g., gauzes, and smart dressings, e.g., hydrogels and hydroconductive dressings, have been used in clinical practice. However, traditional dressings mentioned face a number of problems that need to be addressed, such as the reduction of barrier properties after adsorbing exudate and the inability to initiate tissue regeneration. The application of nanomaterials is a promising approach for fabricating wound dressings with acceptable costs and effectiveness. Nanomaterial-incorporated composites have remarkable benefits in wound care owing to their high surface-to-volume ratio, antibacterial properties, and exceptional physical and chemical properties (Zeng et al. 2022). Moreover, the incorporation of more than one nanomaterial with distinct properties in a polymer matrix leads to the formation of hybrid composites with multiple functionalities.

Boron (B) is a metalloid known to be helpful, perhaps vital, for animals and even humans, especially for the healthy growth and maturation of bones. Besides its favorable impact on the human body metabolism and cell membrane maintenance, B and its derivatives were reported to be beneficial during the healing process of the wound, accelerating the cascade by affecting the production of extracellular matrix (ECM) (Białek et al. 2019). Montmorillonite (MMT) is one of the cationic clay minerals used since ancient times for wound treatment due to its homostatic effect. Moreover, MMT is one of the most

commonly employed nanomaterials used as fillers in the polymer matrix to enhance the physical and mechanical properties of the neat polymer, such as mechanical properties (Mousa et al. 2018). Moreover, some clay nanoparticles, including MMT, have high cation exchange capacity, which can be used for the organomodification of the clay compounds where exchangeable intralayer cation got replaced by a different substrate (cationic or without any charges). The resulting modified nanoclay possesses completely different properties compared to the initial clay mineral e.g., being organophilic rather than hydrophilic. Based on the type of substrate chosen for clay modification, interesting unique properties (e.g., antibacterial properties) can be introduced to clay minerals.

Accordingly, within the scope of the presented study the production of hybrid composites that can accomplish the commitments of a conventional wound dressing material and support various stages of the wound healing cascade simultaneously by incorporation of nanoclay and different boron (B) compounds with distinctive properties was aimed. Nanoclay acted as a carrier for B compounds, and B-adsorbed nanoclays were doped into a polymer matrix. The distinction between modified and unmodified nanoclay minerals and resulting hybrid composites, as well as the impact of the production method on the characteristics of the obtained products, are among the variables studied in the present thesis. The present study sought to examine the characteristic features of B and nanoclay containing micro/nano composites and their effect on the normal human dermal fibroblast (NHDF) cells as a potential material to be used as a wound dressing.

2. GENERAL INFORMATION

The following contents give information about the wound healing process, updated information about developed dressings, and the compounds utilized in this thesis. Considering skin tissue's contact with the environment and the complexity of the process, the healing cascade turns into a challenge that makes a full recovery nearly impossible. Cells play a crucial role in this cascade to achieve regenerative tissue repair instead of physical closure of the lesion with scar formation. The role of wound dressing and the favorable effect of the chosen compounds in the healing cascade were discussed below. Finally, the fabrication methods and the purpose of the study were explained.

2.1. Skin Tissue

2.1.1. Structure and Functions

Injuries tend to happen in daily life, resulting in wound formation. A wound can be described as defects and fractions formed on the anatomical structure of the skin that causes tissue to malfunction (Velnar et al. 2009). The skin is the largest and the most external tissue of the mammal's body with a surface of approximately 2 m^2 and a mass equal to approximately 15% of the total weight of the human body, which acts like a physical barrier, preventing pathogens and harmful chemicals from entering the body. In addition, the skin is in charge of hydration, initialization of vitamin D synthesis, excretion, thermal regulations, self-healing, immune surveillance, and sensory detection in the body (Colwell et al. 2005; Dąbrowska et al. 2018). The skin can accomplish these functions due to its unique layered structure, which comprises of three main layers: the outermost thin epidermis, the underlying thick dermis, and the deeper, subcutaneous hypodermis layer (Figure 2.1.).

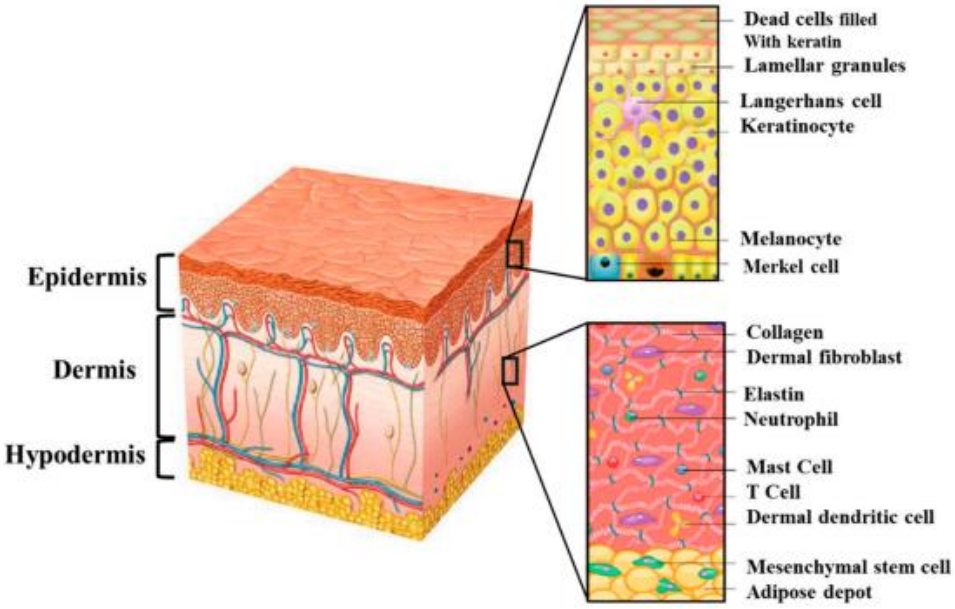

Figure 2.1. The structure of skin tissue (Tavakoli and Klar 2020).

The epidermis is the impervious barrier of the body that mainly consists of keratinocytes and melanocytes that can differentiate and form various strata of the epidermal lesion. Merkel cells and Langerhans cells are the remaining cells of the epidermal layer that provide the skin with sensory and immune system defense capabilities. The dermis, the thickest part of the skin, is formed from the connective tissue by fibroblasts embedded in the extracellular matrix (ECM). The skin tissue ECM consists of collagen I, glycosaminoglycans, and elastin that contributes to skin mechanical properties. Sweat glands, sebaceous glands, hair follicles, and blood vessels are other components of the dermal layer. The thickness of the dermis may differ according to the anatomical regions of the body. The hypodermis is the innermost layer of the skin tissue composed of adipose tissue contributing to thermoregulatory and mechanical properties of the skin (Tottoli et al. 2020).

2.1.2. Wound Formation, Classification and Healing Cascade

When a defect occurs in the skin tissue, the human body becomes vulnerable to environmental threats, causing different malfunctions depending on the depth and size of the injury hence the determination of treatment approach plays a crucial role in people's health care and life quality.

In order to function properly and maintain its integrity, the skin can quickly repair itself and remodel after an injury (Rousselle et al. 2019). However, not all wounds can heal automatically. Although there is no standard classification for wound types, the nature of the injuries causing the wounds, the length of the healing process, and the depth of injury to the skin and underlying tissues are the most important factors in wound classification (Percival 2002). Considering the time frame needed for a wound to heal, wounds can be classified as acute or chronic. When a wound is formed because of accidents, trauma, burns, and surgery, these wounds are considered acute wounds, which means the physical closure of the lesion and formation of a functional tissue occurs in an acceptable amount of time. When the wound closure exceeds the normal healing time frame and the entire healing cascade is elongated, wounds are considered chronic. Chronic wounds often withstand treatment attempts, and the newly established tissue's quality may not be the same as healthy tissue. In addition, functional closure may not occur (Whitney 2005). In general, the body reacts to an injury in three overlapping but distinguishable stages: inflammation, new tissue formation, and remodeling (Figure 2.2.).

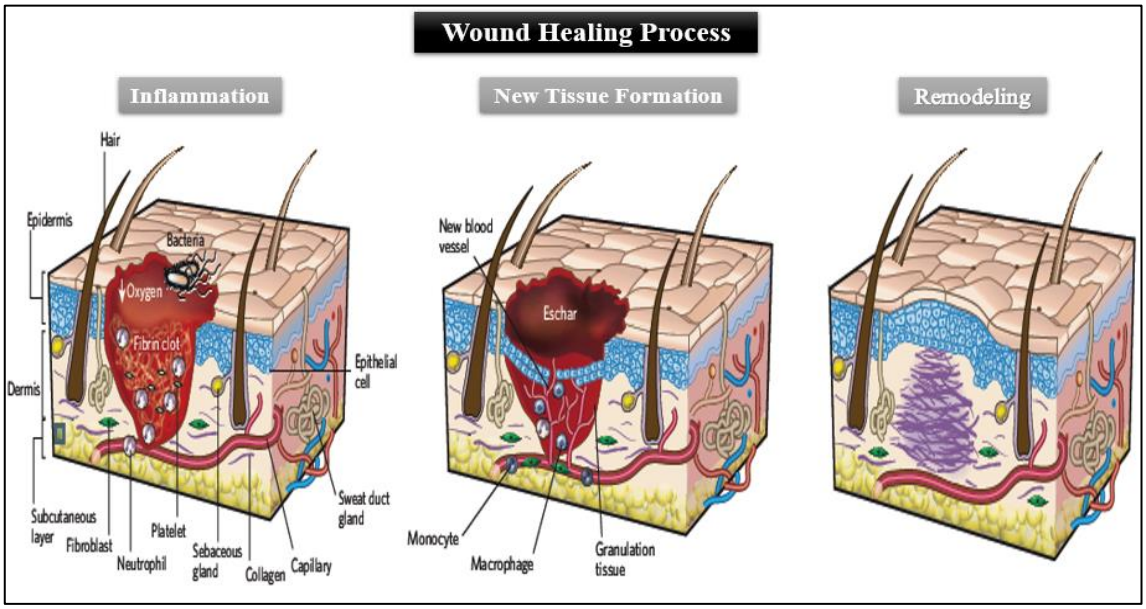

Figure 2.2. Mechanisms of normal wound healing (Gurtner et al. 2008).

The inflammation phase takes place instantly after injury and is known to be the first stage of wound repair. Coagulation and immune response must form to control blood and exudate loss, prevent infection and facilitate the disposal of dead tissue at wound lesions.

Platelet clot formation leads to hemostasis, followed by fibrin matrix establishment that serves as a barrier for cell leakage. A series of actions, such as degranulation of platelets, secretion of chemotactic signals by necrotic tissue, and generation of bacterial by-products activate the complementary system. Consequently, neutrophils got recruited at the wound lesion. As the final action of the inflammatory stage, 2-3 days after wound formation, monocytes emerge at the lesion and differentiate into macrophages, which coordinate all later occasions. Monocytes are accountable for fibrin phagocytosis activity, macrophage-derived growth factor (MDGF) secretion for fibroblasts and endothelial cells, and cellular debris (Kim et al. 2019).

New tissue formation takes place 2-10 days after tissue damage and is the second phase of wound repair. At this point, migration of various cells, cellular proliferation, and angiogenesis which means the formation of new blood vessels occur. If the lesion involves the dermis layer as well, keratinocytes migrate to the dermis and granulation tissue gets formed. The granulation tissue is a poorly differentiated and highly vascularized connective tissue. The mentioned tissue prepares a new lamella for migrated keratinocytes, containing cellular and fibrillar segments placed in an amorphous matrix. The fibroblasts, myofibroblasts (some fibroblasts engaged from the wound ledge or the bone marrow that are stimulated by macrophages, and differentiate into contractile cells that, over time, bring the edges of a wound together)(Gurtner et al. 2008; Opalenik and Davidson 2005), and endothelial cells constitute the cellular part of the granulation tissue. The majority of the mature scar's ECM consists of collagen, which is produced by interacted fibroblasts and myofibroblasts. The endothelial cells are responsible for angiogenesis (Tottoli et al. 2020). Recruitment of bone-marrow-derived endothelial progenitor cells can also lead to angiogenesis, but the extent of contribution is quite limited. The keratinocytes at the ledge of the wound proliferate and mature and, finally, revive the epithelium's impediment role (Gurtner et al. 2008).

Lastly, **remodeling** starts 2-3 weeks after damage and continues for at least a year. In this period of time previously activated actions get silenced and most of the endothelial cells, macrophages, and myofibroblasts undergo apoptosis, meaning a programmed cell death, or gets relocated from the wound lesion, leaving a mass containing few cells and

immature collagen type III and other ECM proteins. Interactions and constant feedback between the epidermis and dermis layers permit the successive regulation of continuity and homeostasis for skin tissue. Type III collagen and other acellular components of ECM are gradually replaced in 6–12 months by matrix metalloproteinases released by fibroblasts, macrophages, and endothelial cells, by means of strengthening the repaired tissue. At the end of remodeling, the ECM will consist of mature collagen type I, as it was before the injury (Gurtner et al. 2008; Tottoli et al. 2020). The healing cascade will proceed similarly for all organs, however, depending on diverse factors such as age, gender, and injured part of the body the speed of the healing process may vary (Op't Veld et al. 2020).

2.2. Classification of Conventional Wound Dressings

Mankind has used various types of natural materials to treat wounds since ancient times. Components such as water, milk, vinegar, and wine were used to clean the wounded area, and clay and honey were utilized to treat the wound. However, the first modern dressing was produced in the mid-1980s, which was able to control the humidity of the wounded area and absorb secreted fluids from the insulted area. Generally, conventional wound dressings that are used to treat the wound are expected to fulfill the following functions (Rezvani Ghomi et al. 2019):

- Manage the moistness around the wound area,
- Transmission of gases,
- Absorb excess discharge,
- Appropriate antibacterial activity,
- Reduce surface necrosis,
- Having proper barrier properties,
- Easily changed and removed,
- Biocompatible, biodegradable, and nontoxic,
- Reduce the pain as much as possible,
- Costly acceptable.

The type of dressings for wound treatment is determined by the sort, depth, location, extent, secreted exudate amount, bacterial invasion, and stickiness of the wound (Rezvani Ghomi et al. 2019). Many adverse factors may lead to belated wound healing that can extend the patient's affliction and pain, increasing the possibility of intricacies and effectively adding to healthcare costs. On most occasions, the healing process ends with scar formation; meaning the physical closure of the lesion, failing to fulfill the regular functions of the normal skin. Furthermore, despite its rigid appearance, the durability of the scar is less than healthy tissue. Such circumstances may increase the possibility of secondary injury in the same lesion (Op't Veld et al. 2020). Synthetic wound dressings such as hydrogels, tissue adhesives, foams, vapor-permeable films, alginates, and silicone meshes have been developed to produce a novel dressing that could respond to the requirements of an ideal wound dressing (Figure 2.3.). Some of the conventional dressings that are widely used worldwide to treat wounds are explained in detail in the following section.

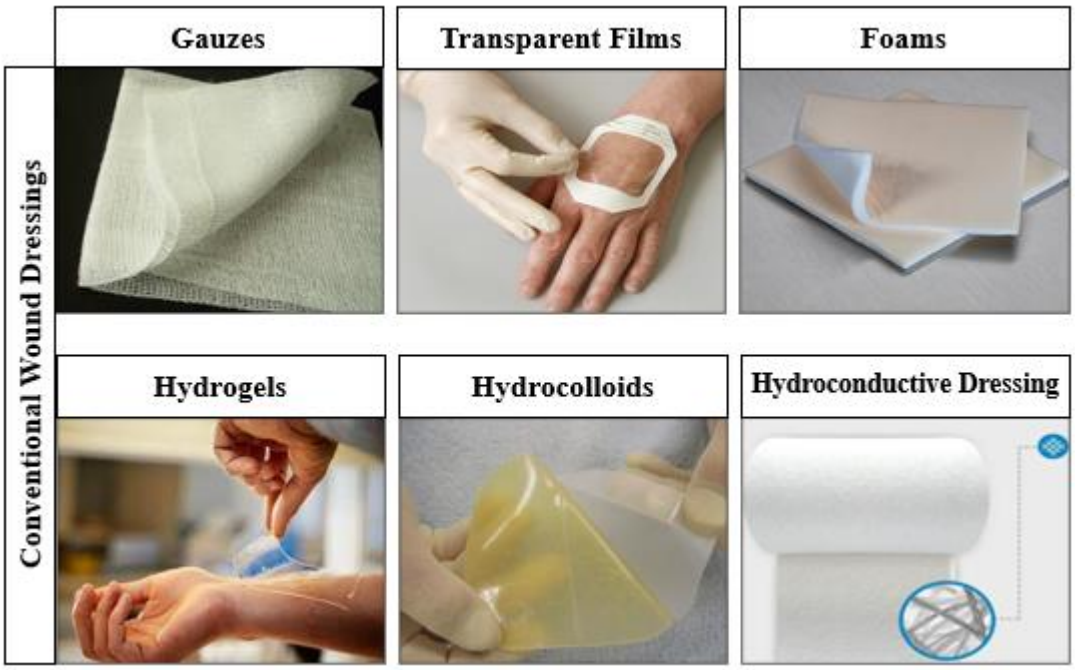

Figure 2.3. Some commonly used wound dressings in clinical practice.

2.2.1. Gauze Dressings

Gauzes are known to be the oldest conventional wound dressings which are inexpensive, available, and highly absorbent, used in clinical practice. They can serve as a physical barrier and compel early hemostasis. Moreover, they can be easily shaped to any defect form and wrap the highly-exudated wounds regardless of the infection condition of the lesion. However, gauzes are far from being an ideal wound dressing due to the following reasons: they can cause trauma, mechanical debridement, secondary injury, and distress upon removal, leave residues, activate the immune system, and cause severe wound infections due to the lack of antibacterial activity. Numerous attempts have been made to improve the functionality of gauzes. Wet-to-dry gauzes and gauzes with antibacterial, self-cleaning, and anti-adhesive functionality were developed. For wet-to-dry gauzes, mechanical debridement upon removal was controlled, and the bacterial growth was partly inhibited due to the presence of elements such as iodine, zinc, and bismuth for impregnated gauzes. However, numerous disadvantages followed the application of mentioned gauzes. Drawbacks such as vasoconstriction, increment in the affinity of hemoglobin to oxygen, hypoxia, causing pain due to removal in the dry state, cross-contamination, and not-selective debridement for wet-to-dry gauzes and toxicity and insufficient anti-microbial behavior for all loaded elements were reported (Laurano et al. 2022; Zeng et al. 2022).

2.2.2. Transparent Films

Transparent films evolved to overcome some of the shortcomings of gauze. The transparent films are applied and removed easily without causing any pain for the patient. During application, they cover the wounded area and prevent contamination while permitting gas exchange and visual inspection of the injured site. They are changed less frequently than gauze and tapes while providing a moist environment for the wound to heal. However, their low capacity for swelling limits their application for utility in infected or highly exudated wounds (Laurano et al. 2022). Moreover, in some cases, the fluid (exudate) could pool under transparent films and create a higher risk of infection. Thus, the utility of transparent films was not recommended as the existence of excess exudate centralized around the insulted area may support bacteria growth and hinder the healing cascade (Bernatchez 2014).

2.2.3. Foams

Foams have attracted great attention because of their remarkably high absorption ability. From this point, they are considered the opposite sort of dressings from transparent films. Gas exchange is permitted through foams while ensuring thermal insulation. The exchange frequency of foams is less than gauzes (they do not need changing for up to seven days if the wound is not infected). However, they need to be changed daily in case of infection (Seaman 2002).

Foams made from calcium salt and sodium alginic acid are called alginate dressings. The alginate dressings are developed from brown seaweed and can be found as nonwoven sheets and ropes, and can be used as flexible fibers, as well. Foremost characteristic of alginates is the absorption capability. Given their high porosity and non-adhesiveness, they can adsorb up to approximately twenty times their weight. Also, the calcium component acts as a hemostat and causes blood clotting. On the other hand, as they need humidity for productive implementation, they are inappropriate for utilization in non-exudated or moderate-exudated wounds. Moreover, alginates need a second layer to avoid drying the wound bed. If the wound gets infected, the mentioned second layer must be non-concealing (Rezvani Ghomi et al. 2019).

2.2.4. Hydrocolloids

Hydrocolloids are another group of dressings that are easily applied and stick sufficiently to the skin, consisting of a blend of colloidal materials with elastomers and alginates. The elastic matrix can be hydrophilic polymers, such as sodium carboxymethyl, cellulose, gelatin, pectin, and sodium alginate. The hydrocolloids have a series of advantages, such as biodegradability, biocompatibility, absorption of minimal to moderate amounts of exudate, prevention of water, bacterial, and oxygen penetration, and maintenance of moisture around the wound. Furthermore, hydrocolloids change the pH of the region towards the acidic range and promote the inhibition of bacterial proliferation, while ensuring the significant coverage of the site, therefore, there is no need for a secondary bandage. Consequently, hydrocolloids are proper for surface ulcers, minor burns, shock injuries, and bruises. Yet, their utility is limited for infected and deep wounds due to their

occlusive properties. Moreover, as they attach firmly to the wound, their removal may traumatize perilesional tissue. (Laurano et al. 2022; Rezvani Ghomi et al. 2019).

2.2.5. Hydroconductive Dressings

Hydroconductive dressings are specific multilayer structured dressings that can absorb exudate and remove debris and by-products of the wound away from the wound bed into their core (Sood et al. 2014). Some of the hydroconductive dressings are commercially available, characterized by high absorption capability, non-traumatic exchange, and the potency of maintaining their integrity for approximately up to a week. However, researchers have shown the potential of such dressings in entrapping the bacteria in their structure, pointing out their shortcomings in antibacterial properties. Although faster healing was observed for patients using hydroconductive dressings for treatment, the reason behind enhanced tissue regeneration was associated with faster removing of exudate rather than causing bacteria destruction (Robson et al. 2012). Therefore, hydroconductive dressings are more suitable to treat specific chronic wounds than other explained conventional dressings due to their distinct characteristics, however, they are far from being universally accepted as an ideal wound dressing.

2.2.6. Diagnostic Dressings

Despite all the effort and improvements achieved by developing various dressings explained before, the passive treatment situation makes it formidable to meet the dynamic requirements of wounds, especially chronic type, as there is no monitoring of the real wound status. The early detection of situations such as infection and their in-time treatment are of significant importance. Therefore, smart wound-dressing systems, which can cope with the “Black-Box” or “blind” condition of classical wound care by not only pro-regenerating properties but also real-time wound status monitoring, were developed. Novel dressings that are able to sense bacteria, pH, temperature, motion, physiological signals, glucose, ROS, and uric acid were produced (Lou et al. 2020; Pang et al. 2020). In spite of their unique benefits, the time-consuming and costly production method, inability to contribute to the absorption of exudate, and covering irregularly shaped wounds are considered to be the most important shortcomings of these dressings.

2.2.7. Hydrogels

Hydrogels are macromolecular three-dimensional (3D), mostly transparent networks with high swelling capacity that contain 70–90% water, consisting of hydrophilic but unsolvable substances often supplied as sheets or amorphous gels. Hydrogels manage the amount of moisture in the wound bed that accelerates the removal of the necrotic tissues and foreign materials, and provide significant pain relief by cooling the skin without sticking. Alterable chemical and physical characteristics, biocompatibility, biodegradability, hemostasis, drug or cell delivery, and barrier properties are other advantages of mentioned dressings (Op't Veld et al. 2020; Rezvani Ghomi et al. 2019). So, they can be used for the treatment of wounds with low to moderate amounts of exudates, such as burns, surgical wounds, skin tears, and pressure ulcers. Certain hydrogels have been designed for specific applications, some of which are described in the following part:

Hydrogels for sutureless wound closure: Hydrogels used as surgical sealants were reported to be more advantageous than traditional sutures as they are less time-consuming and easy to use, without causing secondary injury or discomfort when removed. For this purpose, adhesive hydrogels have been the focus of attention. Their outstanding adhesive ability is accompanied by excellent biocompatibility and biodegradability with a minimum inflammatory response (Ghobril and Grinstaff 2015). These features make them one step closer to being an ideal wound dressing and surgical sealant. Mussel-inspired and thermoresponsive hydrogels are examples of adhesive hydrogels. The majority of mussels bond firmly to rough or smooth substrates through covalent or noncovalent bonds, resulting in immediate attachment to the skin but can be easily sundered without causing additional complications (Lee et al. 2007). Thermoresponsive adhesive hydrogels are able to stick firmly to the skin surrounding the damaged area at the body temperature, closing the wound by applying force to pull the edges of wounds together. Although tissue adhesives are effective for wound closure, they can be painful to change and may demolish the wound repair process (Blacklow et al. 2019).

Antibacterial hydrogels: Antibacterial hydrogels can be: (i) hydrogels with natural antibacterial capability, (ii) antibacterial agent-containing hydrogels, and (iii) stimuli-

responsive antibacterial hydrogels. Hydrogels with natural antibacterial capability possess antibacterial components in their polymeric structure or associated by-products. These hydrogels are easy to produce with fewer drawbacks compared to the other systems because there are no auxiliary antibacterial substances. Antibacterial agent-containing hydrogels combat bacterial infections by agents like metal ions (e.g., Zn^{2+}, Fe^{3+}, and Ag^{+}), metallic nanoparticles, antibiotics, and natural extracts. Finally, the incorporation of nanomaterials into the three-dimensional structure of hydrogels has resulted in the emergence of stimuli-responsive antibacterial hydrogels that are induced by various factors, such as light or laser to cause an antibacterial response (Zhong et al. 2020).

Hemostasis supportive hydrogels: In the case of noncompressible bleeding or severe bleeding arising from aortic and visceral fractures, the application of hemostatic dressings is crucial and plays a vital role in rescuing the patients' life (Qiao et al. 2021). However, designing hemostatic materials is challenging due to the variable conditions of wounds, such as irregularity in the wound shape and depth. In this case, hydrogels are advantageous as they can be amorphous and reach deep wounds. Numerous nanomaterial-based hydrogels were evolved to achieve immediate hemostasis. As an example, a photoreactive hydrogel that was able to adhere firmly to a wet tissue surface under ultraviolet radiation and seal bleeding arteries and arterial hemorrhages was produced (Hong et al. 2019).

Angiogenesis supportive hydrogels: Angiogenesis is a crucial stage of the healing process. Without a proper blood supply, nutrition and oxygen cannot reach cells, and the healing process cannot be completed. To induce angiogenesis, multifunctional hydrogels have been developed, which are able to release VEGF constantly. In the presence of VEGF, enhanced endothelial cell growth, angiogenesis, and neovascularization in wound tissue can be achieved (Siebert et al. 2021). Another approach to induce angiogenesis through hydrogels is to use exosomes. Due to their favorable characteristics, such as storability, stability, and not initiating immune system responses, the design of multifunctional hydrogels is comparatively more manageable to encapsulating growth factors (Wang et al. 2019). One of the natural conditions that can promote angiogenesis in the wound tissue is heat. Therefore, hydrogels that were able to provide a desirable

atmosphere with an optimum high temperature around the wound lesion were designed to enhance the healing process (Sheng et al. 2021).

Hydrogels contain most of the features of an ideal dressing. Despite their many advantages, the need for a secondary protective layer due to their insignificant barrier property, as well as their disability to adsorb excessive exudate are among the main drawbacks of hydrogels.

2.3. Biomaterials for Wound Dressing Applications

2.3.1. Synthetic and Natural Polymers

Considering the complex demands of wound tissue, the development of an ideal dressing utilizing a single-component approach is unattainable. Hence, most current research is focused on fabricating composite materials by incorporating bioactive materials in polymeric bases. As a polymeric base natural polymers, such as alginate, chitosan, dextran, collagen, gelatin, hyaluronic acid, bacterial cellulose, etc., or synthetic polymers, such as poly (lactic-acid) (PLA), poly (D, L-lactide-co-glycolide) (PLGA), poly(vinyl alcohol) (PVA), poly(caprolactone) (PCL), poly (ethylene glycol) (PEG), etc. can be used to evolve composite materials (Fan et al. 2022). Thermoplastic polymers are commonly utilized substances for composite fabrication giving to their diversity, processability, molecular structure, and microstructural features, enabling the resulting composite to be functionalized with tunable chemical and physical properties depending on the type of fillers (González-Henríquez et al. 2019). Moreover, by utilizing more than one bioactive component, hybrid materials can be obtained, which are able to address more than one requirement simultaneously.

2.3.1.1. Poly(lactic acid) (PLA)

Among thermoplastic polymers, poly(lactic acid) (PLA) stands out as it is readily available, biobased, biodegradable, and biocompatible (Chong et al. 2022). Poly(lactic acid) is synthesized from lactide, a cyclic dimer obtained from controlled polymerization of lactic acid, which itself is provided from the fermentation of renewable resources, such as corn starch, tapioca roots, or sugarcane. The synthesis of PLA can result from two

reactions: ring-opening polymerization of lactide, and direct polycondensation of lactide (Figure 2.4.).

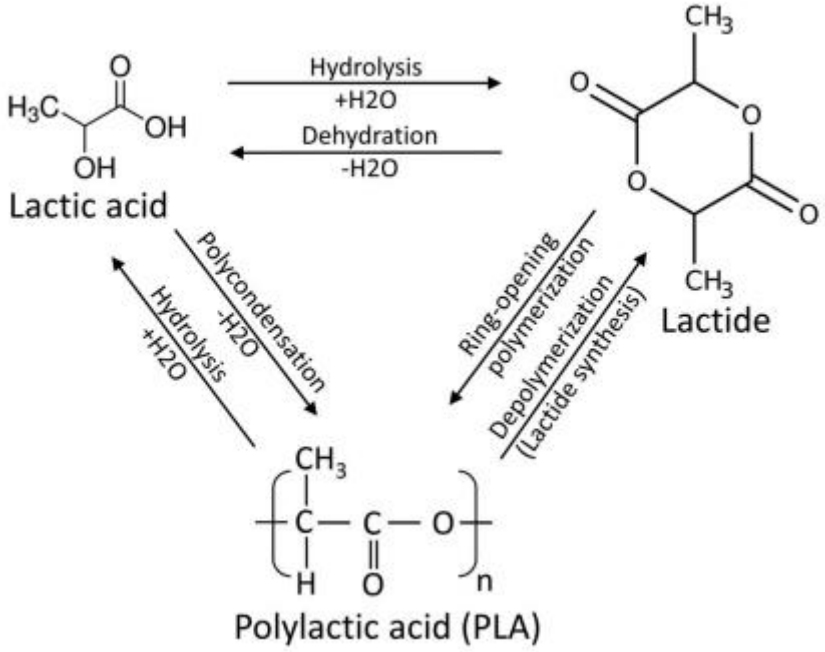

Figure 2.4. Polycondensation and ring-opening polymerization reactions to synthesize PLA (Sanusi et al. 2021).

Lactide has two chiral centers, so it can be found in two optically active stereoisomers: D-lactide and L-lactide. As a result, monomer of PLA is enantiomeric, having D- and L-isomers. The ratio of D-lactate to L-lactate units in PLA determines the final properties of polymer. For instance, PLA with D-lactide content more than 7% is amorphous with glass transition temperature (T_g) about 55 ºC. However, PLA homopolymer synthesized with absolute D-lactide or L-lactide is semicrystalline with T_g between 55-60 ºC (Sanusi et al. 2021).

Owing to its perfect transparency, durability, and adequate processability, PLA was used in beverage/food packaging, sporting goods, interior components, vehicular systems like aerospace and marine, and contact lenses as a promising alternative for petroleum-based commodities. Moreover, PLA-based products have been widely used in medical applications, such as surgical sutures, implants, controlled drug delivery systems, medical prostheses, tissue templates, wound dressings, and pharmaceutical compositions due to

their low toxicity. Despite mentioned advantages, PLA is extremely sensitive to environmental stress which leads to the brittleness of the polymer. In addition, even semicrystalline PLA frequently becomes amorphous after being processed due to its exceptionally slow crystallization and rapid cooling rate, which contributes to the brittleness of the PLA. In addition, for biomedical purposes, inadequate disinfection properties of pure PLA limit their widespread utility as it may be the source of infection. These factors make the modification of PLA necessary to improve the features of neat polymer for long-term application in various occupations (Chen et al. 2012; Chong et al. 2022; Sanusi et al. 2021).

2.3.2. Clay Nanoparticles

Clays have been defined as finely grained natural minerals that have been used for medical purposes since ancient times up until recent years. In traditional cultures, clays were used externally to cure various illnesses (Bergaya and Lagaly 2006).

Clay minerals are phyllosilicate or sheet silicates comprise of hydrated alumina–silicates, which include micas, chlorite, serpentine, and talc. Each layer of clay mineral is composed of tetrahedral silicates and octahedral hydroxide sheets. Different arrangements of tetrahedral and octahedral layers result in the formation of 1:1 and 2:1 classes of clay minerals. The 1:1 clay consists of one tetrahedral and one octahedral sheet, such as kaolinite and serpentine. On the other hand, 2:1 clay is comprised of an octahedral layer sandwiched between two tetrahedral layers. Smectite, chlorite, vermiculite, and montmorillonite are examples of 2:1 clay class. Furthermore, clays can be classified based on the metal ions present in octahedral sheets: dioctahedral and trioctahedral. Trioctahedral clays are formed with divalent metal ions, such as Fe^{2+} and Mg^{2+} ions, and dioctahedral clays are formed with trivalent metal ions, such as Al^{3+} ion (Gaskell and Hamilton 2014; Ghadiri et al. 2015).

Clay minerals are known for their ion exchange capacity, which primarily originates from positively or negatively charged layers of clay. In addition, the net charge of layers can be permanent structural changes caused by the isomorphous substitution of Al^{3+}, Si^{4+}, Mg^{2+}, and Fe^{3+} ions, or be pH-dependent, arising from surface reactivity and broken edges

of clay minerals. For 2:1 clay mineral, the pH-dependent charge constitutes less than 1% of the total net charge. However, for 1:1 clays that do not possess any charge due to ion substitution, the pH-dependent charge is the main contributor to the total net charge. Clays are divided into two groups considering the charge of the layers: (i) The cationic clay minerals that retain a negative charge on the layers and can be found easily in nature, and (ii) The anionic clay minerals or layered double hydroxides that retain a positive charge on the layers. The anionic clays are rather rare in nature but comparatively uncomplicated and can be synthesized easily by cost-effective methods (Ghadiri et al. 2015). Some of the commonly used cationic clay minerals and the applications fields of each are given in Figure 2.5.

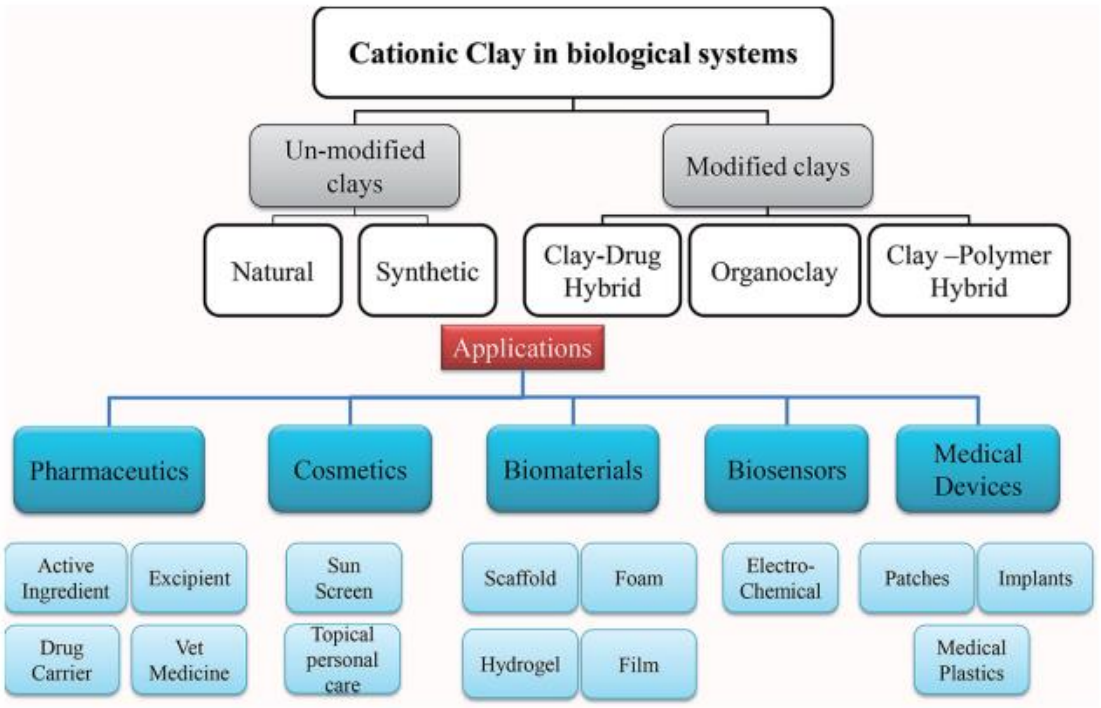

Figure 2.5. Modified and unmodified cationic clay minerals and their applications (Ghadiri et al. 2015).

2.3.2.1. Montmorillonite (MMT)

Montmorillonite (MMT) is a smectite clay mineral type of 2:1 with the half unit formula of $Na_m(Al_{2-m}Mg_m)Si_4O_{10}(OH)_2.nH_2O$, comprising of a double-layered siloxane tetrahedron and a single-layer aluminoxy octahedron with a unit layer spacing of about 1

nm (Figure 2.6.). The layers of the MMT possess an extreme negative charge because of isomorphous cation substitution in the tetrahedral (T) and/or octahedral (O) sheets of MMT. The charge equivalence is maintained by interaction with cations between the layers (Mousa et al. 2018; Yang et al. 2019).

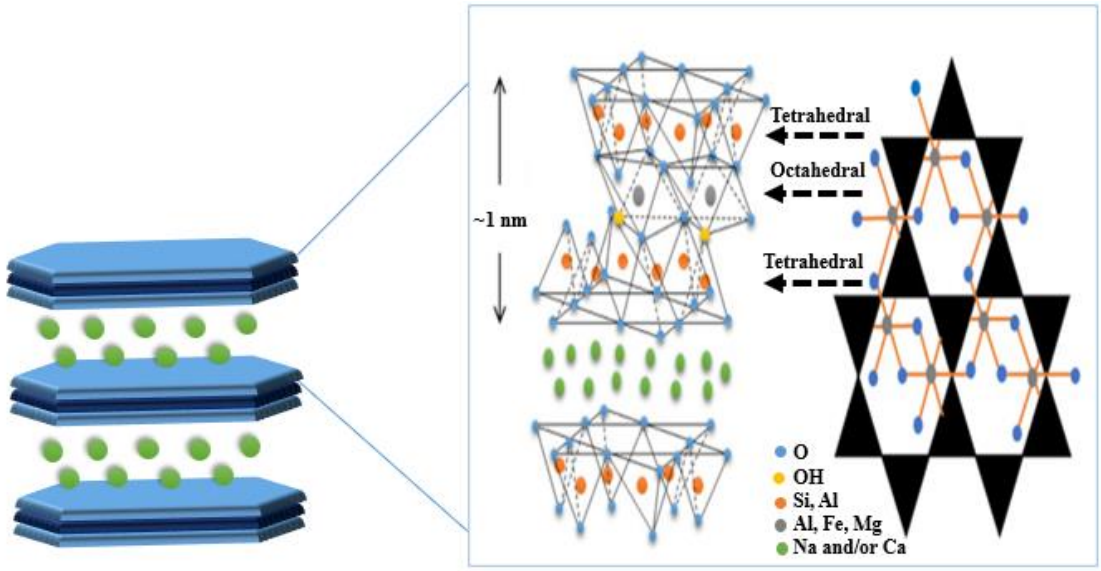

Figure 2.6. Schematic display of MMT and its layer structure (Zhou et al. 2019).

Similar to all clay minerals, MMT is cost-effective and biocompatible even at high concentrations with non-toxic degradation products. Given the remarkable physicochemical characteristics, such as particle size and shape, cation exchange capacity, specific surface area, charge density, MMT has aroused more and more interest in development of bioactive composite biomaterials. Montmorillonite is commonly used not only to improve the mechanical durability, swelling ability, film-forming capability, rheological features, and degradation behavior of the polymers but also to aid cellular adhesion, proliferation, and differentiation of different sorts of cells. Moreover, MMT is an effective natural hemostat that could be used to improve the hemostatic effectiveness of dressings due to the activation of the coagulation system through electronegativity. In addition, due to its acceptable biodegradability rate, MMT has been used as transport vehicles/carriers for the efficient delivery of therapeutic molecules (drugs and genes) (Mousa et al. 2018).

2.3.2.2. Organically Modified Montmorillonite (OMMT)

To enhance the functionality of clay compounds, cationic clay minerals can be modified through the interaction of clay with chemically active substances and polymers. To promote surface reactivity, clays can be chemically modified, which results in the fabrication of homoionic clays. In order to increase the hydrophobicity clays can be modified through interaction with organic substances that lead to the production of organoclays. Lastly, clay nanoparticles can be incorporated into a polymeric matrix to form clay-polymer composites with enhanced chemical and mechanical properties (Ghadiri et al. 2015).

Montmorillonite is one of the clay minerals that has a hydrophilic nature, which makes it incompatible with hydrophobic polymeric basis. Consequently, in order to increase the compatibility between hydrophobic polymer and clay minerals, clays ought to be treated with particular organic substances. As explained before, MMT layers possess an excessive negative charge and the charge equivalence is maintained by incorporation of exchangeable cations among the layers. Desorption and adsorption of cations in between clay layers require low energy, therefore they can be replaced effortlessly by organic cations to create organomodified-MMT (OMMT) (Yang et al. 2019). Hereby, a homogeneously mixed composite can be obtained with hydrophobic polymers, such as PLA.

One of the organic cations that are commonly employed for organoclay generation is a quaternary ammonium salt. The cationic section of quaternary ammonium salt replaces exchangeable cations between clay layers and widens the interlayer spacing with their long carbon chains. Trimethyl octadecyl ammonium bromide (TMOD) is one of the quaternary ammonium salts with a chain consisting of 18 carbons and can effectively widen the space between two galleries of the MMT. In addition, TMOD has an antibacterial effect on gram-negative and gram-positive bacteria (Sha et al. 2021; Sun et al. 2013). Therefore, in this study, TMOD was chosen as a representative quaternary ammonium salt to widen the basal spacing of MMT (Figure 2.7.), which leads to better compatibility of the clay compound and polymeric matrix in the composite structure with additional advantages, such as antibacterial properties.

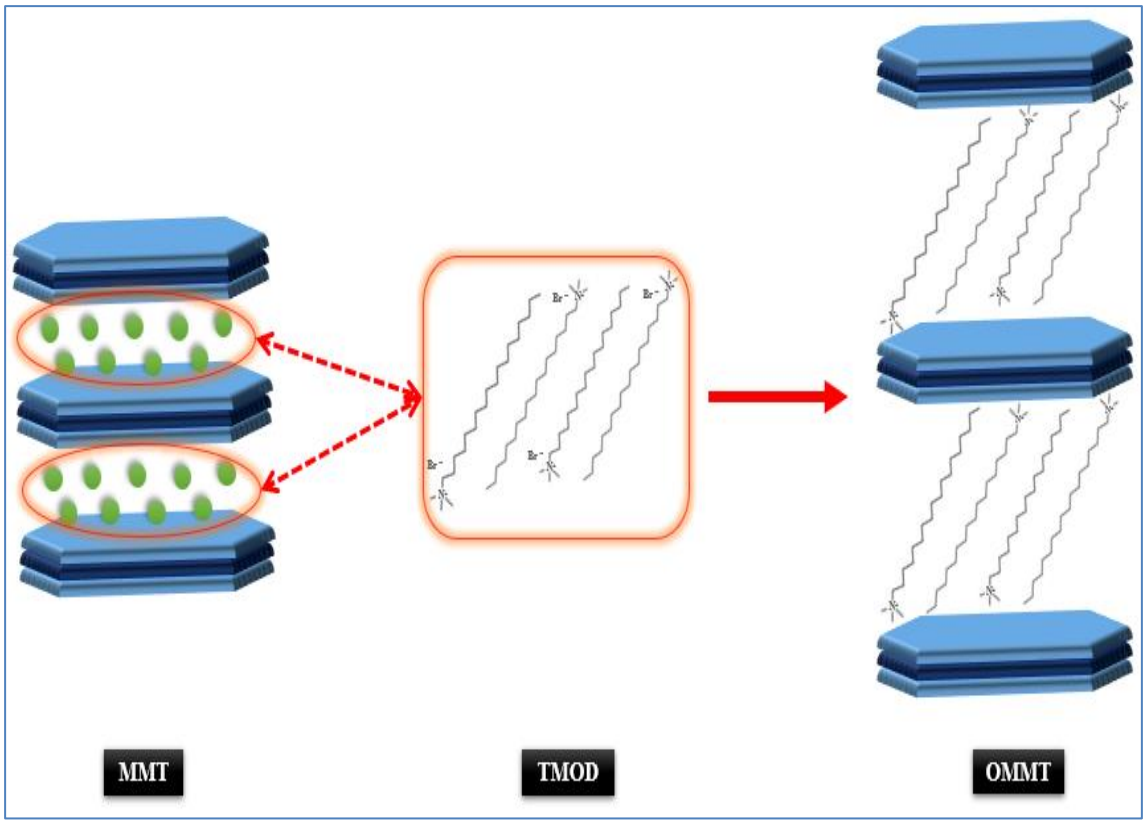

Figure 2.7. Schematic display of MMT, TMOD and OMMT structures.

2.3.3. Boron Compounds

Boron (B) is a semiconductive metalloid with the atomic number 5 and the symbol of B in the periodic table (Białek et al. 2019). Boron and its compounds are known to be advantageous for the metabolisms happening inside the body, fulfilling functions in steroid hormone metabolism, healthy maturation of bone tissue cells, keeping cell membrane intact, central nervous system functions, and alleviating arthritic symptoms, and are widely used in the development of tissue-engineered materials for bone tissue (Gültan et al. 2020; Gümüşderelioğlu et al. 2015; Tunçay et al. 2017), to enhance proliferation and differentiation of adipose mesenchymal stem cells (AdMSCs) (Akdere et al. 2019), periodontal ligament cells (PDL) (Arslan et al. 2018), and human bone marrow-derived stem cells (hBMSCs) (Bozoğlu et al.). A probable route for the favorable influence of B on health was suggested: It directly affects the synthesis of the ECM by activating elastase, trypsin-like enzymes, and collagenase.

The boric acid solution is applied as an antiseptic agent for disinfestation purposes in the wounded area. It was reported that the application of 3% boric acid solution promoted the healing of wounds with full thickness and tissue loss, reducing the healing time compared to intensive care. However, the utility of the solution is limited due to its probable toxicity, but the symptoms of acute or chronic toxicity are rare. The acceleration in the healing process is achieved by boosting the synthesis of proteoglycans, collagen, and proteins such as heat-shock proteins 70 (HSP 70) and tumor necrosis factor (TNF-α). TNF-α stimulates angiogenesis and fibroblast growth. Fibroblasts respond to TNF-α by producing several cytokines, which may have a favorable role in the wound healing process (Benderdour et al. 1998; Nzietchueng et al. 2002).

2.3.3.1. Boron Nitride (BN)

The powder form of boron nitride (BN) is called 'white graphite' due to the similarities between the crystal structure of graphite and BN. It displays a honeycomb structure with alternating B and nitrogen atoms that are connected with a strong σ bond established by sp^2 orbits of each B atom with the sp^2 orbit of neighboring N atoms. The layers of BN are connected through weak van der Waals forces, permitting the layers to move easily (Wang et al. 2017).

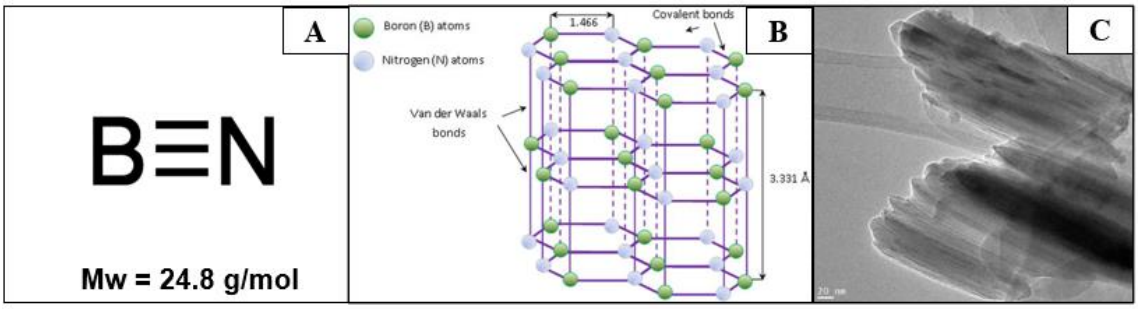

Figure 2.8. Boron nitride nanoparticles, A) Chemical properties, B) Honeycomb structure of BN sheets, C) TEM images of BN nanoparticles at 20nm magnification (Jedrzejczak-Silicka et al. 2020).

Hexagonal BN is a B source with low toxicity, high chemical and thermal stability, and mechanical strength with physicochemical properties similar to graphene and was used

in various studies as a drug carrier in tissue engineering (Figure 2.8). It is also reported that BN flakes have an antibacterial effect on gram-negative and gram-positive bacteria (Pandit et al. 2019). Furthermore, previous studies evaluating the consequence of BN in the wound healing process demonstrated that BN accelerated wound closure at low concentrations and increased angiogenic activity, cell proliferation, and migration of human dermal fibroblasts (HDF) cells while rescuing the cell from apoptosis (Şen et al. 2019; Tarhan et al. 2021).

2.3.3.2. Zinc Borate (ZB)

Zinc borate (ZB) is an inorganic compound with interesting properties such as cultivability with a wide variety of polymers, which makes zinc borate an interesting material for the fabrication of composites (Aysel et al. 2019). Moreover, ZB is non-toxic and recently has been used in developing biomaterials with enhanced mechanical properties and antibacterial effect. Also, due to the presence of the zinc element, ZB might be beneficial for several biological processes necessary for tissue regeneration (Jung et al. 2019).

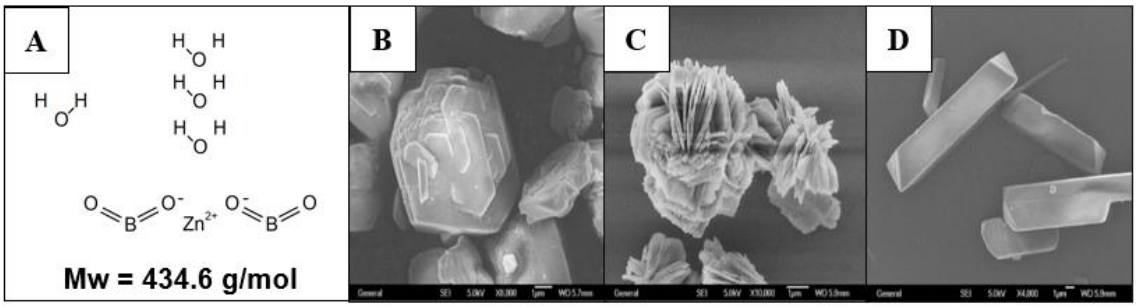

Figure 2.9. Zinc borate nanoparticles, A) Chemical structure of hexaboron dizinc undecaoxide, and SEM images of different zinc borates: B) $2ZnO{\cdot}3B_2O_3{\cdot}3.5H_2O$, C) $3ZnO{\cdot}3B_2O_3{\cdot}5H_2O$, and D) $2ZnO{\cdot}3B_2O_3{\cdot}7H_2O$ at 1 µm magnification (Cui et al. 2012).

Hexaboron dizinc undecaoxide ($2ZnO.3B_2O_3.3,5H_2O$) form of ZB is a white crystalline that is generated from zinc oxide and boric acid reaction under rough conditions (high temperature and concentration) (Aysel et al. 2019; Wang et al. 2012). Zinc borate can form various chemical structures due to the ability of B in coordinating with three (BO_3)

and four oxygen (BO_4) atoms. Each of chemical structures have unique shapes and chemical properties (Figure 2.9). Most natural borates contain water of crystallization in their structures. Skin tissue contains a comparatively high zinc content that is generally accumulated within the epidermis. The beneficial effect of zinc in the management of thermal and surgical wounds is vastly known. Zinc deficiency leads to roughened skin and impaired wound healing (Lin et al. 2017).

2.3.3.3. Phenylboronic acid (PBA)

In the chemical structure of phenylboronic acid (PBA), the B atom is bonded to the phenyl ring and two –OH groups in a trigonal configuration. Phenyl boronic acid can react with diols, such as glucose, to form a phenylboronic ester bond. Therefore, in several reports PBA have been utilized as an insulin and gene carrier (Shao et al. 2021; Shen et al. 2021).

Briefly, due to the empty orbital shell of B, PBA is a Lewis acid. In aqueous solutions, PBA pairs with an OH^- through Lewis acid-base reaction and forms a negatively charged boronate with a tetragonal configuration (Figure 2.10). At this state, PBA can bond with the diol groups of another compound. The stability of the newly formed complex depends on the negative charge of the PBA compound. The bond formed between PBA and the compound containing the diol group is reversible, which enables the composite to be sensitive to pH, sugar concentration, and H_2O_2 (Kim et al. 2017; Zeng et al. 2021).

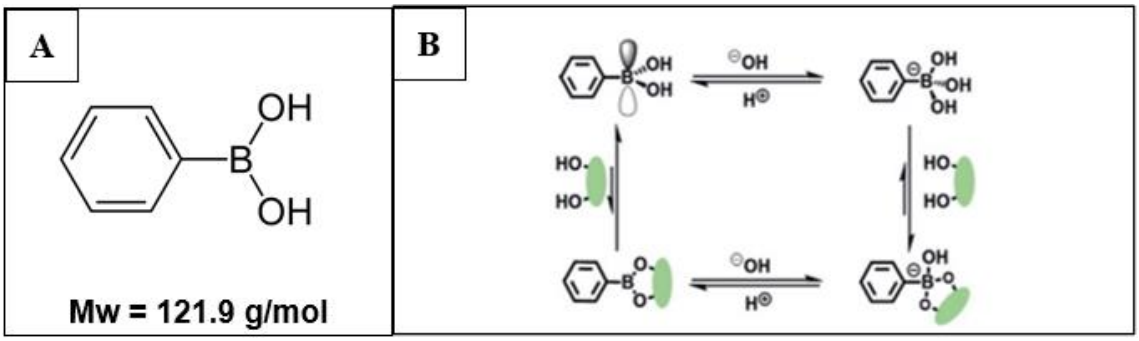

Figure 2.10. Phenylboronic acid nanoparticle, A) Chemical structure, B) The reaction of PBA with a compound containing cis-diol groups (Zeng et al. 2021).

Phenylboronic acid has attracted significant attention in designing smart drug delivery systems owing to its ability to form different chemical bonds (e.g., boric acid ester bond formation, weak intermolecular cross-linking, π–π interactions, and H-bonding) with functional groups of the drugs (Lu et al. 2019). Moreover, recent research has reported that the presence of PBA enhances the antibacterial effect, especially for wounds infected with gram-negative bacterium type. Moreover, PBA accelerates wound closure time and promotes collagen formation during wound-healing process (Wang et al. 2022).

2.4. Polymer-Nanoclay Interactions

To prepare a copolymer/clay macro or nanocomposite two routes can be followed: 1) Placing the polymer chains in-between clay layers, or 2) Polymerizing the desired monomers between layers. In case of the first approach, the interactions between polymers and clay minerals can be sorted into three types which depend on the degree of separation of the clay layers (Chen 2004) (Figure 2.11).

Conventional Composites: If the chains of the polymer are not able to penetrate in-between the galleries,

Intercalated Composites: If the polymeric chains enter the galleries but clay layers remain stacked,

Exfoliated Composites: If the clay layers are entirely separated to form an irregular arrangement.

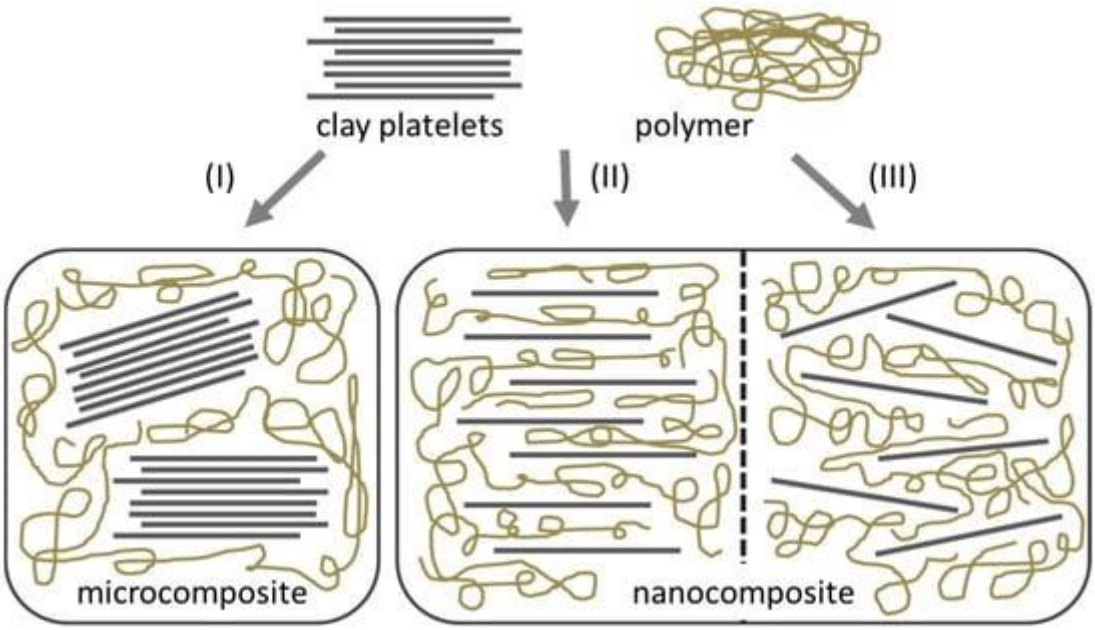

Figure 2.11. Various interactions of clays and polymer chains and the resulting composites. (I) Phase-separated microcomposite (conventional), (II) Intercalated nanocomposites, and (III) Exfoliated nanocomposites (Müller et al. 2017).

When the polymer chains do not enter between the silicate sheets, a phase-separated or conventional type of composite gets formed, which has the same properties as traditional microcomposites. However, without modification of clay compounds the interaction between polymer matrix and clay is limited to the conventional type. When polymeric chains enter between the layers of clay compound, an intercalated nanocomposite structure is formed with ordered crystallography, consisting of alternating polymeric chains and inorganic clay layers. Under typical conditions, only a few molecular chains of polymer can get intercalated between clay layers, not getting affected by the clay-polymer ratio. Upon exfoliation, complete or partial delamination of layers transpires as a consequence of a total diffusion of the polymer chains into the interlayer spacing of the clay compound. The degree of delamination depends on the amount of clay loaded in a polymer matrix, clay functionalities, and interfacial interaction between the polymer matrix and clay compound. It is worth mentioning that some of the studies suggested that exfoliated nanocomposites have more prevailing physicomechanical properties than intercalated nanocomposites (Müller et al. 2017; Murugesan and Scheibel 2020).

2.5. Composite Fabrication Method for Wound Dressing Applications

The high porosity for wound dressings is crucial as a dressing should secure respiration and enhance oxygen permeability (Adeli et al. 2019). Some of the most notable fabrication techniques which can fulfill mentioned criteria are solvent casting, electrospinning, electrospraying, and 3D printing (Figure 2.12). Two of these techniques, solvent-casting, and electrospinning, are explained in more detail.

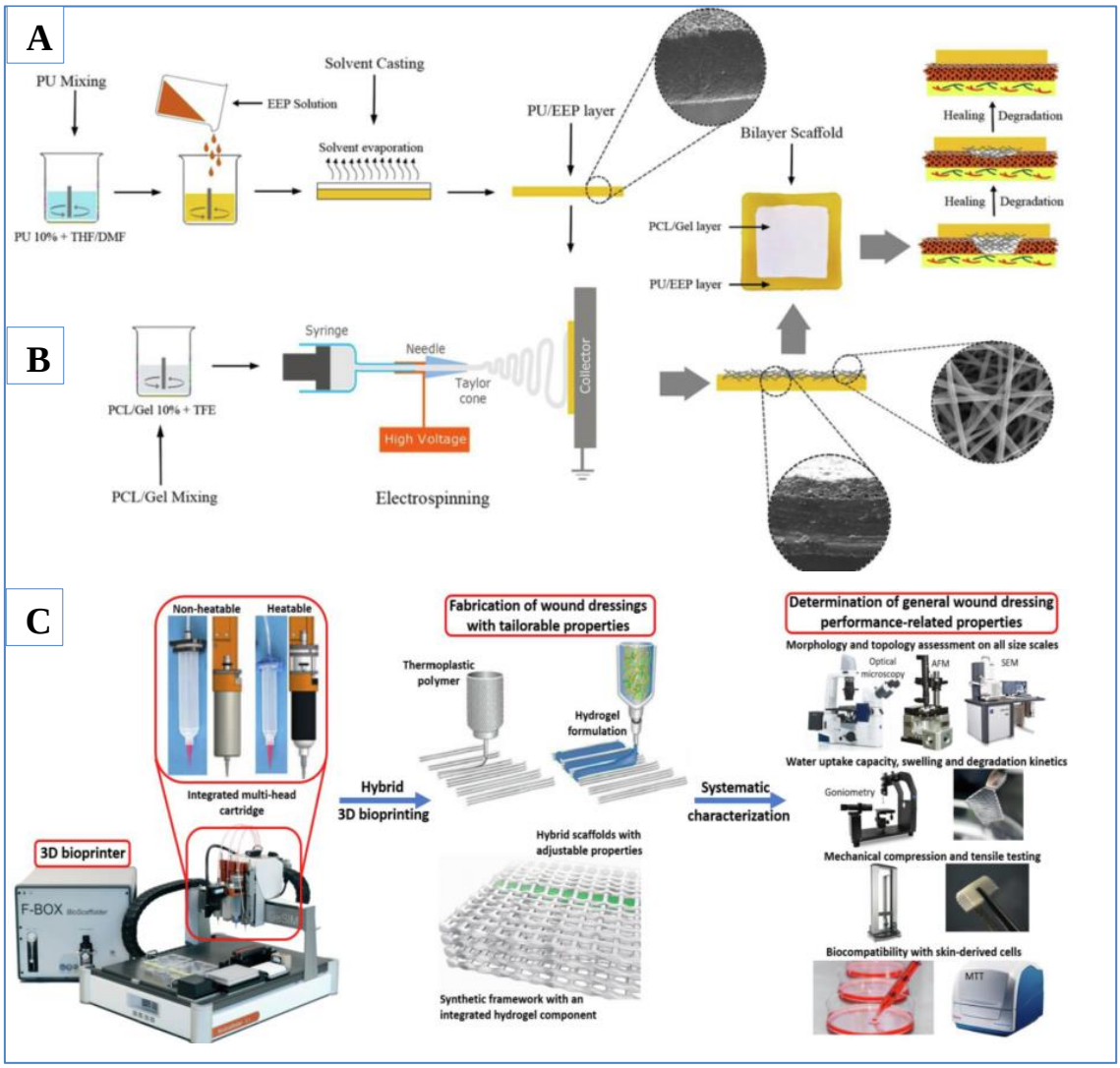

Figure 2.12. Various production methods for wound dressing applications. A) Solvent-casting B) Electrospinning, and C) 3D printing, using different polymers (Naseri and Ahmadi 2022).

2.5.1. Solvent-Casting

Solvent-casting is one of the conventional and most widely used techniques to produce film-form dressings for wound dressing application. These dressings are ready-to-use, flexible, and allow gas transmission and wound state monitoring while sufficiently sealing the site. In addition, the method and the process are not complicated and time-consuming as it does not require additional complex equipment. However, fabricating porous films is challenging as it demands salt or particulate leaching, which is not preferred as it removes incorporated bioactive agents, such as drugs. Moreover, the porosity and permeability of the wound dressing are not controllable in this technique (Naseri and Ahmadi 2022).

2.5.2. Electrospinning

Electrospinning is an effective way of fabricating non-woven ECM analogue fibrous scaffolds that consists of fibers in the diameter range of micro to nanoscale with a high surface-to-volume ratio and relatively controllable porosity. In addition, it is a simple, cost-effective, and sophisticated technique, which can be performed with synthetic or natural polymers (Arida et al. 2021). Furthermore, electrospinning can be used for drug encapsulation, as electrospun polymers have outstanding drug encapsulation capacity. In previous studies, electrospinning was performed to fabricate fibrous scaffolds for wound healing (Arida et al. 2021; Fang et al. 2019; Ji et al. 2006; Zhou et al. 2016). The application of nano scaled fibrous dressings in the initial phases of healing cascade and film dressings in the proliferation phase of the healing process is suggested (Naseri and Ahmadi 2022).

3. EXPERIMENTAL

This thesis focuses on the fabrication of the potential biomaterials to be used as skin tissue-engineered products to accelerate the wound healing process. For this proposes, hybrid biocomposites were fabricated utilizing poly(lactic acid) (PLA), montmorillonite (MMT), organomodified-montmorillonte (OMMT) and three different B compounds namely, boron nitride (BN), zinc borate (ZB), and phenylboronic acid (PBA). In order to fabricate the hybrid scaffolds, B compounds were adsorbed onto the OMMT and PLA based hybrid scaffolds were produced utilizing solvent-casting and electrospinning techniques. The effect of fabrication method on chemical and morphological structure, mechanical properties, biodegradability, and thermal properties were evaluated. In the second part of the present thesis, to examine the impact of organomodification of MMT on the fibrous scaffolds, B compounds were adsorbed on unmodified MMT and PLA-MMT/B hybrid composites were fabricated via electrospinning method. The antibacterial properties of fibrous scaffolds as well as their effect on normal human dermal fibroblasts (NHDF) cells were examined to reveal their potential as tissue-engineered products.

3.1. Materials

The materials used in the scope of thesis were summarized in Table 3.1.

Table 3.1. List of chemical and biological materials.

Material	**Company**	**Country**
1,1,1,3,3,3-Hexafluoro-2-propanol (HFIP)	Merck	Germany
3-(4,5-dimethylthiazol-2-yl)-2,5-diphenyltetrazolium bromide (MTT)	Sigma-Aldrich	Germany
Boron nitride	Boren	Turkey
Calcein AM	Thermo Fisher Scientific	USA
Calcium chloride	Merck	Germany

Chloroform	Merck	Germany
Dulbecco's Modified Eagle's Medium-Low Glucose (DMEM-LG)	Capricorn Scientific	Germany
Dulbecco's Modified Eagle's Medium-High Glucose (DMEM-HG)	Capricorn Scientific	Germany
Dulbecco's phosphate buffer solution	Lonza	Sweden
Ethyl alcohol	Teksoll	Turkey
Ethidium homodimer-1 (EthD-1)	Sigma-Aldrich	Germany
Fetal bovine serum (FBS)	Capricorn Scientific	Germany
Glutaraldehyde solution	Sigma-Aldrich	Germany
Isopropyl alcohol	Sigma-Aldrich	Germany
Lysozyme	Sigma-Aldrich	Germany
L-glutamine	Capricorn Scientific	Germany
Magnesium chloride	Merck	Germany
Montmorillonite (MMT K-10)	Sigma-Aldrich	Germany
Penicillin-streptomycin (P/S)	Capricorn Scientific	Germany
Phenylboronic acid	Sigma-Aldrich	Germany
Poly(L-lactic acid) (PLLA) (PURASORB PL 18)	Corbion	Netherlands
Sodium azide	Sigma-Aldrich	Germany
Sodium hydroxide	Merck	Germany
Sulfuric acid	Sigma-Aldrich	Germany
Trimethyl octadecyl ammonium bromide (TMOD)	Sigma-Aldrich	Germany

Trypsin/EDTA solution	Capricorn Scientific	Germany
Zinc Borate	Boren	Turkey

3.2. Preparation of Nanocomposites

For this work, six groups of scaffolds, which are neat ***PLA***, PLA doped with unmodified MMT ***(PLA-MMT)***, PLA doped with organomodified MMT (***PLA-OMMT***), PLA doped with BN adsorbed OMMT (***PLA-OMMT/BN***), PLA doped with ZB adsorbed OMMT (***PLA-OMMT/ZB***), PLA doped with PBA adsorbed OMMT (***PLA-OMMT/PBA***), were fabricated via solvent-casting and electrospinning methods. Thereafter, three groups of fibrous scaffolds were fabricated using unmodified MMT and B compounds which are PLA doped with BN adsorbed MMT ***(PLA-MMT/BN)***, PLA doped with ZB adsorbed MMT ***(PLA-MMT/ZB)***, and PLA doped with PBA adsorbed MMT ***(PLA-MMT/PBA)*** were fabricated via electrospinning method. The groups of scaffolds were summarized in Figure 3.1.

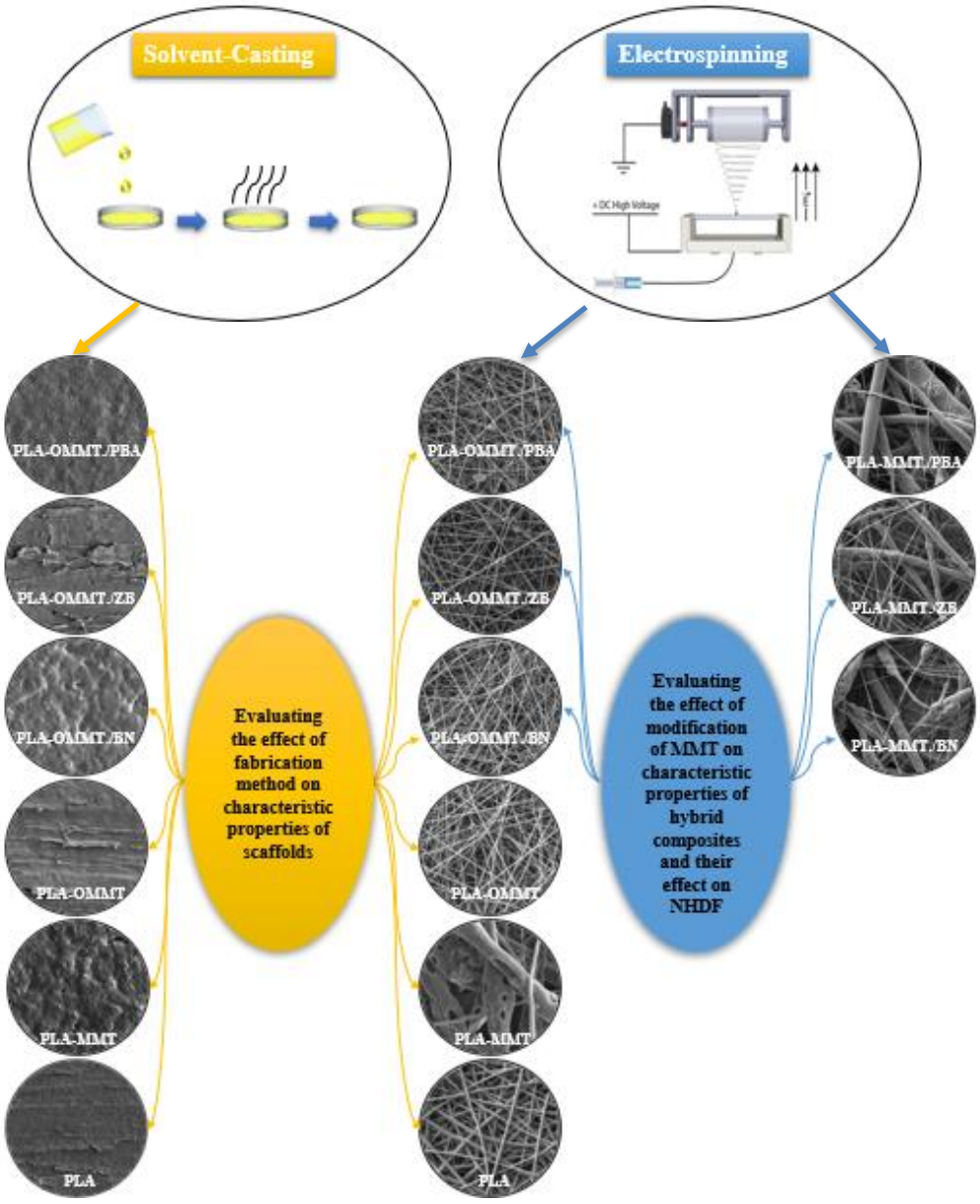

Figure 3.1. The summary of scaffolds fabricated via solvent-casting and electrospinning method.

3.2.1. Nanoclay Modification

For modification of the MMT to OMMT, firstly MMT was dried in an oven (Nüve, Turkey) at 150 ˚C for 18 h to remove residual moisture. Then, 5 g of dry MMT was weighed and suspended in 100 mL of distilled water for 2 h. Two-gram TMOD was added to the solution and magnetically stirred at 750 rpm for 5 h and the completion of the process was tested with $AgNO_3$. Organo-MMT was precipitated at the bottom of a plastic

bottle. Finally, OMMT particles were dried under a fume hood (Hedlab, Turkey) for 24 h (YALÇINKAYA et al. 2010).

3.2.2. Determination of Cation Exchange Capacities (CEC) of MMT and OMMT

After modification, cation exchange capacities (CEC) of MMT and OMMT were determined according to the method given in literature.(YALÇINKAYA et al. 2010). This method is based on the adsorption of methylene blue solution at a certain pH value and clay concentration. Briefly, a methylene blue solution with a concentration of 10 mg/mL was prepared. Two grams of MMT were dissolved in 300 mL of ultrapure water (UPW) and magnetically stirred until a homogeneous mixture was obtained. The pH of the mixture was adjusted with sulfuric acid to be in the range of 2.5-3.8. Then, 5 mL of methylene blue solution was added to the mixture and magnetically stirred for about 2 min. A drop from the mixture was dripped onto the filter paper with a glass baguette, and its color was observed. The process was repeated until the color stated in the standard was reached. At the beginning of the test, the droplets were blue and surrounded by a colorless water ring. As the progress continued, the color of the droplets gradually darkened as the amount of methylene blue absorbed by the clay increased. The experiment continued until a light blue ring was observed around the dark blue droplet. The same process was repeated for OMMT, and the results were compared.

3.2.3. Adsorption of B Compounds onto MMT and OMMT

For adsorption of BN, ZB, and PBA onto OMMT and MMT, each of the B compounds was weighed and added to ultrapure water and magnetically stirred for two days. After two days, the pH of the solutions was adjusted in the range of 9-9.5 with NaOH solution prepared in UPW. OMMT was added to the solution with the different clay:B ratios (1:1, 1:3, 1:5, 3:1, and 5:1 w/w), and the solutions were suspended for a day. The prepared solutions were centrifuged (Heraus, Germany) to separate the supernatant and the precipitated B loaded OMMTs (OMMT/B). The OMMT/B compounds were washed three times and kept at -20 ˚C for a day. Then, the samples were dried in a freeze dryer (Christ, Germany) for two days. The same procedure was repeated to adsorb B compounds onto MMT at the determined ratio (3:1 w/w).

3.2.4. Fabrication of Nanocomposites

The PLA-based micro/nanocomposites were produced by solvent-casting and electrospinning methods to compare the characteristic properties of emerging hybrid composites.

3.2.4.1. Solvent-casting

In order to fabricate membranes by solvent-casting method, the PLA was dissolved in chloroform: 1,1,1,3,3,3-hexafluoro-2-propanol (HFIP) (8:2 (v/v)) binary solvent system at a concentration of 10% (w/v). To prepare solutions of PLA-OMMT and PLA-OMMT/Bs, each of the OMMT and OMMT/B compounds was weighed and dissolved in the same binary solvent system with the concentration of 4% (w/v). Then, the solutions were sonicated for 1 h, and then pre-weighed PLA was added to the bottle at the same concentration (10% w/v) and the solutions were magnetically stirred for 24 h. The prepared solutions were poured into circular Teflon molds and dried under a fume hood overnight. The completely dried membranes were cut into the desired forms for each test. The thickness of the membranes was kept the same as the fibrous scaffolds fabricated by electrospinning method.

3.2.4.2. Electrospinning

To prepare solutions for electrospinning, the PLA was dissolved in a binary solvent system of chloroform:HFIP (8:2 (v/v)) to obtain a 10% (w/v) polymer concentration. The solution was magnetically stirred at room temperature for 24 h. For the preparation of PLA-MMT, PLA-OMMT, PLA-OMMT/BN, PLA-OMMT/ZB, PLA-OMMT/PBA, PLA-MMT/BN, PLA-MMT/ZB, and PLA-MMT/PBA solutions, each of MMT, OMMT, OMMT/Bs, and MMT/Bs was weighed and dissolved in the same binary solvent system with the concentration of 4% (w/v). The solutions were sonicated for 1 h, and then pre-weighed PLA was added to the bottle and the solution was magnetically stirred for 24 h.

The solution was prepared for electrospinning by being placed in a 5 mL plastic syringe. Then, the syringe and a vertically-positioned needle were connected through a polyethylene capillary tube (inner diameter 0.6 mm). With the aid of a pump system, the

solution was fed at a certain rate through the needle (Ne300, Inovenso, Turkey). A rectangular plate was used as a collector covered with aluminum foil and placed at a determined distance from the needle. The electric field needed for fiber generation was created using a high-voltage power supplier between the collector and needle. The electrospinning conditions were given in Table 3.2.

Table 3.2. Electrospinning parameters optimized for nanofibrous scaffolds.

Groups	Polymer (w/v (%))	MMT (w/v (%))	OMMT (w/v (%))	B (w/v (%))	Voltage (kV)	Distance (cm)	Flow rate (mL/h)
PLA	10	-	-	-	15.0	22.0	0.8
PLA-MMT	10	4	-	-	13.5	22.0	1.2
PLA-OMMT	10	-	4	-	13.5	22.0	1.2
PLA-OMMT/BN	10	-	3	1	20.0	15.0	0.8
PLA-OMMT/ZB	10	-	3	1	13.0	16.0	0.8
PLA-OMMT/PBA	10	-	3	1	11.0	18.0	0.5
PLA-MMT/BN	10	3	-	1	20.0	20.0	2.0
PLA-MMT/ZB	10	3	-	1	12.0	22.0	1.2
PLA-MMT/PBA	10	3	-	1	18.5	22.0	3.0

3.3. Characterization of Nanocomposites

In this part of the study, the physicochemical properties of solvent-cast membranes and electrospun scaffolds were determined.

3.3.1. Chemical Analysis

Attenuated Total Reflectance-Fourier Transform Infrared Spectroscopy (ATR-FTIR) analysis was used to examine the chemical structure of the composites and hybrid composites in the range of 400-4000 cm^{-1} wavelengths (Thermo Scientific Nicolet iS10, USA).

3.3.2. Energy dispersive X-ray (EDX)

To determine the incorporation of B compounds and clay nanoparticles into the polymeric scaffolds, energy dispersive X-ray (EDX) (FIB-SEM, Tescan, Czech Republic) analysis was performed.

3.3.3. Morphological Analysis

3.3.3.1. Scanning Electron Microscope (SEM)

Fibrous scaffolds and solvent-cast membranes were coated with a gold-palladium layer and were morphologically depicted by scanning electron microscopy (FIB-SEM, Tescan, Czech Republic). Fiber diameters were measured using SEM images through the Image J (NIH, USA) program.

3.3.3.2. Transmission Electron Microscope (TEM)

High contrast transmission electron microscopy (CTEM) (Tecnai G2 Spirit BioTwin CTEM, FEI, ABD) was performed to determine fiber diameters.

3.3.4. Thermal Analysis

Differential scanning calorimetry (DSC) and thermogravimetric analyses (TGA) were performed to define the thermal properties of fibrous scaffolds. To determine thermal mass loss with TGA (EXSTAR 6000, SII Nanotechnology Inc., Japan), samples heated in the range of 25 - 800 °C, and between room temperature to 400 °C with a heating rate of 5 °C/min DSC (Diamond DSC, PerkinElmer Inc., USA) was performed. The % crystallinity values of the all groups were calculated from the melting enthalpies in the DSC graph, according to Equation 3.1. In this equation, ΔH_m defines the melting enthalpy of the samples in the DSC graph, and ΔH_0 defines the melting enthalpy of the examining substrate in a 100% crystalline state. In the present case the melting enthalpy of PLA in 100% crystalline state is given as 93 J/g according to the relevant literature (Neto et al. 2012).

$$\text{Crystallinity (\%)} = (\Delta H_m/\Delta H_0) \times 100 \qquad \textbf{(Equation 3.1.)}$$

3.3.5. Biodegradability Test

İn-vitro biodegradability studies of membranes and fibrous scaffolds were performed in 10 mL of PBS (pH: 7.4) including 10 µg/mL lysozyme enzyme and 1 µg/mL sodium azide (Koç et al. 2021). When each determined period ended, scaffolds were removed and washed with ultrapure water twice before freezing at the temperature of -20°C. The scaffolds were dried in the freeze-dryer for a day. The weight of the dry scaffolds was measured and mass loss (%) was calculated by comparing the initial weight of the scaffolds with the weight of the dry samples obtained at the end of the experiment.

3.3.6. Water Contact Angle Measurements

The wettability of solvent-cast membranes was measured by sessile drop method at 25°C (Krüss DSA 100, Germany). To estimate the contact angle, the dimension of the membranes was adjusted for 1×1 cm^2, and then a droplet (5 µL) of distilled water was dropped.

3.3.7. Mechanical Test

The mechanical properties of solvent-cast membranes and fibrous scaffolds were determined by a tensile test (TA.XTplus Texture Analyzer, Stable Micro Systems, UK) to evaluate the reinforcing effect of the fillers in hybrid composites. The scaffolds with 3×5 cm^2 dimensions were immersed in PBS (pH: 7.4) at body temperature to mimic the natural environment of the body before the tensile tests. The elastic modulus was calculated from the stress-strain curves.

3.3.8. Water Uptake Capacity Test

Water uptake capacities of fibrous samples were examined gravimetrically in PBS (pH: 7.4) at body temperature on a dry weight basis (Yang et al. 2022). The dry scaffolds were weighed before being immersed in PBS. The wet scaffolds were taken from the PBS at particular time intervals and weighted after the extra PBS was removed by filter paper. The water uptake capacity was calculated using Equation 3.2. In this equation, W_d defines the weight of dry scaffold, and W_W defines the weight of wet scaffold.

$$\text{Water uptake ability (g/g)} = (W_W - W_d)/ W_d \quad \textbf{(Equation 3.2.)}$$

3.4. Antibacterial Study

The effects of various sterilization techniques such as autoclave, ethanol (Eth), ultra violet (UV), and Eth:UV combined method were investigated with SEM images and contamination test. For **autoclave**, the scaffolds were kept at 121 °C for 30 min. Ultra violet radiation operated on each side of the scaffolds during different time intervals (1/1 and 2/2, indicating 1 and 2 h of UV application per side, respectively) for **UV** sterilization. In **Eth** and **Eth:UV** combined methods, firstly the fibrous samples were kept in %70 (v/v) ethanol solution, and then UV was applied on each side of the scaffolds same as explained in UV sterilization. Based on the results, a combined method of Eth:UV was preferred to sterilize the fibrous scaffolds, where they were immersed in 70% ethanol for 30 min, then UV was applied to each side of the scaffolds for an hour. The scaffolds were washed using PBS before UV application to remove any residue of the ethanol.

The antibacterial activities were examined with agar disk diffusion and the optical density (OD) methods using model microbial species, namely *Escherichia coli* (*E. coli*) ATCC 25922 representing gram-negative bacteria, and *Staphylococcus aureus* (*S. aureus*) ATCC 25923 representing gram-positive bacteria with a bacterial concentration identical to 0.5 McFarland turbidity standards.(Haider et al. 2015; Ul-Islam et al. 2013). In the case of the agar disc diffusion method, the antibacterial properties of fibrous samples were displayed as halo zones formed around the scaffolds. The diameter of the clear zones of inhibition was measured and reported. For the OD method, the concentration of scaffold to media was adjusted for ~0.01 g scaffold/mL, and sterile scaffolds were put in 2 mL of Mueller Hinton Broth media. Then, 100 μL of bacterial strains were added to each tube and were inoculated in a shaking incubator at body temperature for a day. At various time intervals of 0, 3, 6, 9, 12, 16, 20, and 24 h, 200 μL of each test group was diluted with 800 μL sterile PBS and the turbidity of the resultant solution was read with Nanodrop 2000 (Thermo Fisher Scientific, USA) at 610 nm to define the bacterial proliferation. Cultures without any scaffold served as control groups.

3.5. Cytotoxicity Test

The cytotoxicities of the materials were tested with normal human dermal fibroblasts ((NHDF-Ad CC-2511)) in a laminar flow cabinet (Bioair, Italy). The cells were sub-cultured in flasks with DMEM-LG containing 10 % (v/v) FBS, 1 % (v/v) P/S, and 2 % (v/v) L-glutamine. The cells were detached from the flask surface by trypsin (0.01 %)/EDTA (10 mM) and seeded into 48-well tissue culture polystyrene (TCPS) plates with 1×10^4 cells/well. The fibroblasts were incubated for almost 4 days until to reach the confluency. The sterile fibrous samples were incubated in a culture medium at 37 °C for 1, 2 and 3 days. At the end of each determined day, the medium in the tubes was withdrawn and added to NDHF cells at 100%, 50%, and 25% dilutions obtained with cell culture medium. The cells that were seeded in TCPS with a fresh culture medium were served as the control. After culturing the cells for 1, 2, and 3 days with these extraction media, cell viability was determined by a 3-(4,5-dimethylthiazol-2-yl)-2,5-diphenyltetrazolium bromide (MTT) assay. The medium on cells was removed, and 300 µL of DMEM-LG solution containing 30 µL of MTT solution was added to each well. After a 3 h incubation period, the medium on the cells was removed and isopropyl alcohol was added to dissolve the formed formazan crystals. The optical density of the solution was measured with a microplate reader (Asys UVM 340, Austria) at 570 nm with 650 nm as a reference.

3.6. *In-vitro* Cell Culture Studies

3.6.1. Cell Viability Test

In the cell culture study of samples, each fibrous scaffold was cut into 1×1 cm^2 dimensions and sterilized. Sterile scaffolds were put in 24-well nontreated-tissue culture polystyrene (TCPS) plates. Then, 20 µL cell suspension including 5.5×10^5 cells in DMEM-LG medium were seeded on each scaffold. After 45 min, 20 µL of DMEM-LG was added to the wells and this process was repeated twice. Lastly, after 2 h, 940 µL of DMEM was added to each well, and cells were incubated in 5% CO_2 at 37 °C. The culture was conducted for 14 days, and the medium was refreshed every 3 days. Cell viability and proliferation were investigated by MTT assay at determined time intervals up to 14 days following the same steps which were explained in the cytotoxicity test.

3.6.2. SEM Analysis

The attachment behavior and morphological properties of the proliferated NHDFs on scaffold surfaces were observed on the determined days of culture by SEM (FIB-SEM, Tescan, Czech Republic) analysis. The culture media were removed from wells and fibrous samples were washed using sterile PBS for three times. The cells were fixed using glutaraldehyde solution at the concentration of 2.5% (v/v) and washed with PBS after 30 min. Later, scaffolds were washed using ethanol solutions with different concentrations (30, 50, 70, 90, and 100% (v/v)) for 2 min in each solution to prepare for SEM analysis.

3.6.3. Live/Dead Staining

The live/dead ratio of the cells were visualized by live/dead staining method with calcein AM for labeling live cells and ethidium homodimer-1 (EthD-1) for labeling dead cells on the 5^{th} and 14^{th} day of culture. Calcein AM, which naturally does not have fluorescent properties, passes through the living cell membrane, undergoing enzymatic hydrolysis with esterase activity in the cell cytoplasm, becomes fluorescent and viable cells appear green when viewed under a fluorescence microscope. Ethidium homodimer-1 which cannot pass through the membrane of a living cell can bind to nucleic acids when the membrane integrity is disrupted after cell death. When dead cells get stained with EthD-1, they appear red under a fluorescence microscope.

Samples were washed with PBS+ (PBS containing Ca^{2+} and Mg^{2+}), and then all samples were stained with 300 µL of PBS+ that contained 0.3 µL of each dye. After 30 min of incubation in the dark, cell viability was observed with a fluorescent microscope on the samples washed twice with PBS+ solution.

3.7. Statistical analysis

All experimental results were stated as ± standard deviation as a representation of three similar tests in triplicate. The results were statistically evaluated using Graph-Pad Prism 6 (GraphPad Software Inc., San Diego, CA). Statistical analysis was performed using a one-way test, where the *p*-value is less than 0.05, which was accepted as significant.

4. RESULTS AND DISCUSSION

This research mainly focusses on fabrication of novel dressings which are superior to conventional dressings, utilizing simple and cost-effective methods of fabrication, such as solvent-casting and electrospinning. For this purpose, available B compounds and clay nanoparticles were chosen to fabricate hybrid composites. Prior to the fabrication of composites, MMT mineral was modified with TMOD salt to improve the interaction of hydrophobic PLA and hydrophilic MMT to form intercalated composites. Then, to prevent possible toxic effect of selected B compounds, each of BN, ZB and PBA were adsorbed onto OMMT before incorporating into the polymeric matrix. The scaffolds were fabricated via solvent-casting and electrospinning methods. The physicochemical characterization studies were conducted to reveal the effect of fabrication method on both groups of samples and results were given in this section. Later, new groups of fibrous scaffolds were fabricated to reveal the commanding effect of MMT modification on overall physicochemical properties of hybrid scaffolds, as well as their antibacterial effect against model microbial species. The same procedure of adsorption was carried out to adsorb B compounds onto unmodified MMT. The cytotoxicity of the modified clay nanoparticle and chosen B compounds were determined using extracts of hybrid scaffolds. Lastly, viability, adhesion, and morphology of NHDF cells were evaluated during the *in-vitro* cell culture study.

4.1. Characterization of OMMT Nanoparticles

4.1.1. Attenuated Total Reflectance-Fourier Transform Infrared Spectroscopy (ATR-FTIR) Analysis

In this context, we hypothesized that the B compounds and nanoclay employed in the 3D fibrous system could be promising for the adequate treatment of ulcers by enhanced physicochemical/mechanical properties and antibacterial activities. Therefore, we aimed to produce wound dressings that can i) have an antibacterial effect so that bacteria would not be able to adhere and proliferate on their surface which decreases the possibility of wound infection, ii) would cover the wound lesion and prevent pathogens from entering the body, iii) support various stages of wound healing process morphologically,

chemically, and mechanically by adding B compounds. As a distinctive feature, MMT which was chosen as a clay nanoparticle in this study was used not only as a reinforcing agent but also as a carrier for various B compounds in the structure of hybrid composites. The B compounds that were chosen due to their beneficial effect in various stages of the wound healing process were adsorbed on MMT nanoparticles before being introduced to the polymeric matrix. Owing to the highly hydrophilic nature of the MMT nanoparticle, it needs to be modified before being introduced to the hydrophobic polymer matrix. To increase the compatibility of MMT and PLA which was the chosen polymer in the scope of the thesis, the MMT nanoparticles were modified with TMOD salt as one of the quaternary ammonium salts through ion-exchange reaction and the chemical structure of the unmodified and modified MMT nanoparticles was analyzed with ATR-FTIR and the spectra of each particle were given in Figure 4.1.

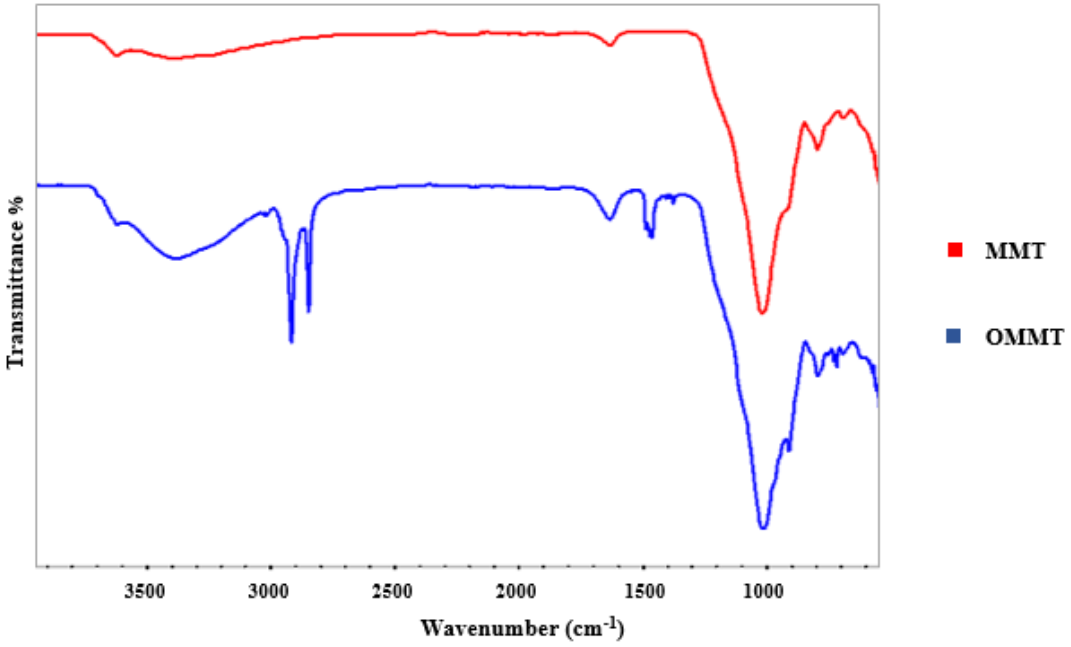

Figure 4.1. ATR-FTIR spectra of MMT and OMMT.

The peak around 3620 cm^{-1} corresponds to stretching vibration of –OH in Al-OH of MMT (Yang et al. 2022); the peaks around 3380 cm^{-1} and 1630 cm^{-1} correspond to stretching vibration and bending vibration of H–O–H; the peak around 1030 cm^{-1} corresponds to stretching vibration of Si–O. OMMT has also different absorption peaks while

maintaining the characteristic peaks of MMT in contrast to the FTIR spectrum of MMT. The peaks near 2849 cm^{-1} and 2920 cm^{-1} correspond to the symmetric and asymmetric stretching vibrations of CH_2 (Yang et al. 2019); peaks appearing near 1460 cm^{-1} and 1370 cm^{-1} correspond to the asymmetric stretching vibration of C–H bending of both CH_3 and CH_2 groups in the long carbon chain of TMOD salt (Kozak and Domka 2004). Results showed that MMT particles were successfully modified with TMOD.

4.1.2. CEC Experiments

The CEC values demonstrate the number of cations that a clay compound is capable to hold at a certain pH value and it is expressed as centimol per kg (cmol/kg) or milliequivalent of hydrogen per 100g (meq/100g) (Murugesan and Scheibel 2020). The change in CEC values was given in Figure 4.2.

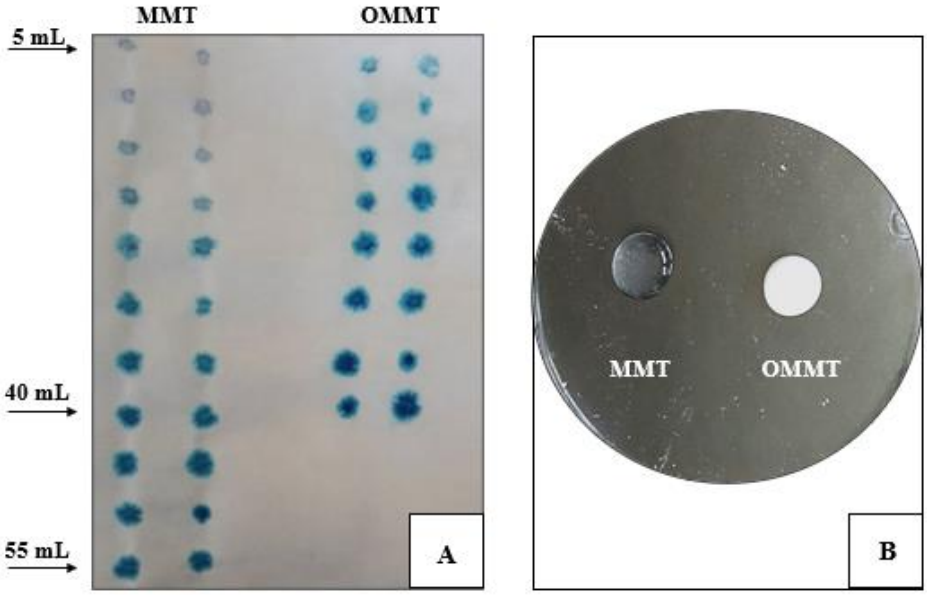

Figure 4.2. Organomodification of MMT through ion exchange reaction A) Cation exchange capacity experiments with methylene blue staining. B) $AgNO_3$ test to check the completion of modification reaction of MMT.

The value of CEC decreased after the modification of MMT (86.08 meq/100g) to OMMT (62.6 meq/100g) since $(CH_3)_3(CH_2)_{17}N^+$ replaces some of the Ca^{2+} and Na^+ cations in MTT. Due to this effect, the capacity to absorb the methylene blue decreased as well. It was also observed in previous studies that when MMT was modified, the value of CEC decreased (Lee et al. 2006). During the reaction, as $(CH_3)_3(CH_2)_{17}N^+$ cations enter the structure of MMT, the amount of Br^- ions increases in the supernatant, so the completion of the reaction can be tested by using an $AgNO_3$ solution. After adding $AgNO_3$ to the solution obtained from the reaction, the change of color from transparent to white due to the formation of AgBr, confirms the completion of the exchange reaction (Figure 4.2.)

4.2. Characterization of OMMT/B Compounds

4.2.1. ATR-FTIR Analysis

The ATR-FTIR spectra of OMMT, BN, and OMMT/BN compounds after adsorption was given in Figure 4.3.

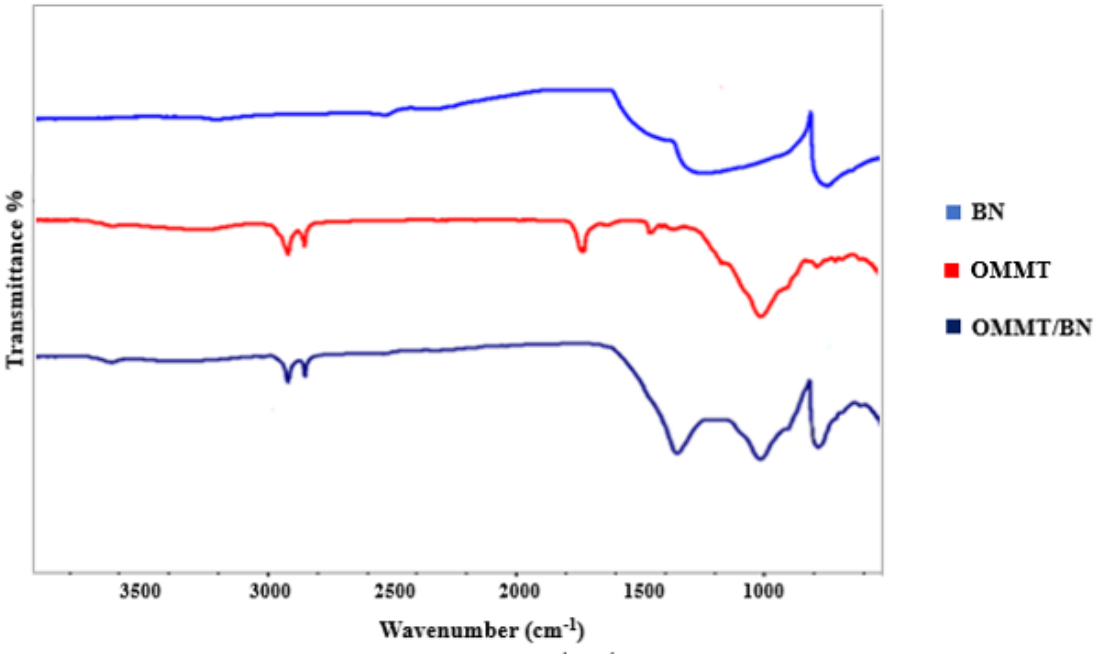

Figure 4.3. ATR-FTIR spectra of OMMT, BN and OMMT/BN nanoparticles.

The FTIR spectrum of BN indicates two characteristic peaks near 760 and 1330 cm^{-1} that corresponds to the stretching vibration of B–N and the bending vibration of B–N–B,

respectively (Budak 2018). Boron nitride was adsorbed into OMMT at 1:1, 1:3, 1:5, 3:1, and 5:1 (w/w) ratios, and FTIR spectra of the OMMT/BN were evaluated (data not shown). All of the characteristic peaks of OMMT and BN were observed in three ratios (1:1, 3:1, and 5:1 w/w) of OMMT/BN nanoparticles. The electrospinning solutions of mentioned ratios of OMMT/BN were prepared and the electrospinning process was carried out. Two ratios of 1:1 and 5:1 failed to produce continuous fibers during the electrospinning process due to the constant formation of droplets and unstable jets. This procedure was repeated for OMMT/ZB nanoparticles as well and similar results were observed and the optimum ratio for adsorption was determined as 3:1 (w/w) for OMMT/Bs. As there were no new adsorption peaks or any changes in characteristic peaks of OMMT and BN in the FTIR spectrum of the 3:1 (w/w) OMMT/BN, it was inferred that BN was physically adsorbed on OMMT. The BN is chemically inert and its interaction with the MMT is limited to weak Van der Waals forces and possibly the formation of hydrogen bonds between the nitrogen of the BN and hydroxyl groups of MMT.

The FTIR spectra of ZB, OMMT, and OMMT/ZB was presented in Figure 4.4.

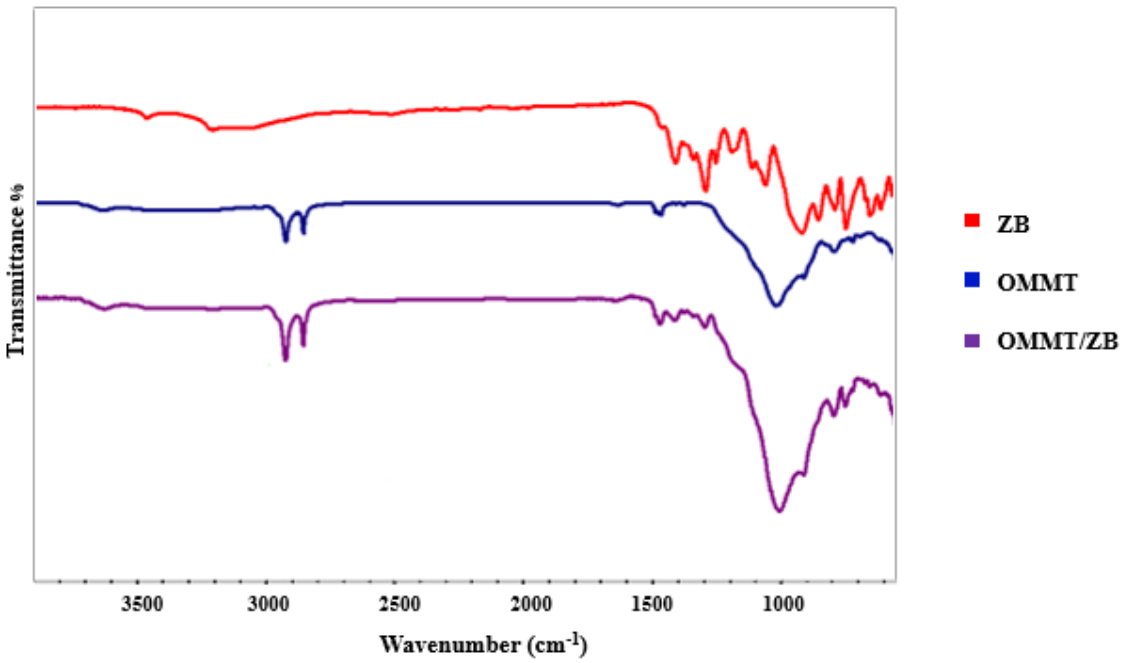

Figure 4.4. ATR-FTIR spectra of OMMT, ZB and OMMT/ZB nanoparticles.

The peaks in the range of 1406 cm^{-1} and 1251 cm^{-1} correspond to asymmetric vibration of the three-coordinate $B_{(3)}$-O; the peaks between 1189 cm^{-1} and 1110 cm^{-1} correspond to the bending vibration of the B-O-H; the peak at 1060 cm^{-1} is due to the asymmetric vibration of the $B_{(4)}$-O band; the peak at 919 cm^{-1} is related to the symmetric vibration of the $B_{(3)}$-O band; the peaks between 854 cm^{-1} and 790 cm^{-1} correspond to the symmetric vibration of $B_{(4)}$-O band; the peak at 748 cm^{-1} corresponds to rocking vibrations that belong to $B(OH)_4)^-$; the out of plane bending of $B_{(3)}$-O is observed at approximately 653 cm^{-1} (Ersan et al. 2016). Similar to the results of the OMMT/BN, OMMT/ZB was physically adsorbed on OMMT. The only noteworthy difference between OMMT/BN and OMMT/ZB was the presence of the peaks which belonged to symmetric and asymmetric vibration of water that was observed in OMMT/ZB due to the presence of H_2O molecules in ZB structure and weakly adsorbed water on OMMT/ZB compound. Because of the organomodification of MMT and the hydrophobicity of the BN compound, the peaks that belonged to H_2O were eliminated in the FTIR spectrum of OMMT/BN.

The characteristic FTIR spectrum of PBA is described in Figure 4.5. indicated a peak at 1432 cm^{-1} that corresponds to the B–O–C; the peak that appears near 3200 cm^{-1} corresponds to symmetric and asymmetric C–H stretching in the benzene ring; the peaks at 1603 and 1498 cm^{-1} corresponds to the stretching vibration of the C–C aromatic group; the peak at 1344 cm^{-1} corresponds to vibrations of the phenyl group; the peaks between 1023 and 1089 cm^{-1} correspond to the stretching vibrations of B–O–H and C–B bands; lastly, the peak at 580 cm^{-1} corresponds to the bending vibration C–B band (Abniki et al. 2022). After the adsorption process of PBA to the MMT, noteworthy changes were marked in the FTIR spectrum of OMMT/PBA and as expected, PBA was chemically bonded to diol groups present at OMMT layers.

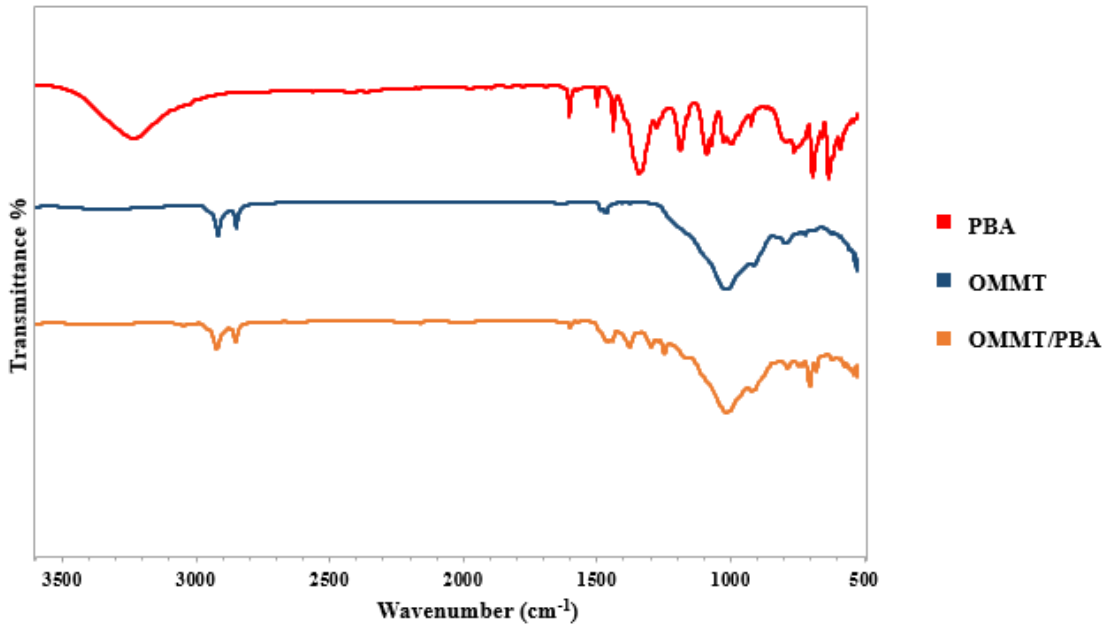

Figure 4.5. ATR-FTIR spectra of OMMT, PBA and OMMT/PBA nanoparticles.

As the adsorption reaction was realized at high pH values, the PBA and OMMT formed a stable complex. The elimination of the B-O-H adsorption peaks and the shifting in adsorption peaks of B-phenyl groups at the FTIR spectrum of OMMT/PBA proves the formation of the complex.

4.2.2. TGA

The TGA of each B compound before and after adsorption to OMMT was tested and the results of BN, OMMT and OMMT/BN were given in Figure 4.6.

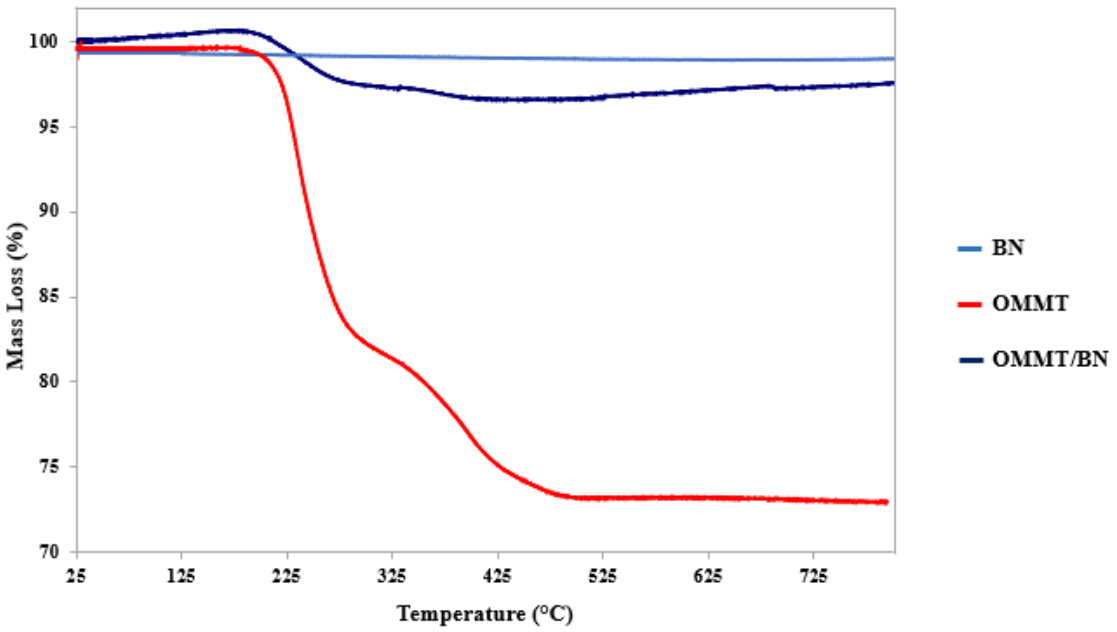

Figure 4.6. Thermogravimetric analyses curves of OMMT, BN and OMMT/BN nanoparticles.

According to the TGA results, BN has high thermal stability and the mass remains roughly constant up to around 800˚C under the N_2 atmosphere (Yu et al. 2016). However, OMMT nanoparticles exhibit different behavior. The major mass losses of OMMT happen in two steps at different temperature regions. In the first step, OMMT lost approximately 17% of its initial weight due to the loss of adsorbed water at 217˚C. The decomposition of incorporated aliphatic carbon chains of OMMT happened in the second step and OMMT lost about 7% of its initial weight at 351˚C.(Ganguly et al. 2010). A similar trend was observed in OMMT/BN with a modest decrease in the onset degradation temperature of the first and second steps. On the other hand, OMMT/BN lost only 5% of its initial weight during the process. The excess residual weight indicates that during the thermal degradation, the layers of the BN act as barriers on the surface and limit the transport of heat which delays the thermal degradation of the compound (Ayoob et al. 2018).

The TGA results of ZB that were illustrated in Figure 4.7. showed two steps of weight loss.

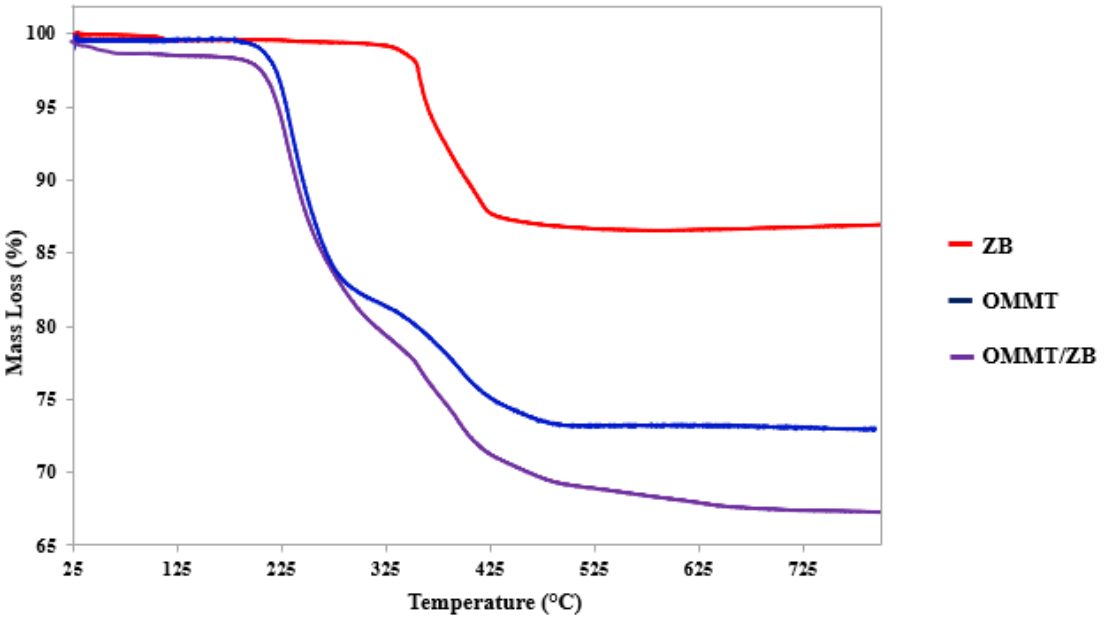

Figure 4.7. Thermogravimetric analyses curves of OMMT, ZB and OMMT/ZB nanoparticles.

The first step was due to dehydration of ZB that starts upon heating above 113°C. This value was lower than the ones that were reported for $2ZnO.3B_2O_3.3,5H_2O$ (~290°C) in previous studies (Ersan et al. 2016). The reason might be the poor crystallinity of the ZB. The major mass loss happens at temperatures of 357°C when zinc oxide and boric acid are formed and ZB losses approximately 12.7% of its initial weight (Younis 2022). The thermal degradation trend of OMMT/ZB consisted of three steps. The OMMT/ZB lost `about 1% of its initial weight at low temperatures which is due to the evaporation of weakly bonded water molecules. In the second step, dehydration of OMMT happened with no significant change in onset degradation temperature of OMMT and the compound loses approximately 19% of its initial weight. The final step took place at 340˚C, attributable to the decomposition of incorporated aliphatic carbon chains of OMMT and decomposition of hydrated ZB, the compound simultaneously lost 10% of its initial weight.

The TGA results of PBA presented in Figure 4.8. showed two steps of weight loss.

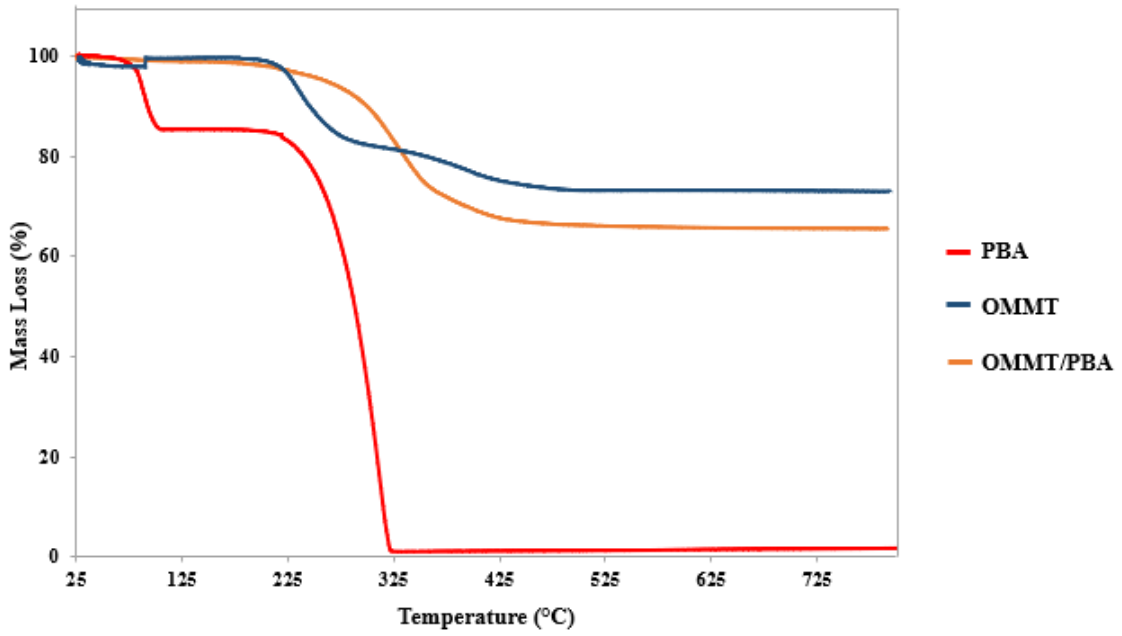

Figure 4.8. Thermogravimetric analyses curves of OMMT, PBA and OMMT/PBA nanoparticle.

The first step was due to the elimination of water that occurs at 90°C and PBA losses approximately 15% of its initial weight. At temperatures of 313°C decompositions of PBA took place and the compound degraded completely as well-known (Adamczyk-Woźniak et al. 2018). The thermal degradation of OMMT/PBA consisted of two steps. After the formation of the phenylboronic ester-OMMT bond, water molecules were generated, and the first step of weight loss was due to the elimination of water molecules that happened at low temperatures (~56˚C). The second step took place at 275˚C which was attributed to the decomposition of PBA and the compound lost about 34% of its initial weight. The formation of a highly stable coal layer during the thermal degradation by PBA prevented further degradation of OMMT (Abniki et al. 2022).

4.3. Fabrication and Characterization of PLA-OMMT/B Composites

4.3.1. ATR-FTIR Analysis

To investigate the interaction between PLA matrix and OMMT and OMMT/B compounds, nanofibers were analyzed through ATR-FTIR, and the spectra of all groups were given in Figure 4.9. The spectrum of PLA obtained from both solvent-casting and electrospinning showed adsorption peaks at 2995 and 2947 cm^{-1} that corresponds to

asymmetric and symmetric vibrations of the $–CH_3$; the sharp peak at 1750 cm^{-1} corresponds to the stretching vibration of the C=O; The bands between 1180 - 1043 cm^{-1} were related to the C–O group; the peaks at 1455 and 1361 cm^{-1} corresponds to asymmetric and symmetric bending vibrations of $–CH_3$; The band regarding C-H bending vibration was located at 1382 $cm^{-1}$and finally, a band at 868 cm^{-1} is assigned to the stretching vibration of the C-C single bond (Mushtaq et al. 2020; Nim et al. 2018).

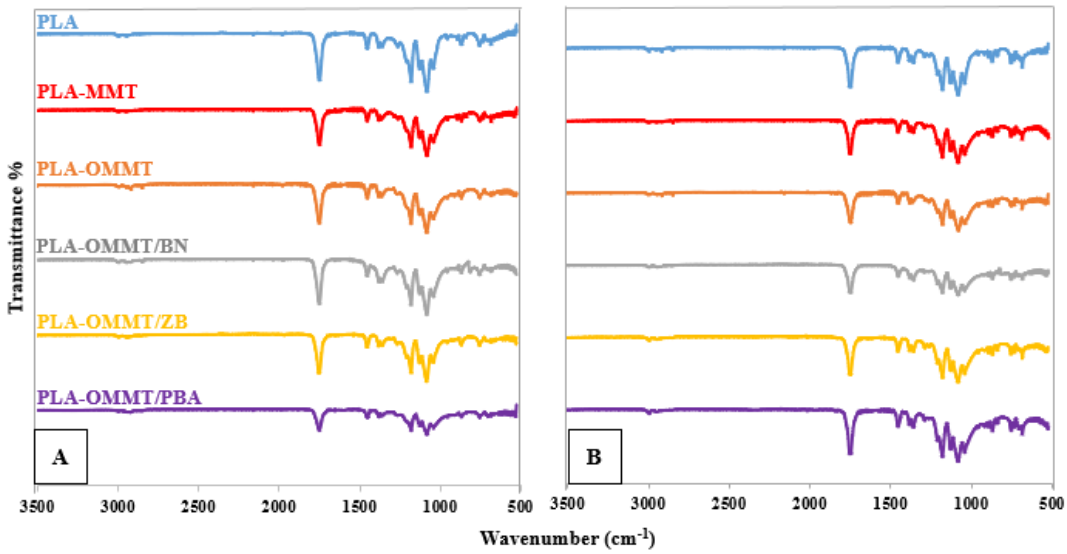

Figure 4.9. ATR-FTIR spectra of PLA, PLA-MMT and PLA-OMMT composites, and PLA-OMMT/B hybrid composites. A) Scaffolds obtained from electrospinning, B) Membranes obtained from solvent-casting

At the ATR-FTIR spectra of PLA-OMMT and PLA-OMMT/B nanofibers, new peaks at 2950 and 2920 cm^{-1} were observed due to the symmetric and asymmetric stretching vibrations of CH_2 which was one of the characteristic peaks of OMMT and proved the presence of this compound in the structure. In addition, the peak around 3620 cm^{-1} which belongs to the stretching vibration of –OH of OMMT was restrained in PLA-OMMT and PLA-OMMT/B composites, demonstrating the formation of hydrogen bonds via the hydroxyl groups of OMMT and PLA (Yang et al. 2022). In contrast, characteristic peaks of PLA remained unchanged and the ATR-FTIR spectrum of PLA-MMT was almost identical with neat PLA and it was difficult to make a certain judgment about the presence of the B compounds in the structure of hybrid composites. It may be due to the low amount of B compounds in the structure and the overlapping effect of characteristic peaks

of B compounds and PLA. In order to further investigation and to affirm the presence of the B compounds in nanofibers, EDX analysis was conducted.

4.3.2. EDX Analysis

The summary of EDX spectra for PLA, PLA-MMT, PLA-OMMT, PLA-OMMT/BN, PLA-OMMT/ZB, and PLA-OMMT/PBA were summarized in Table 4.1.

Table 4.1. Summary of weigh percentages of each element in the structure of PLA, PLA-MMT, PLA-OMMT and PLA-OMMT/B hybrid composites acquired from EDX spectra.

Groups	C (%)	O (%)	Si (%)	Al (%)	B (%)	N (%)	Zn (%)
PLA	57.1	16.2	-	-	-	-	-
PLA-MMT	67.2	27.0	4.5	0.8	-	-	-
PLA-OMMT	65.7	28.0	4.4	1.6	-	-	-
PLA-OMMT/BN	66.2	15.7	1.9	0.5	13.8	1.8	-
PLA-OMMT/ZB	67.2	14.4	2.5	0.8	14.4	-	0.5
PLA-OMMT/PBA	74.7	9.3	1.9	0.8	13.1	-	-

When PLA fibrous matrix was doped with MMT and OMMT, the weight amount (%) of aluminum and silicon was the evidence of the presence of nanoclay particle in the structure of the nanofibers. All PLA-OMMT/B groups have B in their structure (~14%). Whereas, in PLA-OMMT/BN, nitrogen, and in PLA-OMMT/ZB, zinc was present as well. In PLA-OMMT/PBA, the amount of carbon increased further as there were carbon atoms in the PBA structure.

4.3.3. Morphological Properties

The morphological properties of tissue-engineered products are one of the properties that influences cell migration, adhesion and proliferation directly (Tottoli et al. 2020). From this point, the morphologic change in nanofibrous structure before and after doping with

MMT, OMMT and OMMT/B compounds were compared through SEM, and the images with fiber diameter distribution graphs were given in Figure 4.10. As was reported in previous studies, nanoparticle addition may have two opposite effects on the nanofiber network. First, it may increase the viscosity of polymer solutions that may cause bead formation on some occasions. Second, some nanoparticles such as MMT and OMMT can enhance electrical conductivity, which reduces fiber diameter and leads to the formation of a better fibrous network with a more uniform structure (Mushtaq et al. 2020; Palak et al. 2021) The grooved, bead-free and continuous nanofibers with an average diameter of 655±229 nm were obtained from PLA. The formation of grooves in nanofiber structure might be due to the void-based elongation mechanism with two low boiling point solvents where there is enough difference in evaporation rate to form grooved fibers (Liu et al. 2015).

When PLA was doped with MMT, the distribution of the MMT in the polymer matrix was non-homogenous. Although the average diameter of the nanofibers decreased, there were thicker fibers (1344±2304 nm) wherever MMT nanoparticles were present. The standard deviation, which measures how data dispersed, was higher than mean and this result indicated data are more spread out. Probably, this situation revealed because of agglomeration and aggregation of the clay in the polymer solution. Furthermore, SEM images of PLA/MMT revealed numerous pores in their structure interestingly. Prior studies suggested various mechanisms regarding the formation of the pores in the fibrous structure. Since electrospinning is a complicated process, sometimes more than one phenomenon might be responsible for the morphological structure of the fibers (Szewczyk and Stachewicz 2020). As electrospinning was conducted in normal conditions and no additional method was used to increase relative humidity (RH), the formation of the pores is related to the water present in the structure of the MMT. Furthermore, it is well known that composition changes occur in polymer jets during the subsequent solidification process in the case of non-solvent-induced phase separation (NIPS). In this case, phase separation depends on solvent (HFIP)/nonsolvent (chloroform) system, and upon the removal of the polymer-poor regions (HFIP and water), the nanopores are formed on the surface of the fibers. In addition, “breath figures” formation might also be effective in the present case. Chloroform is immiscible with water while HFIP is miscible with water. After rapid removal of the HFIP and water, the polymer jet

gets cooler abruptly and the moisture present in the air condenses on the surface of the PLA which is a hydrophobic polymer and its evaporation leads to the formation of the surface pits (Zhang et al. 2016).

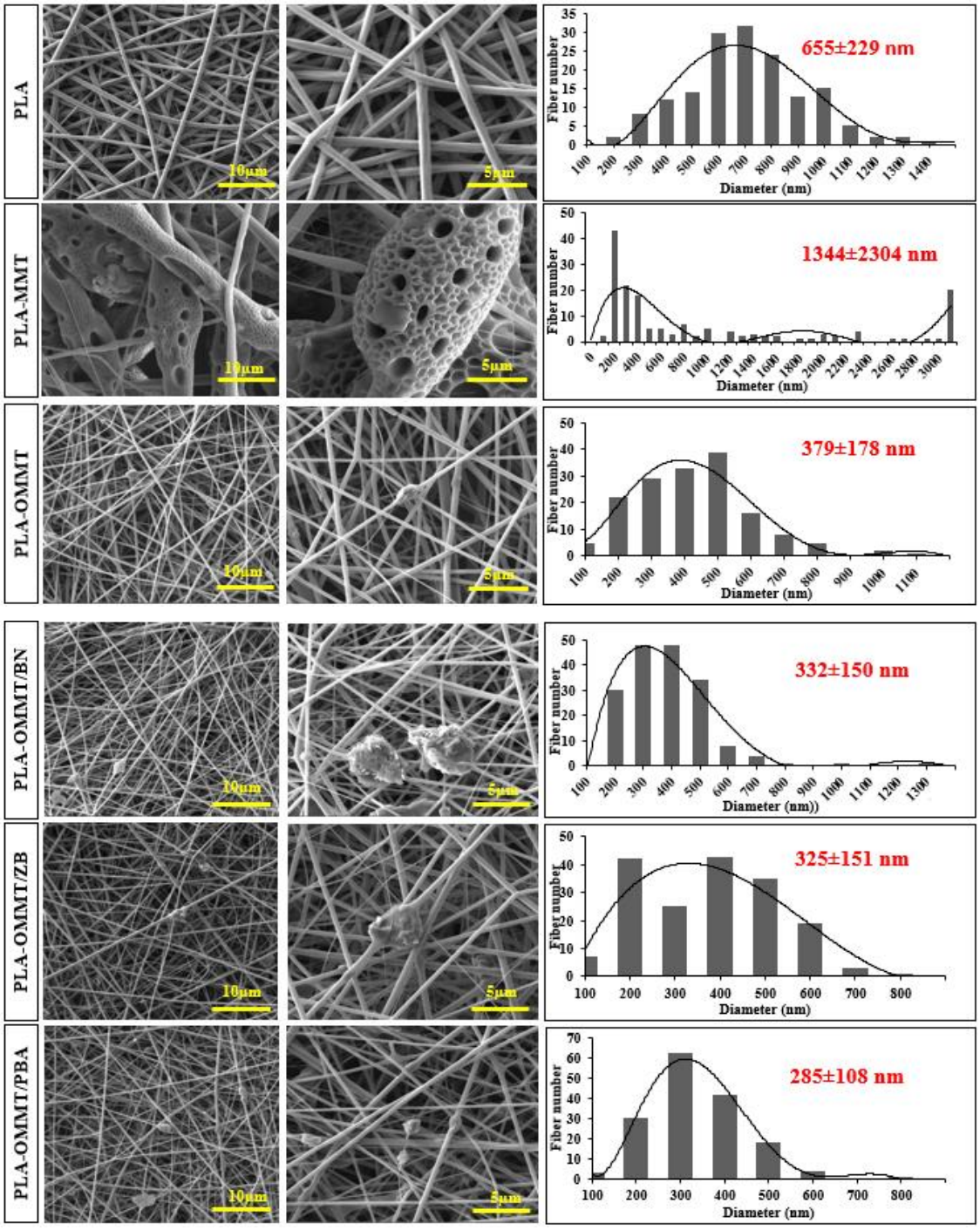

Figure 4.10. SEM images of PLA, PLA-MMT, PLA-OMMT, and PLA-OMMT/B fibrous scaffolds at different magnifications with the optimized electrospinning conditions and diameter distribution graphs.

With the addition of OMMT nanoparticles into PLA polymer solution, the average fiber diameters decrease to 379±178 nm. OMMT improved electrical conductivity of electrospinning solution, which resulted in the formation of thinner nanofiber. The PLA-OMMT nanofibers were produced in continuous form with circular beads that may have formed due to nanoparticle agglomeration (Palak et al. 2021). The better homogenous fibers were formed in the presence of OMMT in comparison to unmodified MMT, which is related to the improved compatibility of PLA and MMT as a result of the organicmodification of the MMT. The modification of MMT formed intercalated composite with PLA, resulting in the better distribution of clay compound in the polymer matrix. Whereas, unmodified MMT forms conventional composite with polymer matrix where the interaction between polymer and clay nanoparticle is limited, since the clay-clay interaction is stronger than clay-polymer interaction (Jaffar Al-Mulla 2011), resulting in non-homogenous fiber formation.

The same behavior as PLA-OMMT was observed for all groups of PLA-OMMT/B nanofibers. The average diameter of PLA-OMMT/BN, PLA-OMMT/ZB, and PLA-OMMT/PBA nanofibers were calculated to be 332±150, 325±151, 285±108 nm, respectively. The better distribution of OMMT/PBA nanoparticles in the PLA matrix may be due to the chemical bonding of PBA and OMMT which led to the formation of much smaller beads. The thinnest fiber diameter belonged to PLA-OMMT/PBA as well which might be due to further enhancement in electrical conductivity when PBA was present in the nanofiber structure. In conclusion, the addition of the OMMT/B particles resulted in the formation of thinner nanofibers. However, fibers without OMMT or OMMT/B were more uniform. It was noteworthy that the structure of the beads formed for each of OMMT, OMMT/BN, OMMT/ZB, and OMMT/PBA was different since the morphology of selected B compounds was completely different from each other.

The CTEM images of the nanofibers given in Figure 4.11. demonstrates that OMMT and OMMT/B particles were able to maintain nano-sized in fibrous structures probably due to the better compatibility of the OMMT and PLA polymer which resulted from organomodification of MMT with quaternary ammonium salt.

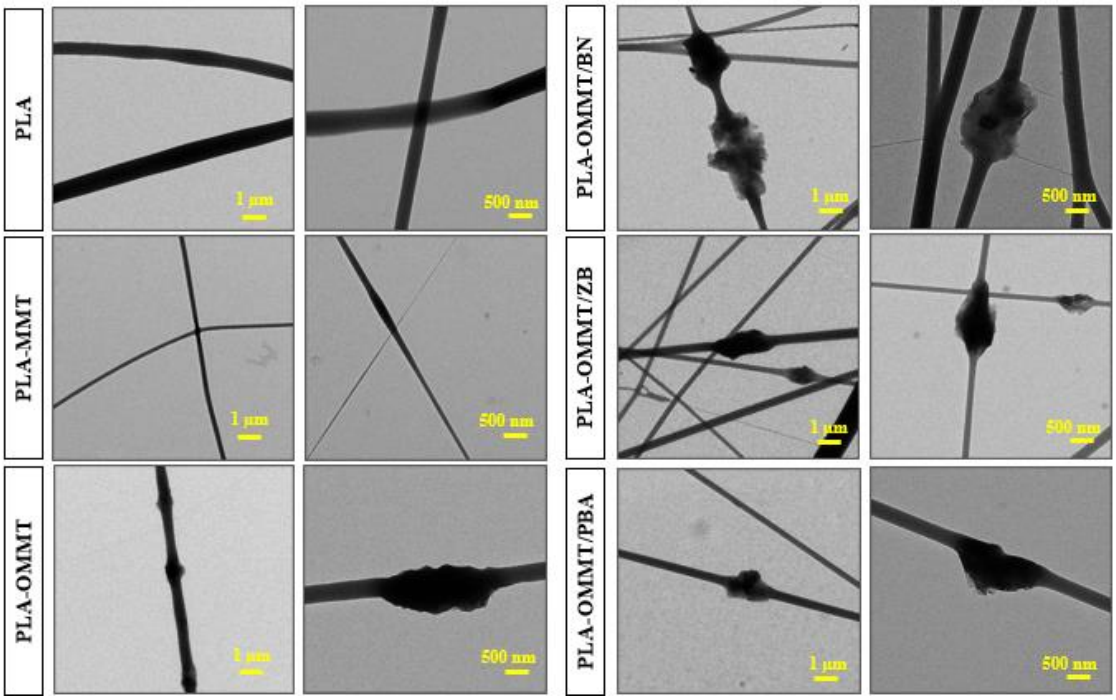

Figure 4.11. The CTEM images of the PLA, PLA-MMT, PLA-OMMT, and PLA-MMT/B hybrid composites at different magnifications.

The surface morphology of the solvent-cast membranes was presented in Figure 4.12. As shown in the SEM images, pure PLA has a smooth, uniform, and layered structure without any holes. The micrographs of PLA-MMT nanocomposite demonstrated a rough surface structure with good distribution and interfacial adhesion of MMT in the polymer matrix. However, some clusters (shown by red arrows) were observed on the surface of the composite membrane which is due to the agglomeration of MMT nanoparticles. On the contrary, the surface morphology of PLA-OMMT nanocomposite indicated a smooth and layered structure, identical to neat PLA, where no cluster was visible. This observation indicated that the modification of MMT nanoparticles resulted in the better distribution of clay nanoparticles in the polymer matrix as was speculated in the solvent-casting method as well.

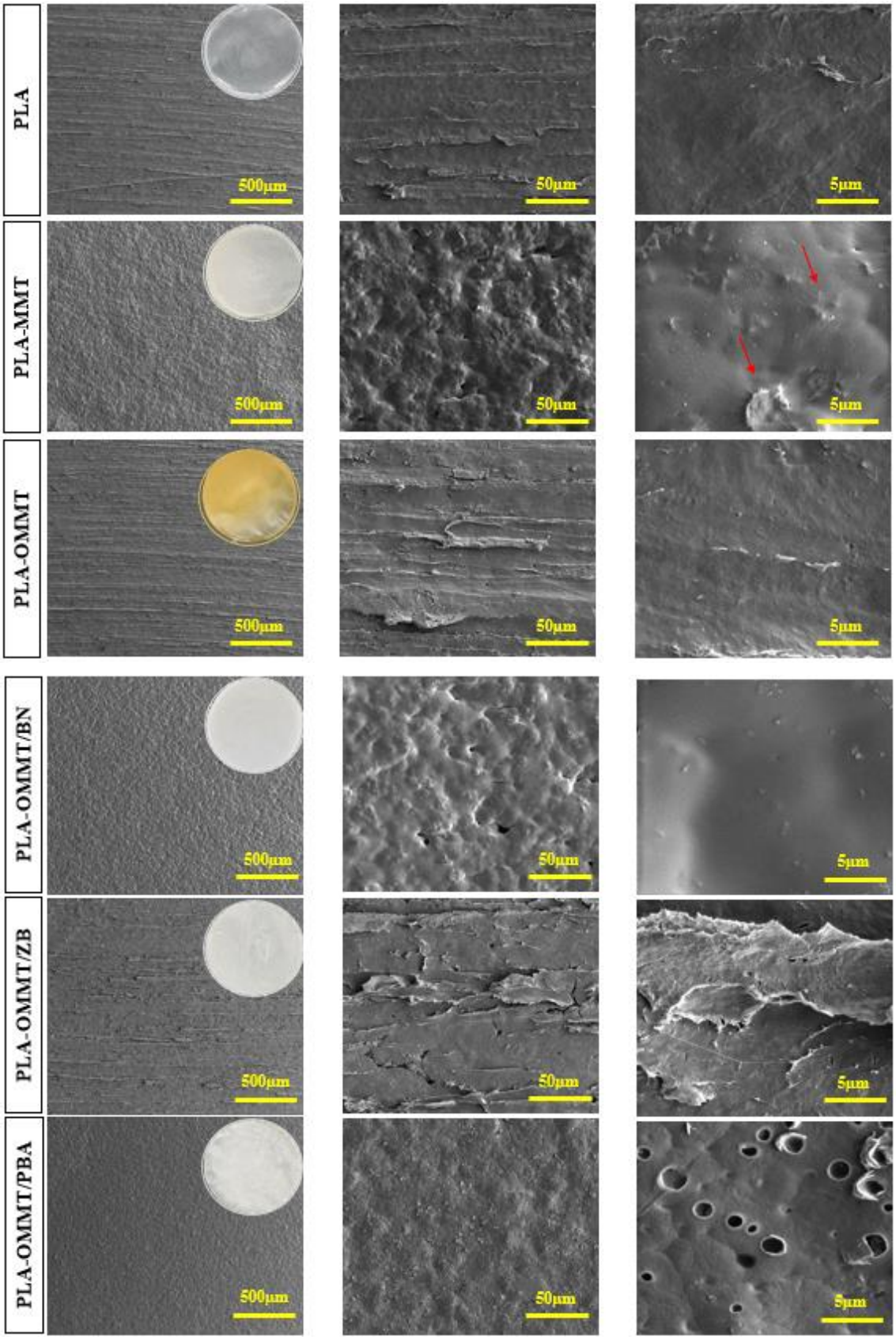

Figure 4.12. Morphological properties of the membranes fabricated via solvent-casting. SEM at different magnifications. Red arrows show agglomeration of MMT.

The surfaces of the PLA-OMMT/BN and PLA-OMMT/PBA hybrid composites showed a rough surface with a few pores on the surface, whereas the presence of pores was more pronounced in PLA-OMMT/PBA structure. On the other hand, some agglomerates of OMMT/BN were visible on the surface of PLA-OMMT/BN, unlike PLA-OMMT/PBA which indicated a more uniform surface morphology. A few pores were observed on the surface of PLA-OMMT/ZB as well but the hybrid composite of PLA-OMMT/ZB demonstrated a layered surface without any visible agglomerates similar to PLA-OMMT and neat PLA morphology. The evaporation of volatile solvent allows the formation of an asymmetrical structure with pores on the surface of membranes during the solvent evaporation and polymer coagulation process (Morgado et al. 2014). Based on the results, the best distribution of filler in the polymer matrix for solvent-cast membranes was observed for the PLA-OMMT composite and PLA-OMMT/ZB hybrid composite, where the least homogenous surface morphology was observed for PLA-MMT composite group.

4.3.4. Biodegradability Test

Biodegradability is an essential property for tissue-engineered products and a wound dressing must be stable meanwhile, it must not cause long-term complications (Op't Veld et al. 2020). To understand the biodegradation behavior of composites and hybrid composites before and after doping with MTT, OMMT, and OMMT/B compounds, solvent-cast membranes and fibrous scaffolds were immersed in PBS that contained lysozyme and the mass loss was weighted at certain intervals and the results were given in Figure 4.13.

In the case of fibrous scaffolds, the degradation percentage increased steadily as the immersion time expanded. The total weight loss of PLA nanofibers after 56 days was 1.77 ± 0.85 %. The degradation of PLA mainly occurs by surface erosion mechanism and this process is usually slow. Furthermore, factors such as high crystallinity and molecular weight reduce the degradation rate of PLA (Ebrahimi and Ramezani Dana 2021; Eng et al. 2013).

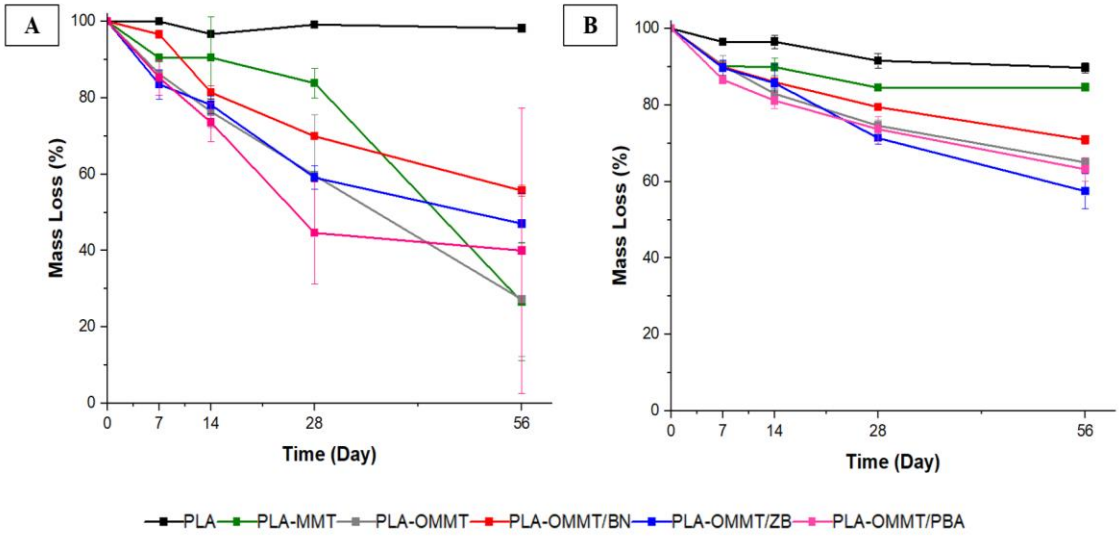

Figure 4.13. Enzymatic degradation results of PLA, PLA-MMT and PLA-OMMT composites, and PLA-OMMT/B hybrid composites. A) Electrospun scaffolds B) Solvent-cast membranes

The PLA-MMT composites degraded slowly for a month and then the degradation improved drastically from the 28th to the 56th day of the test. The total mass loss of PLA-MMT nanofibers after 56 days was measured to be 73.39 ± 15.44 %. The acceleration in the decomposition of PLA can be explained by the relatively high hydrophilicity of the composite due to the presence of nanoclay or the existence of terminal hydroxyl groups in MMT, which improves the diffusion of water into the polymer matrix, leading to faster initiation of the hydrolytic degradation processes, however, it takes some time for unmodified MMT compound to initiate decomposition (Stloukal et al. 2015).

The degradation behavior of PLA-OMMT nanofibers was similar to PLA-MMT nanofibers, where the weight loss of PLA-OMMT after 56 days was 72.79 ± 14.92 %. However, in comparison to PLA-MMT, the weight loss of composites constantly increased by increasing the immersion time. Another parameter that affects the degradation rate of PLA is fiber diameter (Ozbek et al. 2018). In the present work, the modification of MMT initiated the degradation of nanocomposite faster than unmodified MMT, and the low and uniform fiber diameter of PLA-OMMT nanofibers caused regular degradation for up to 56 days.

The addition of B compounds to nanofibrous structure decreased the degradation rate, consequently. The total mass loss after 56 days for PLA-OMMT/BN, PLA-OMMT/ZB, and PLA-OMMT/PBA nanofibers were calculated to be 44.30 ± 1.47, 52.95 ± 8.00, 60.00 ± 37.39 %, respectively. The resistance of BN nanoparticles produced from various precursors against hydrolytic degradation, (Şen et al. 2018) and the inhibitory activity of boronic acid compounds against a variety of enzymes have been reported in prior studies (Yu et al. 2020). Consequently, the incorporation of B compounds decreased the amount of weight loss up to 56 days for hybrid composites fabricated via electrospinning.

Similar to the results of fibrous scaffolds, the lowest degradation amount was observed for neat PLA membrane obtained from the solvent-casting method. The total mass loss after 56 days was measured to be 10.25 ± 1.30 %. The total mass loss of PLA-MMT and PLA-OMMT composites and PLA-OMMT/BN, PLA-OMMT/ZB, and PLA-OMMT/PBA hybrid composites were calculated to be 15.40 ± 0.32, 15.40 ± 0.32, 35.00 ± 1.29, 29.07 ± 1.18, 42.53 ± 4.53, 36.78 ± 3.03%, respectively. The results indicated that the overall degradation percentage for fibrous scaffolds was higher than for solvent-cast membranes. It is evident that the penetration of the water molecules into the fibrous structure is easier than the penetration into the dense structure of membranes. By incorporating MMT and OMMT nanoparticles into the structure of membranes, the degradation of the neat polymer increased as expected, however, the enhancement in degradation was more pronounced in the presence of OMMT which can be explained by the interaction type between the polymer and the clay compound in the modified and unmodified state. The well-known effect of MMT nanoclay is to increase the water affinity of PLA which consequently increases the degradation rate of the polymer. Yet, the homogeneous dispersion of OMMT in the PLA matrix improved the degradation of the membrane more effectively than MMT.

The degradation rate of the hybrid composites that contained B compounds in their structure was close to each other during the test for all determined days. The highest degradation percentage was observed for PLA-OMMT/ZB hybrid composite among all tested groups with a total weight loss of 42.53 ± 4.53 after 56 days. The biodegradation

results were in agreement with SEM micrographs, where the membranes with homogenous distribution improved the degradation of the membranes more effectively.

4.3.5. Mechanical Test

The importance of the mechanical properties of scaffolds on the adhesion, stretching and proliferation of fibroblast had been vastly discussed in the literature (Boddupalli et al. 2016). Mechanical tests were conducted to assess the tensile strength, breaking strain, toughness, and elastic modulus of the electrospun scaffolds and solvent-cast membranes. The results were summarized in Table 4.2.

Table 4.2. Mechanical characterization of fibrous scaffolds and membranes obtained via electrospinning and solvent-casting methods utilizing OMMT and B compounds.

	Groups	Tensile strength (MPa)	Breaking strain (%)	Toughness (MPa)	Elastic modulus (MPa)
Electrospinning	**PLA**	14.95±1.41	132.87±12.72	3.92±1.06	591.10±183.72
	PLA-MMT	4.52±0.91	147.88±10.35	1.89±0.81	88.20±6.26
	PLA-OMMT	9.88±0.57	104.00±1.58	2.38±0.31	137.47±46.53
	PLA-OMMT/BN	10.99±1.17	125.74±0.23	2.16±0.13	245.13±29.54
	PLA-OMMT/ZB	10.36±0.46	123.30±1.53	1.97±0.70	314.43±24.47
	PLA-OMMT/PBA	10.53±1.32	85.45±6.67	1.46±0.59	371.97±46.86
Solvent-Casting	**PLA**	193.85±42.23	291.12±58.99	354.73±172.48	1476.07±287.97
	PLA-MMT	86.40±16.32	106.71±1.37	4.13±0.84	4782.07±1045.79
	PLA-OMMT	111.27±24.38	103.47±0.33	2.49±0.67	5833.76±1286.71
	PLA-OMMT/BN	115.75±8.55	102.42±0.31	1.53±0.29	7523.80±576.87
	PLA-OMMT/ZB	5.79±2.23	100.62±0.14	0.01±0.00	1385.06±908.71
	PLA-OMMT/PBA	103.36±13.30	104.27±1.50	2.81±0.65	5462.27±666.03

Based on the results, for the fibrous scaffolds, the tensile strength was negatively affected by the addition of MMT, and the value decreased from 14.95±1.41 to 4.52±0.91 MPa when compared to neat PLA. Toughness and elastic modulus values also followed similar trends. The mechanical durability of fibrous scaffolds mostly depend on the filler

mechanical features, the amount of filler doped in a polymer matrix, fiber morphology, and the interaction between polymer and filler (Jaffar Al-Mulla 2011; Rashid et al. 2021). When clays are used as fillers, the low amount of the clay enhances interfacial adhesion, leading to compatibilization at a molecular level between polymer and clay compound, which improves stress transfer within the composite and eventually, enhances the tensile strength. However, further incensement in the clay content decreases the tensile strength as the homogeneity of the fibers decreases due to agglomeration and aggregation of clay (Eng et al. 2013). The morphology of the PLA-MMT scaffolds that were elucidated by SEM images, revealed the formation of aggregates in the fibrous structure. Moreover, fibers indicated porous morphology. It is reasonable to assume that porosity have caused the reduction in the tensile strength, toughness, and elastic modulus of the conventional composite of PLA-MMT. On the other hand, the breaking strain of the PLA increased with the incorporation of the MMT compound into the structure. Similar results were observed for polypropylene/poly(ethylene terephthalate) blends containing MMT, suggesting that the addition of MMT improves the stress transfer that led to higher values of breaking strain (Calcagno et al. 2008). With the inclusion of OMMT in the PLA matrix, tensile strength increased to 9.88±0.57 MPa in comparison to unmodified MMT, and a similar trend was observed for toughness and elastic modulus values. One of the distinguishing features of clay nanoparticles on the polymeric matrix is the increase in the stiffness of polymers owing to the high specific surface area of the clay compounds. However, the agglomeration of beads decreased the interaction between polymer and silicate layers of clay compound. The reduction in the stiffness values of composites was more pronounced for unmodified MMT rather than OMMT. The overall enhancement in the mechanical properties of PLA-OMMT in comparison to the PLA-MMT nanocomposite is relatable to the better distribution of the OMMT in the polymer matrix and the formation of a more uniform fibrous structure.

The addition of B compound into the structure improved the tensile strength and elastic modulus of the nanofibers due to the intrinsic mechanical features of B compounds individually. The lowest elongation at the break value belonged to PLA-OMMT/PBA group due to the limited interactions between the polymeric chain and OMMT/PBA compound. As was described before, PBA was chemically adsorbed on OMMT nanoclay which may limit the interaction between OMMT and PLA chains.

For solvent-cast membranes, the values of tensile strength, elastic modulus, toughness, and breaking strain were higher than in nanofibrous scaffolds. As common knowledge, different fabrication technologies result in the formation of various structures with varying properties. For solvent-cast membranes, the tensile behavior is mainly influenced by the physical features of the polymer and the molecular chain arrangement and inter-chain interactions whereas for randomly oriented nanofiber scaffolds, tensile behavior greatly relies on fiber morphology (Tarus et al. 2020). In the process of membrane formation, during the evaporation of the organic solvents, the concentration of polymer increases, and the interdiffusion of polymeric chains form solvent-free membranes. The evaporation process of the organic solvents was much longer for solvent-cast membranes, hence polymeric chains had sufficient time to rearrange and form a bulk structure with higher mechanical endurance.

Similar to the results of fibrous scaffolds, the incorporation of MMT negatively affected the breaking strain, tensile strength, and toughness of the composite membranes, however, the elastic modulus of the PLA-MMT membranes was measured to be 4782.07±1045.79 MPa which was by far higher than neat PLA membrane. As explained before, polymeric chains can be physiosorbed on the silicate surface of MMT and get stiffened. In the membrane formation process, the complete evaporation of the organic solvents takes place in a day. This considerable long time allows sufficient time for the polymeric chains to get adsorb on the silicate surface of MMT and get stiffer through their interaction. The elastic modulus of the PLA-OMMT composite membranes was 5833.76±1286.71 MPa which was even higher than the value measured for PLA-MMT. The higher value can be ascribed to the better interaction of the PLA chains and OMMT nanoparticles as a result of the organomodification of MMT.

The tensile strength and elastic modulus of the membrane samples were improved with the addition of BN nanoparticles. Similar behavior was also observed for fibrous scaffolds. The improvement is relatable to the interaction of polymer chains and ceramic nanoparticles such as BN which improves the mechanical properties of the hybrid composite structure (Ozbek et al. 2018). The incorporation of ZB into the composite structure demolished the mechanical behavior of the membrane where the tensile strength

of the membrane decreased to 5.79±2.23 MPa. It is worth mentioning that the preparation of the samples for the tensile test was challenging for the mentioned group due to the brittleness of the membranes. In the literature, there are various reports about the impact of the ZB on the mechanical durability of the polymers, most of them reporting the favorable influence of the ZB on the mechanical characteristics of the composite (Ramazani et al. 2008; Younis 2022). However, there are also reports that have mentioned the impact of ZB on the brittleness of the composite structure, resulting in the reduction of mechanical endurance and early failure. The incorporation of ZB nanoparticles resulted in the formation of brittle hybrid composites in the solvent-cast membranes, however, the ZB nanoparticles in the structure of PLA-OMMT/ZB fibrous scaffolds enhanced the mechanical properties when compared to the PLA-OMMT composites. The distinct difference in the behavior of PLA-OMMT/ZB hybrid composites fabricated by solvent-casting and electrospinning methods clearly shows the influence of the fabrication method on the mechanical characteristics. The mechanical properties of the PLA-OMMT/PBA membranes were quite similar to the PLA-OMMT group which means the presence of PBA had no impact on the mechanical properties of membranes.

These results showed that doping of OMMT/B to PLA decreased the tensile strength and elasticity of the neat polymer. However, these values were well within the range for skin tissue engineering products. In the literature, there are various values reported for the biomechanical properties of the skin. The variability may be due to the tissue storage and preparation protocols, mechanical test conditions, and sample orientation concerning contour lines of tension (Langer's line) (Annaidh et al. 2012; Griffin et al. 2017). The skin was found to be highly anisotropic and viscoelastic, with a range of Young's Modulus between 5 kPa and 140 MPa (Kalra et al. 2016). Yang et al. found the strength of rabbit skin as 8–15 kPa which is consistent with human skin that was tested simultaneously and perpendicular to Langer's lines (Yang et al. 2015). The results found in this study were comparable to the literature and scaffolds developed here, especially fibrous scaffolds, showed excellent mechanical properties in terms of tensile strength and elasticity.

4.3.6. Water Contact Angle Measurement

Wettability is important factor that affects adhesion, migration, and proliferation of the cells and it can be evaluated by measuring the water contact angle (Tottoli et al. 2020). To understand the hydrophilicity of scaffolds, water contact angle measurements were carried out (Figure 4.14.)

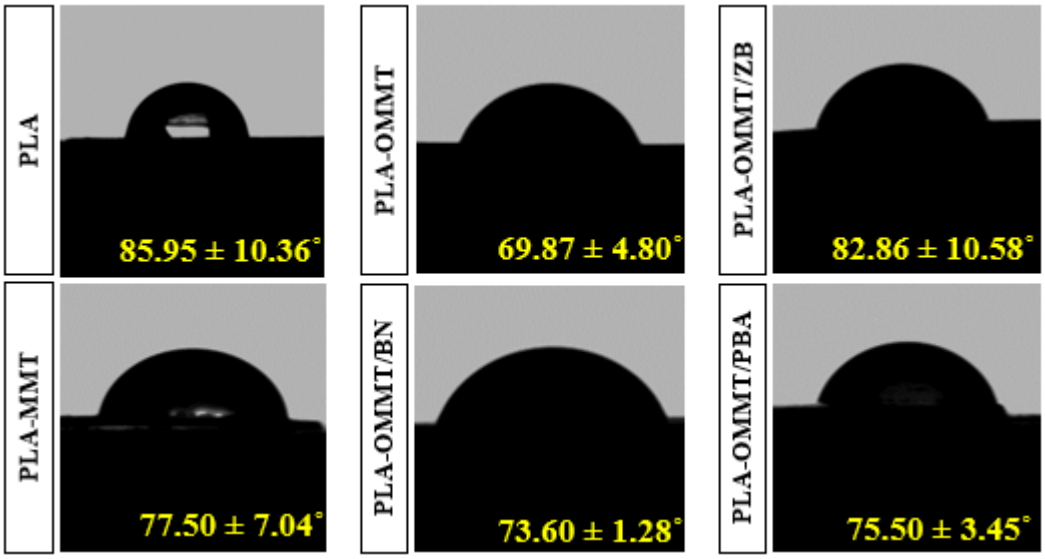

Figure 4.14. Water contact angles of the membrane samples.

Although PLA is a non-toxic polymer approved by the Food and Drug Administration (FDA) that is vastly used for the development of materials in tissue engineering, it fails to support cell attachment and spreading because of its high hydrophobicity (water contact angle: 85.97±10.36°). After the addition of nanoclay, the water contact angle was reduced to 69.87 ± 4.80° for PLA-OMMT scaffolds as expected (Ghaemi et al. 2011). However, B addition did not severely influence the affinity of the scaffolds toward water molecules.

Based on the results of characterization tests and analysis conducted on the fibrous scaffolds and solvent-cast membranes, the effect of the fabrication method on the resultant products has been shown. Although the materials that constitute the composite material and the doping ratios were identical, the composites and hybrid composites formed by different production methods indicate prominent features. The nonexistence

of a dynamic environment during the membrane formation in the solvent-casting method reduces the homogeneity of the membranes. The lack of homogeneity negatively affects the physical and chemical properties which were observed throughout the tests and analysis carried out, hence, it was decided to continue the remaining analysis with the fibrous groups only.

4.3.7. TGA

Thermal properties of polymers can be promoted by introducing fillers to the polymeric matrix and the impact of incorporated particles can be observed from the excess residual content and the improvement in thermal degradation temperature (Khalili et al. 2019). The thermal stability of PLA, PLA-MMT and PLA-OMMT composites, PLA-OMMT/B hybrid nanofibers were given in Table 4.3. through their TGA profiles.

Table 4.3. Mechanical characterization of fibrous scaffolds and membranes obtained via electrospinning and solvent-casting methods utilizing OMMT and B compounds

Groups	Mass loss I (%) / Onset temperature (˚C)	Mass loss II (%) / Onset temperature (˚C)
PLA	1.60 / 73.37	94.78 / 352.34
PLA-MMT	6.30 / 60.58	69.59 / 309.49
PLA-OMMT	-	75.02 / 340.40
PLA-OMMT/BN	-	75.87 / 321.43
PLA-OMMT/ZB	-	78.75 / 322.66
PLA-OMMT/PBA	-	77.16 / 323.09

PLA lost 1.6% of its initial weight at a temperature of ~75 ˚C, which was ascribed to the removal of moisture (Belaid et al. 2020). Approximately 95% of the initial weight of PLA nanofibers lost due to thermal degradation of PLA at a temperature of 336 ˚C. The decomposition of PLA-MMT took place in two stages. In the first step, the weight loss due to the elimination of water molecules occurred at 60 ˚C and the composite lost 6.29%

of its initial weight. By incorporating MMT into the structure of the nanofibers, the amount of water increased in the composite structure due to the existence of water molecules in the hydrophilic structure of MMT. At the temperature of 309 ˚C, due to the thermal degradation of PLA, 69.6% of the composite was decomposed. The addition of MMT affects the residual weight of the PLA-MMT nanofibers to increase by 24.11%. The incorporation of MMT into the PLA matrix results in the formation of a barrier that delays the release of thermal degradation products (Eng et al. 2013), which is the reason behind excess residual observed for PLA-MMT composite. Generally, the release of water vapor released by the filler promotes the thermal decomposition of composite by absorbing the heat and decreasing the temperature in the burning zone (Khalili et al. 2019). However, it can oxidize the volatile products of thermal decomposition generated by polymer and accelerate thermal degradation. The last explained effect causes of the deduction in onset degradation temperature of the second step in the case of PLA-MMT. The weight loss of the PLA-OMMT nanofibers occurred in one step. In an intercalated type of composite, the polymer chains enter into the galleries of the clay compound, and the main enthalpy needed for polymer and clay interaction is provided by the freedom of many desorbed molecules such as water molecules (Chen 2004). The weight loss related to water molecules observed for OMMT was not observed for PLA-OMMT composites. The restriction of –OH peaks in the FTIR spectrum of the PLA-OMMT composite and the nonexistence of the weight loss regarding adsorbed water molecules demonstrates the intercalated composite formation. The addition of OMMT affects the residual weight of the PLA-OMMT nanofibers by 25%. Dispersion of OMMT layers within the polymer causes a barrier property that enhances the thermal stability (Ramesh et al. 2020).

A similar trend was observed for all groups of PLA-OMMT/BN, PLA-OMMT/ZB, and PLA-OMMT/PBA nanofibers. The mass loss occurred at one step with no significant change in onset degradation temperature for nanofibers that contained B in their structure. The mass loss for PLA/OMMT/BN, PLA-OMMT/ZB, and PLA-OMMT/PBA nanofiber were observed to be 75%, 79%, and 77%, respectively. The modest decrease in the amount of residue might be due to the decomposition of ZB and PBA that happened at temperatures around 350 ˚C (Adamczyk-Woźniak et al. 2018; Younis 2022).

4.3.8. DSC Analysis

By performing DSC analysis the glass transition temperature (T_g), melting temperature (T_m), and degree of crystallinity (%) of nanofibers were defined, and the result were given in Table 4.4.

Table 4.4. Summary of differential scanning calorimetry results of PLA, and PLA-based hybrid composites of OMMT and B compounds.

Groups	Glass transition temperature (˚C)	Melting temperature (˚C)	Crystallinity (%)
PLA	60.93	175.52	48.00
PLA-MMT	81.66	176.85	28.00
PLA-OMMT	71.19	178.29	58.00
PLA-OMMT/BN	71.25	177.92	43.00
PLA-OMMT/ZB	70.12	175.33	39.00
PLA-OMMT/PBA	69.90	175.58	37.00

For PLA, T_g is 60 ˚C. The inclusion of MMT and OMMT into the PLA matrix raised the T_g to higher temperature. This behavior was commended to the restricted segmental movements of the intercalated organic-inorganic interface (Zhou and Xanthos 2009). The T_m of PLA was 175 ˚C and increased slightly to 176 and 178 ˚C, respectively with the addition of MMT and OMMT but the addition of B compounds decreased the T_m to temperatures around 175 ˚C. The degree of crystallinity decreased severely when MMT was incorporated on the PLA matrix, however, the incorporation of OMMT increased the degree of crystallinity to 58%. Yet, the crystallinity of PLA decreased once again after the addition of B compounds. The improvement in the crystallinity of PLA after incorporation of the OMMT suggested that the clay acted as a heterophase nucleating agent that increases the crystallization rate of the PLA matrix. However, after the addition of B compounds and crystallinity values were reached even lower than the degree of crystallinity of PLA. It means heterogeneous nucleation led to the formation of the more defect-ridden crystalline lamella, and less ordered crystals of PLA is formed (Fukushima et al. 2011). The formation of less ordered crystalline lamella of polymer was also

observed for PLA-MMT composite that addition of MMT nanoparticles decreased the degree of crystallinity. This might be the reason for the modest decrease in T_m values when the B compounds were added.

4.3.9. Water Uptake Capacity Test

A potential material that is going to be used as a skin tissue engineered product is required to adsorb a certain amount of fluid as it must remove extra exudates secreted by wounded tissue. The complete removal is not preferred due to the favorable functions of exudate in the migration and proliferation of keratinocytes and fibroblasts, which might reduce the healing time and improve the overall cascade (Golafshan et al. 2017). Thus, management of exudate adoption is one of the undeniable properties of wound dressings. The water uptake capacity test outcomes of fibrous scaffolds were shown in in Figure 4.15.

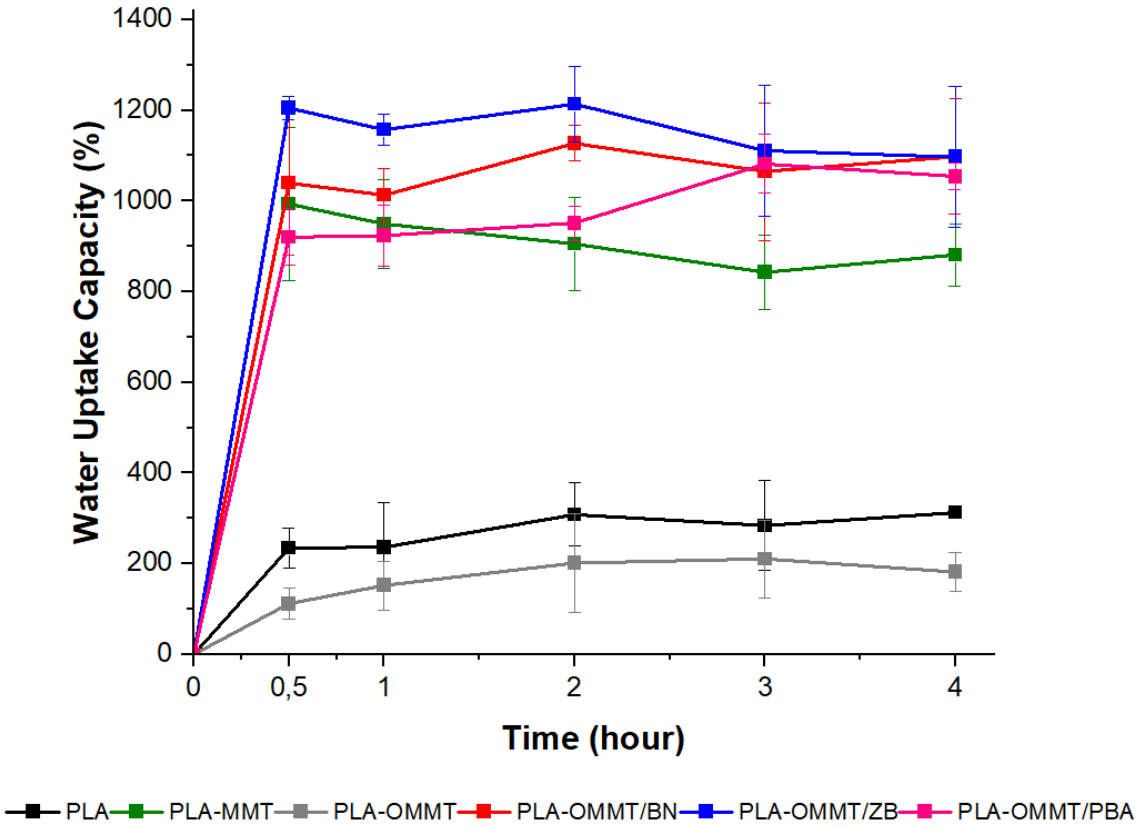

Figure 4.15. The water uptake capacities test results for PLA and PLA-based hybid composites of OMMT and B compounds.

The tendency of MMT nanoparticles to absorb water due to their highly hydrophilic nature is acknowledged. However, the affinity of MMT nanoparticles toward water is strongly dependent on the type of exchangeable interlayer cations (Chiou and Rutherford 1997). During organomodification of MMT, small cation molecules of the clay compound (Na^+ and Ca^{2+}) were replaced by $(CH_3)_3(CH_2)_{17}N^+$ cations which decreases the water uptake capacity of the PLA-OMMT scaffolds. In contrast, the addition of the B compound to the fibrous scaffolds increased the water uptake capacity considerably. The presence of the B compounds in the fibrous structure presents new sights for water molecules to bond with and increased the water uptake ability of the PLA-OMMT/Bs.

4.4. Antibacterial Study

The bacterial infection can lead to a prolonged inflammatory phase in the healing cascade and in the case of proceeding, the wound may enter a chronic state and fail to heal (Silva et al. 2018). Therefore, antibacterial activity is one of the crucial properties of a wound dressing material. The effects of various sterilization techniques such as autoclave, ethanol, UV, and Eth/UV combined method as immersing scaffolds in ethanol solution for 30 min, then applying UV on each side for an hour were investigated (Figure 4.16.) before performing the antibacterial assay.

The fibrous structure of all groups seemed to be unchanged after the sterilization process using UV radiation. However, after the sterilization process of ethanol washing and autoclaving, side effects such as the reduction in fiber diameter and deformation of the fibrous structure were observed. Furthermore, according to TGA results, PBA loses approximately 15% of its initial weight at 90 °C. For Eth, deformation and cohesion of the fibrous structure were observed being the reason for pores closure based on Eth applying time. However, according to the contamination test in DMEM-HG medium for 7 days, UV radiation alone was not sufficient for sterilization of the thick and compact fibrous scaffolds (100-250 µm). Therefore, a combined method of Eth/UV was applied to the scaffolds as a sterilization method, and Eth:UV (0.5:(1/1)) was chosen instead of Eth:UV (1:(1/1)) to decrease Eth time before the antibacterial and cytotoxicity assay.

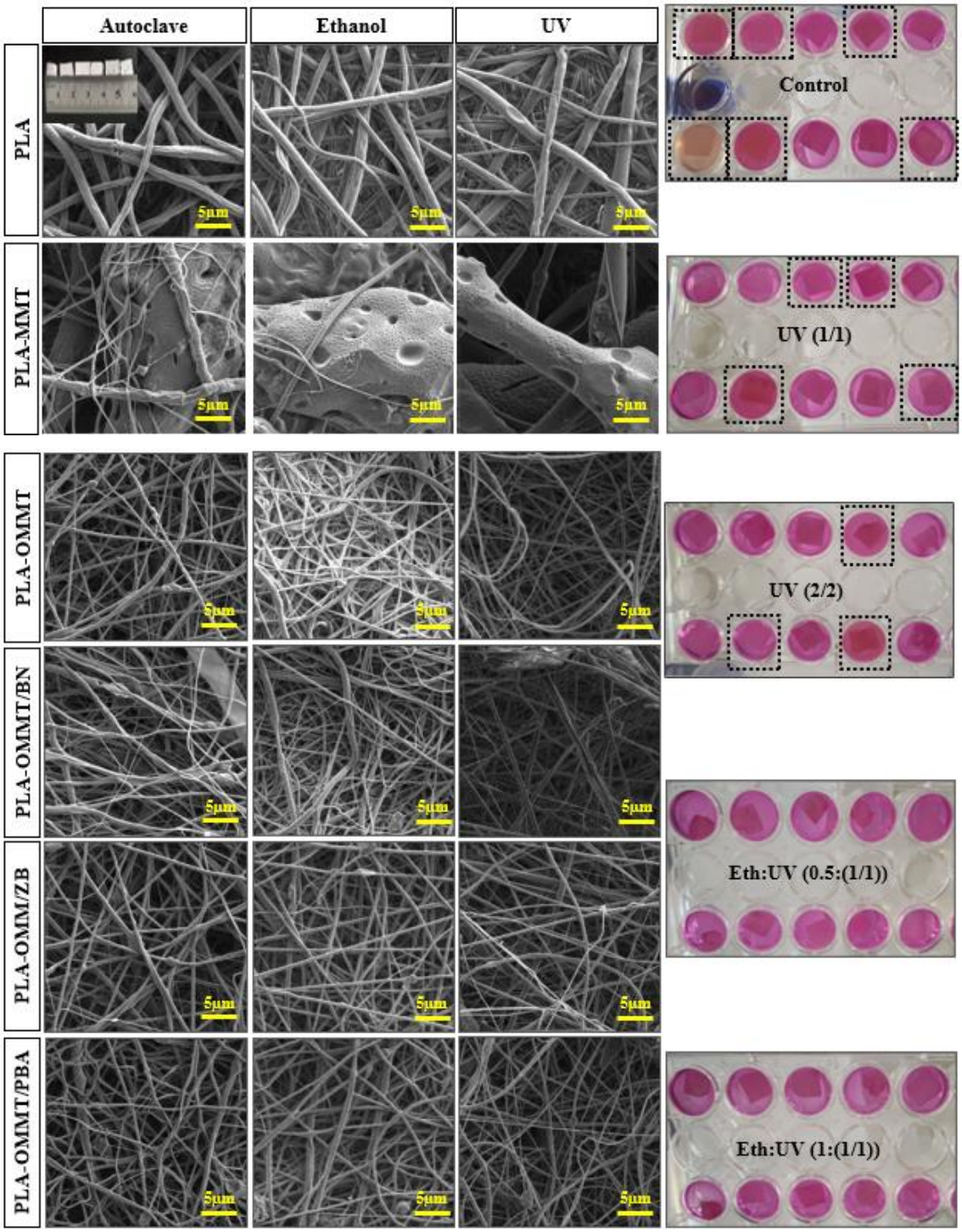

Figure 4.16. The changes in the fibrous structure that occur after applying different sterilization methods A) SEM images of fibrous groups after applying autoclave, Eth, and UV sterilization methods. B) The results of contamination test after 7 days.

Among all these factors that can lead to a prolonged healing process, bacterial infections are a significant contributor. The colonization of bacteria alters the metabolic activity which negatively affects the wound closure capability. Furthermore, biofilm formation hinders the dispersal of locally delivered medications (Laurano et al. 2022). Consequently, a promoted wound healing process can be obtained by dressing processing antibacterial properties.

The antibacterial assay was performed on the scaffolds against pathogenic gram-negative *E. coli* and gram-positive *S. aureus* bacteria employing the agar disk diffusion and optical density (OD) methods based on Clinical & Laboratory Standards Institute (CLSI) standards. For the agar-disc diffusion method, bactericidal properties of materials got shown as halo zones formed around the scaffolds. The images presented in Figure 4.17. demonstrate the bactericidal effect of PLA-OMMT/ZB and PLA-OMMT/PBA nanofibers against both bacteria, while PLA-OMMT/BN possesses bactericidal activity only against gram-positive bacterium. PLA, PLA-MMT and PLA-OMMT did not show any clear zone formation against both strains of bacteria. To determine the quantitative bacteriostatic effect of scaffolds on the proliferation rate of both bacterial strains in the liquid media, the OD method was performed for 24 h. Based on the results, the inclusion of MMT into a polymeric basis, the resulting PLA-MMT scaffold inhibits the proliferation *S. aureus* more than *E. coli*. Fibrous samples of PLA-OMMT/ZB and PLA-OMMT/PBA scaffolds exhibited toxicity toward *E. coli* during 24 h. The PLA-OMMT and PLA-OMMT/BN scaffolds failed to demonstrate any significant inhibition against the growth of *E. Coli*. Interestingly, PLA-OMMT and all of the PLA-OMMT/Bs exhibited strong toxicity toward *S. aureus* during 24 h.

In the case of PLA-MTT scaffolds, it was mentioned that the presence of unmodified MMT (Ca-MMT and Na-MMT) in the structure affects the adsorption of toxic substances and microorganisms, but does not demonstrate a significant antibacterial effect (Malachová et al. 2009; Ul-Islam et al. 2013). Even so, in a few reports that unmodified MMT was incorporated into composite structure, the CFU (colony forming units) of *S. aureus* and *E. coli* got lowered, describing that bacterial cells were attached and accumulated on MMT, leaving a bacterial biofilm filled with dead and lysed cells

(Malachová et al. 2011). Yet, the inhibitory effect was more pronounced against the gram-positive bacterium. *S. aureus* is famous for its staphylococci (grape-like clusters) appearance and has large, round, golden-yellow colonies when visualized by microscope. (Ray and Ryan 2010).

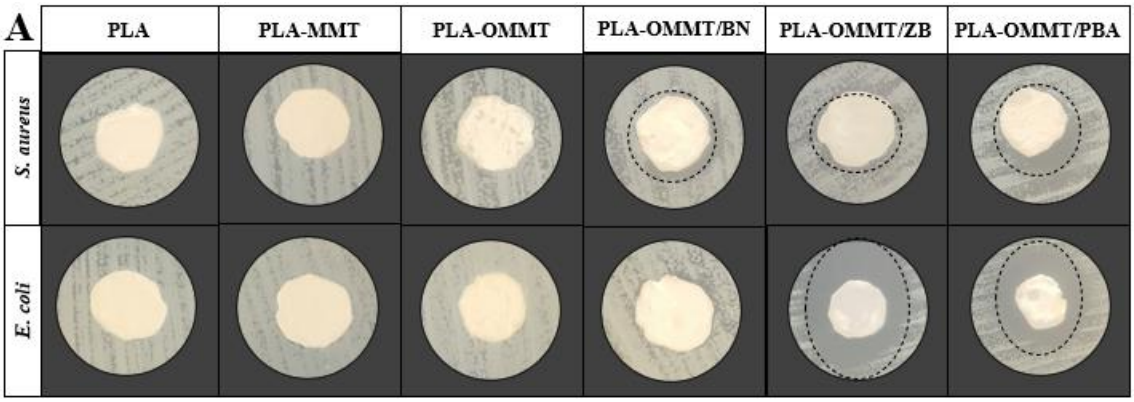

B

Groups	Zone diameter (mm)	
	S. aureus	*E. Coli*
PLA	-	-
PLA-MMT	-	-
PLA-OMMT	-	-
PLA-OMMT/BN	10.67±0.58	-
PLA-OMMT/ZB	10.11±0.57	14.50±4.95
PLA-OMMT/PBA	11.50±0.71	11.67±1.52

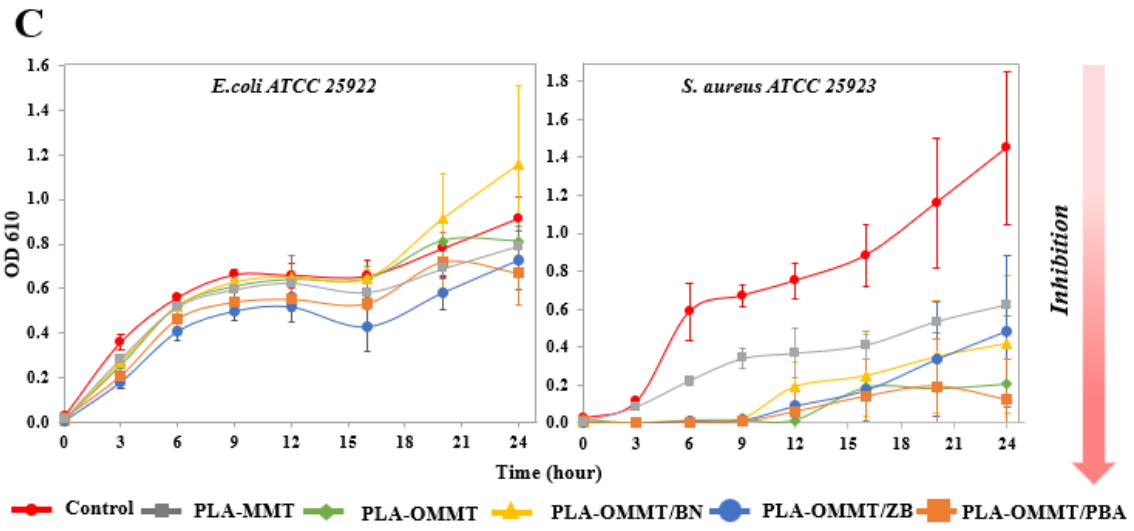

Figure 4.17. Antibacterial activity studies of OMMT and B-containing fibrous scaffolds against pathogenic *E. coli* and *S. aureus* bacteria A) The disc diffusion method B) Calculation of zone diameter formed in disk diffusion method for all groups. C) The optical density method.

The accumulation of *S. aureus* on MMT hinders the cell-cell interaction of bacterial cells and limits the growth of the bacterium which gradually leads to cell death. The quaternary ammonium salts such as TMOD are able to modify the permeability of cellular membranes. The nutrients needed for cellular metabolism that possess low molecular weight and intercellular ions scatter out of the cells and the attempt of bacterial cells to maintain homeostasis leads to cell death, eventually. The simple and more permeable cell wall structure of gram-positive bacteria strains such as *S. aureus* makes them more vulnerable to quaternary alkyl ammonium salts such as TMOD (Malachová et al. 2009).

An inhibition zone of ~14 mm for *E. coli* and a ~10 mm zone of inhibition for *S. aureus* was formed around PLA-OMMT/ZB, and significantly inhibiting the proliferation of *E. coli* in the OD method, which demonstrated bactericidal and bacteriostatic effects of PLA-OMMT/ZB scaffolds. It might be due to the presence of zinc particles in fibrous structures. Previous studies evaluated the antibacterial effect of the borate-based bioactive glasses and stated that the presence of Zn^{2+} raised the antibacterial effect of bioactive glasses against gram-negative and gram-positive bacteria (Jung et al. 2019). Both bacteria showed an inhibition zone of ~11 mm for the PLA-OMMT/PBA, and also inhibited the growth of *E. coli.* This result confirmed the antibacterial effect of PLA-OMMT/PBA on both bacteria. In conclusion, modification of MMT nanoclay with TMOD resulted in the formation of fibrous scaffolds that reveals an undeniable inhibitory against the growth of *S. aureus* bacterium. In the presence of ZB and PBA compounds, nanofibers indicated bacteriostatic effect toward gram-negative strain as well as demonstrating bactericidal effect toward both types of bacteria.

4.5. *In-vitro* Cell Culture Studies

4.5.1. Cytotoxicity Test

To be certain of the OMMT effect on the fibroblasts, the cytotoxicity test was conducted for the PLA-OMMT scaffolds. Since cytotoxicity is dose-dependent, various extracts of the PLA-OMMT scaffold were tested. The scaffolds were placed in sterile tubes containing cell culture media. After 1, 2, and 3 days the extracts were removed and filtered. The 100% extract (without dilution), 50% extract (50% of extract and 50% fresh media), and 25% extract (25% extract and 75% fresh media) were prepared and when the

cells seed on TCPS plates reached confluency, the media were added on top of the cells. The viability was monitored for 3 days, and the outcomes were depicted in Figure 4.19.

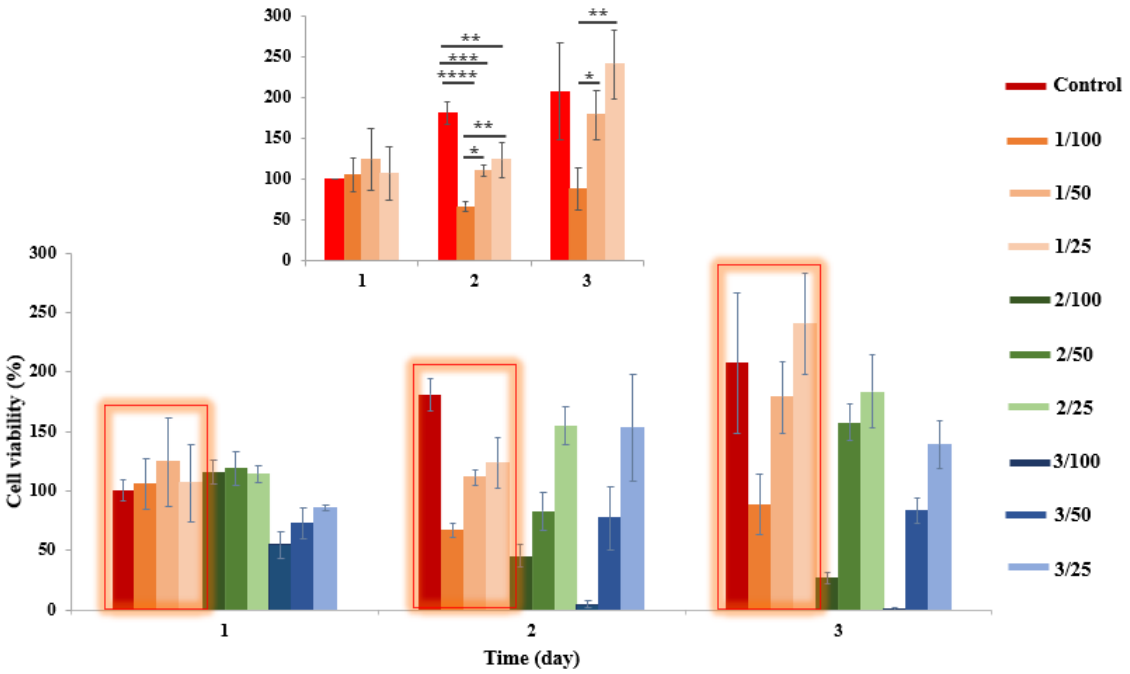

Figure 4.18. Cytotoxicity results of nanofibrous PLA/OMMT scaffolds for 3 days at different extracts (100%, 50%, and 25%) of various days (1,2, and 3). Control indicates that cells were cultured on TCPS. Statistically significant differences were observed between groups in the same analysis day: n = 3; $*\ p < 0.05$, $**\ p < 0.01$, $***\ p < 0.001$, $****\ p < 0.0001$.

Based on ISO 10993-5/EN 30993 standards, the cytotoxicity of newly-developed biomaterial can be defined through a cell viability test. When the viability is under 70% in an indirect test, the material is cytotoxic and not suitable to be used in biomedical applications. Based on the results, the cytotoxicity was noticed only for 100% extracts of the 2nd and 3rd days, shown in Figure 4.19. as 2/100 and 3/100 bars. It is reasonable to assume that the concentration of OMMT released to the culture media increases as the immersion time continues. As the concentration of the OMMT increases in the media, cell viability decreases. During cell culture studies, it was suspected that organomodification of the MMT might be the cause of cell death during the culture studies and the results of the cytotoxicity test confirmed the dose-dependent cytotoxic

effect of the OMMT on NHDF cells. Later, the effect of 1st-day extracts of OMMT on NHDF cells with different dilutions was investigated in more detail.

The results in the smaller chart of Figure 4.19. separately demonstrated that on the first day of culture, the cell viability of all extract dilutions was higher than the control but there is no statistical difference among them. On the 2nd day, cell viability of 100% *($p < 0.0001$)*, 50% *($p < 0.001$),* and 25% (*$p < 0.01$)* extract decreased when compared to the control. On the 3rd day of culture, the cell viability of all delusions of extracts increased in comparison with the 2nd day, and the 25% extract indicated the highest cell viability. As far as we know, a limited number of studies explored the cytotoxic possibility of quaternary ammonium salts on fibroblast cells. In one of the previous researches, quaternary ammonium salts with varying chain lengths were grafted on polyvinyl alcohol-formaldehyde sponges, evaluating their cytotoxicity effect on mice fibroblast cells (L929). It was reported that no significant cytotoxic effect was observed in the cell viability of the sponges up to 0.5 g/mL concentration for 3 days (Sha et al. 2021). Although the concentration of OMMT compounds in nanofiber structure was 0.04 g/mL in this study, there was a modest cytotoxic effect on NHDF cells on the second day (cell viability of ~66% for 100% extract) which might be due to the presence of TOMD in the OMMT structure. In contrast, the cell viability of all extracts on the 3rd day was higher than ~80% and the cell growth rate continues to increase till the 3rd day which means scaffolds might be suitable for short-term wound dressing applications.

4.6. Fabrication of PLA-MMT/B Composites

After the cytotoxicity test results of OMMT-containing scaffolds, three groups of fibrous scaffolds were added to the scope of the thesis as PLA doped with BN adsorbed MMT (***PLA-MMT/BN***), PLA doped with ZB adsorbed MMT (***PLA-MMT/ZB***), PLA doped with PBA adsorbed MMT (***PLA-MMT/PBA***), aiming to monitor the differences between modified and unmodified clay compound. The impact of B addition in the morphology of scaffolds and its effect on NHDF cells was restrained in previous groups due to the commanding influence of OMMT on cells. Identical to the prior fibrous scaffold groups, B compounds were adsorbed onto unmodified MMT with a ratio of 3:1 w/w% before being doped into PLA matrix with a concentration of 4% w/v%. B adsorbed MMT

(MMT/Bs) were characterized through ATR-FTIR and TGA analysis. Then, the solutions were prepared for electrospinning and after the optimization process, the scaffolds were collected. The results are presented in this section. All characterization results of PLA and PLA-MMT scaffolds are used as a reference to compare the effect of B addition into the structure. As the next step, the antibacterial activity and cytotoxicity test of PLA, PLA-MMT, and PLA-MMT/B scaffolds were examined. Finally, the NHDF cells were seeded on scaffolds, and cell viability, adhesion behavior, and morphology were explored.

4.6.1. Characterization of MMT/B Nanoparticles

4.6.1.1. ATR-FTIR Analysis

ATR-FTIR spectra of BN, MMT and MMT/BN compound was given in Figure 4.20. The ATR-FTIR results of MMT/BN demonstrated an additional peak at near 780 and 1350 cm^{-1} that belongs to the stretching vibration of B–N and the bending vibration of B–N–B, respectively. As there was no additional peak nor any changes at the characteristic peaks of BN and MMT, it was assumed that BN was physically absorbed on the surface of the clay mineral (Figure 4.20).

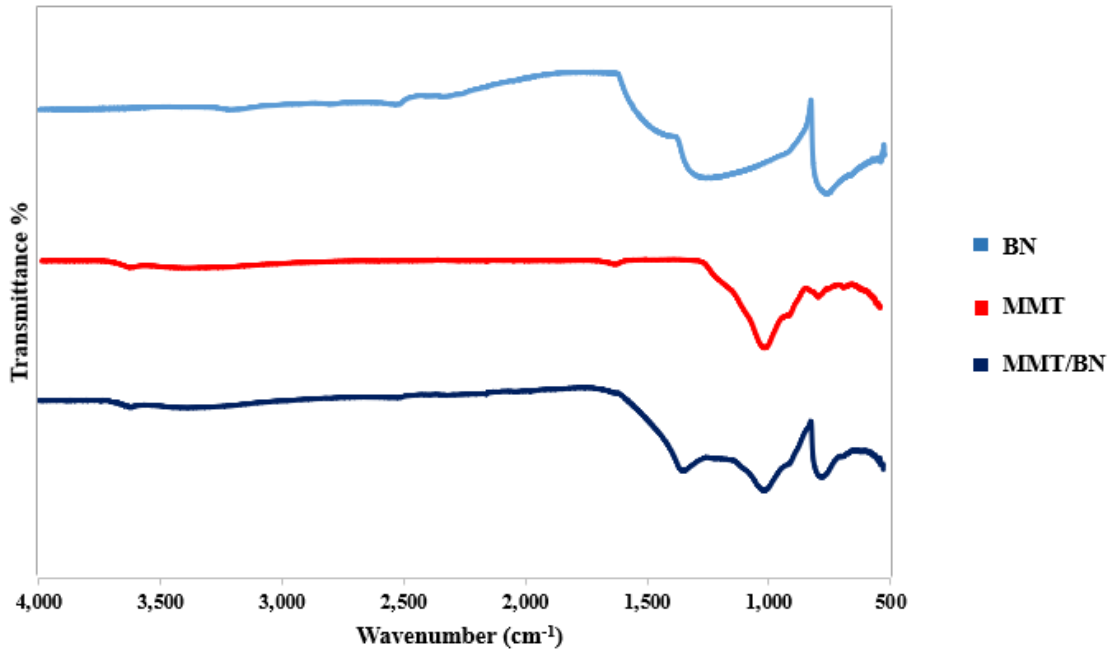

Figure 4.19. ATR-FTIR spectra of MMT, BN and MMT/BN nanoparticles.

The additional peaks in the range of 1414 and 1293 cm^{-1} (asymmetric vibration of the three-coordinate $B_{(3)}$-O), the adoption peak at 1161 cm^{-1} (asymmetric vibration of the $B_{(4)}$-O) and peaks at 792 and 749 cm^{-1} (symmetric vibration of $B_{(4)}$-O and rocking vibrations of $B(OH)_4)^-$) in the FTIR spectrum of the MMT/ZB, verified the attendance of ZB while maintaining the characteristic peaks of MMT in the structure of MMT/ZB compound (Figure 4.21).

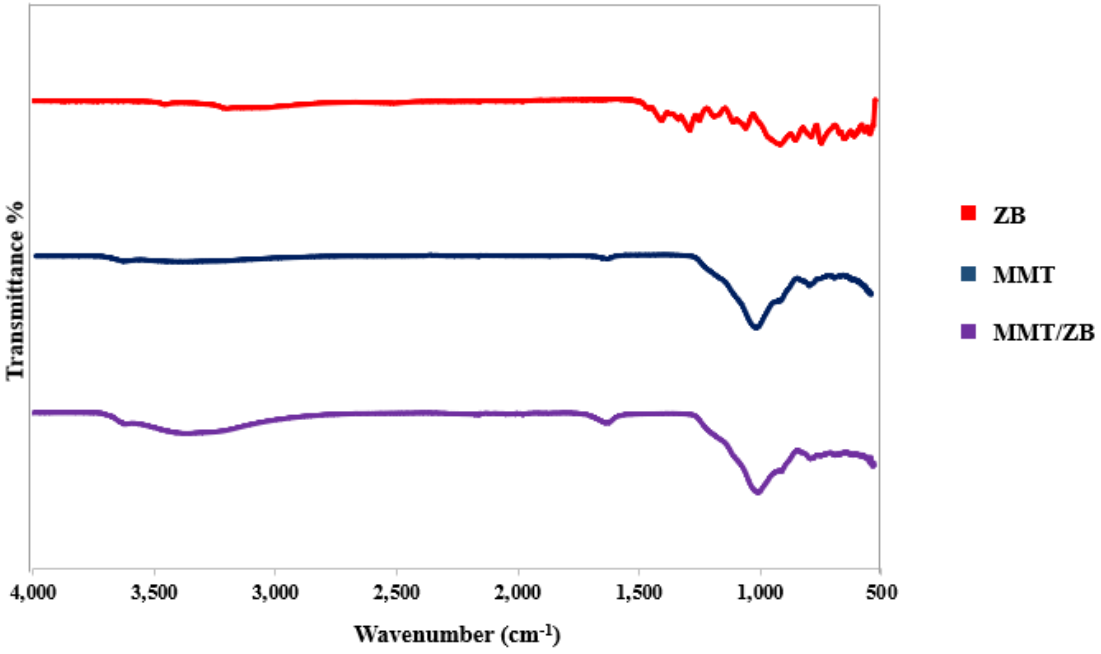

Figure 4.20. ATR-FTIR spectra of MMT, ZB and MMT/ZB nanoparticles.

The PBA compound tends to form a reversible bond with diol/polyol compounds. The presence of OH groups on MMT layers provides the opportunity for PBA to chemically bond with the OH groups of the MMT. The FTIR spectrum of MMT/PBA revealed intercalary peaks at 1410, 1465, 1293, and 597 cm^{-1} that are ascribed to the B–O–C, stretching vibration regarding C–C of the aromatic group, vibrations of the phenyl group, and bending vibration C–B band respectively. Moreover, the peak intensity at 1632 cm^{-1} increased due to the stretching vibration of the C-C aromatic group, and the shoulder peak near the 1100 cm^{-1} ascribed to the C-B stretching vibration was further evidence of PBA presence in the compound. However, the peak at 1023 cm^{-1} corresponded to the stretching vibrations of B–O–H was not observed at MMT/PBA compound which is due to the chemical bonding between MMT and PBA (Figure 4.22).

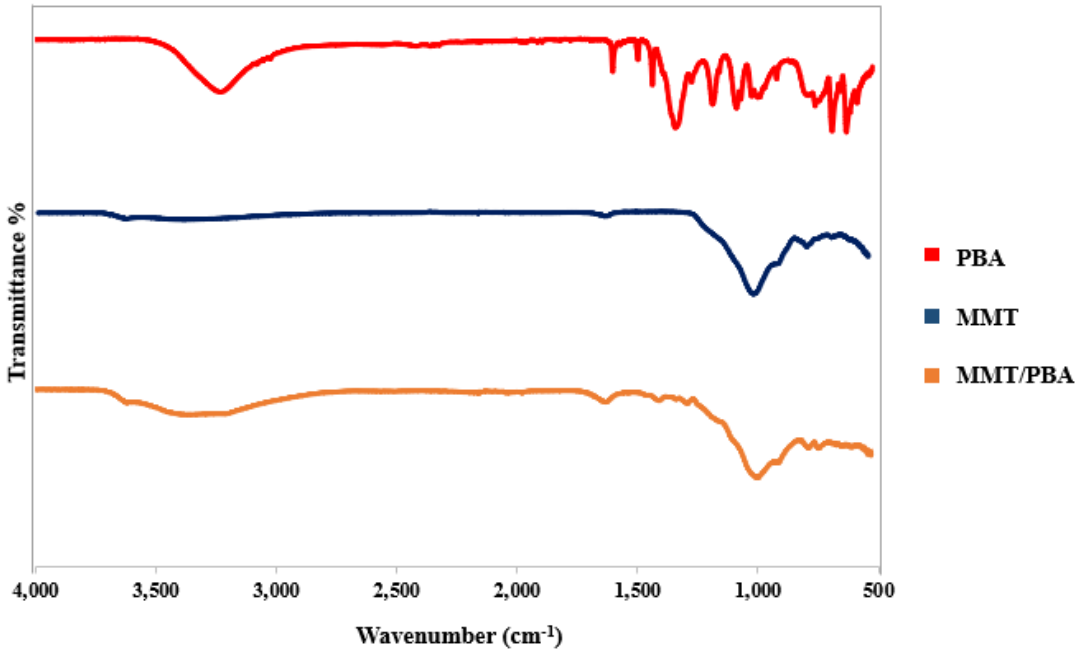

Figure 4.21. ATR-FTIR spectra of MMT, PBA and MMT/PBA nanoparticles.

4.6.1.2. TGA

Based on the result given in Figure 4.23., the thermal decomposition of MTT indicated two major mass loss regions in different temperatures. In the first step, the overall water content of MMT (water present in MMT crystallites, the water between the layers, and total water spheres around hydrated interlayer cations) was lost which occurred at relatively low temperatures (onset thermal degradation of 37°C). The second step involved dehydroxylation of MMT, which occurred between temperatures of 400 - 600°C (Qiu et al. 2020; Xie et al. 2001). The TGA results of MMT/BN exhibited a two-step thermal degradation behavior with similar temperature legions as MMT. However, the difference between MMT and MMT/BN was the overall weight loss amount of the compounds. The MMT/BN lost approximately 5% of its initial weight up to 800 °C whereas the overall weight loss of the MMT was 9% of its initial weight. The addition of the BN and its thermal stability increased the excessive residue amount of the MMT/BN compound.

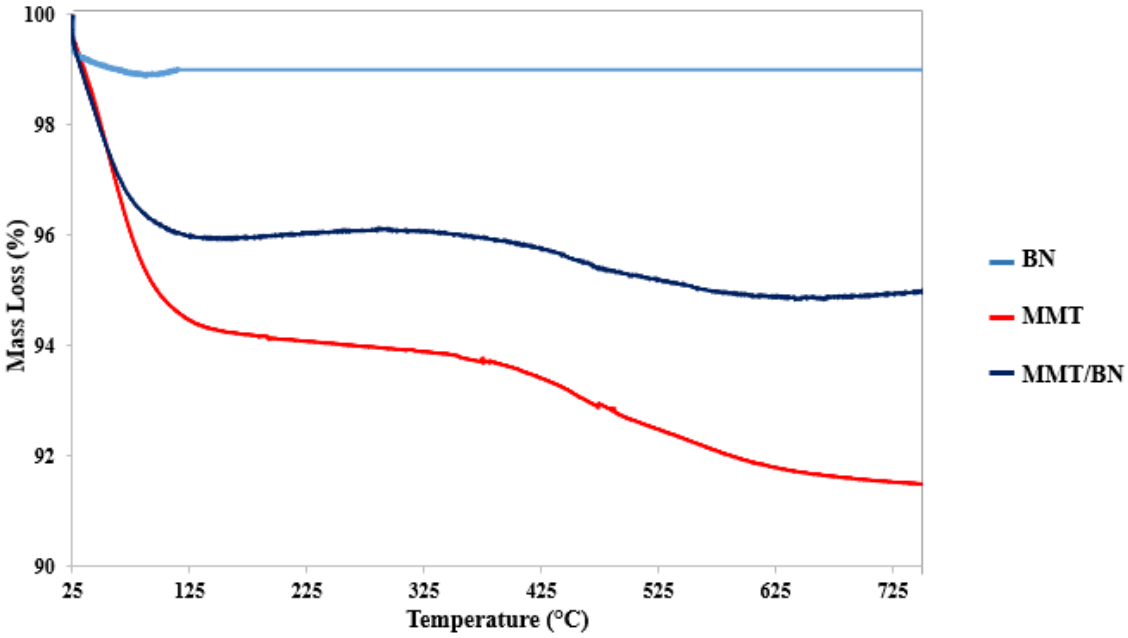

Figure 4.22. TGA mass loss curves of MMT, BN and MMT/BN nanoparticles.

The first step of thermal decomposition of MMT/ZB occurred at the same temperature regions as MMT regarding the elimination of water. The second stage is attributed to thermal decomposition of ZB, where zinc oxide and boric acid are formed and the compound lost 3% of its initial weight at 344 °C. The mass loss due to the decomposition of dehydroxylation of the MMT was not observed when ZB was present. The decomposition of hydrated ZB promotes the formation of a protective and vitreous char layer that acts as a thermal insulator, protecting the underlying substrate (MMT in this case) from heat (Cheng et al. 2020). The formation of a protective char layer may have prevented further decomposition of MMT (Figure 4.24.).

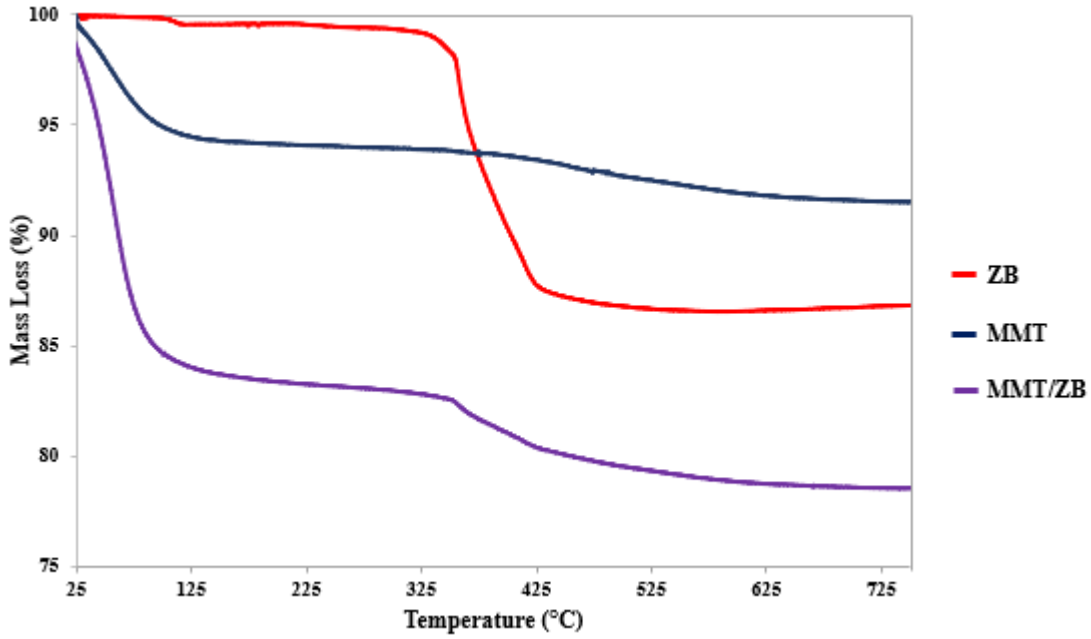

Figure 4.23. TGA mass loss curves of MMT, ZB and MMT/ZB nanoparticles.

According to the TGA results of MMT/PBA given in Figure 4.25. the weight loss of the compound occurred in two steps. The first step was due to the elimination of water that happens at 44°C and the compound lost approximately 16% of its initial weight. Generation of the water molecules during the formation of the phenylboronic ester-MMT bond increased the overall water amount of the compound. According to the TGA curve of the MMT/PBA, the second step of thermal degradation of MMT/PBA starts at temperatures around 370 ˚C and continues until 600 ˚C, and the compound loses approximately 3% of its initial weight, which is attributed to the thermal decomposition of PBA. The decompositions of PBA resulted in the appearance of a highly stable coal sheet slowing the second step of thermal degradation of the neat MMT.

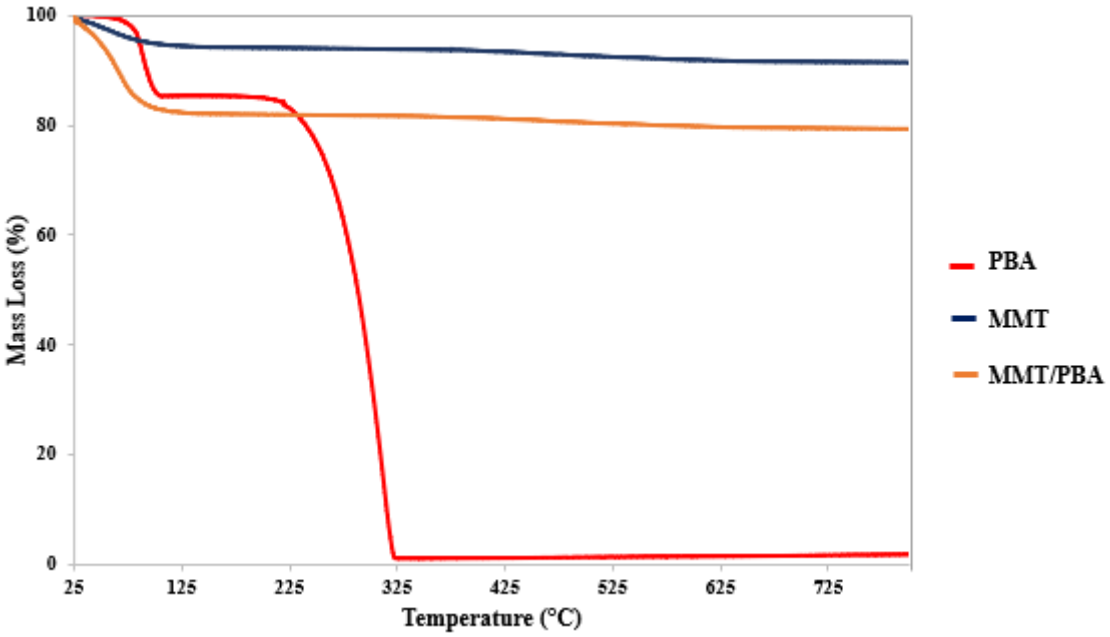

Figure 4.24. TGA mass loss curves of MMT, PBA and MMT/PBA nanoparticles.

4.6.2. Characterization of PLA-MMT/B Composites

4.6.2.1. ATR-FTIR Analysis

Figure 4.26. showed the FTIR spectra of the PLA, PLA-MMT, and PLA-MMT/Bs. All the characteristic peaks of PLA at 1750 cm^{-1} (C=O stretching), 1180-1043 cm^{-1} (peaks of C–O group), 2995, 2947, 1455, 1361 cm^{-1} (asymmetric and symmetric stretching and bending vibrations of the $–CH_3$), 1382 cm^{-1} (the bending vibration of C-H), and 868 cm^{-1} (stretching vibration of C-C single bond) was observed in FTIR spectra of all groups. Similar to the results of previous groups containing modified clay compound, FTIR results of all groups of scaffolds showed characteristic peaks of the PLA, without any significant change in peak positions. In order to get a clue about the chemical composition of the fibrous scaffolds, EDX analysis was carried out.

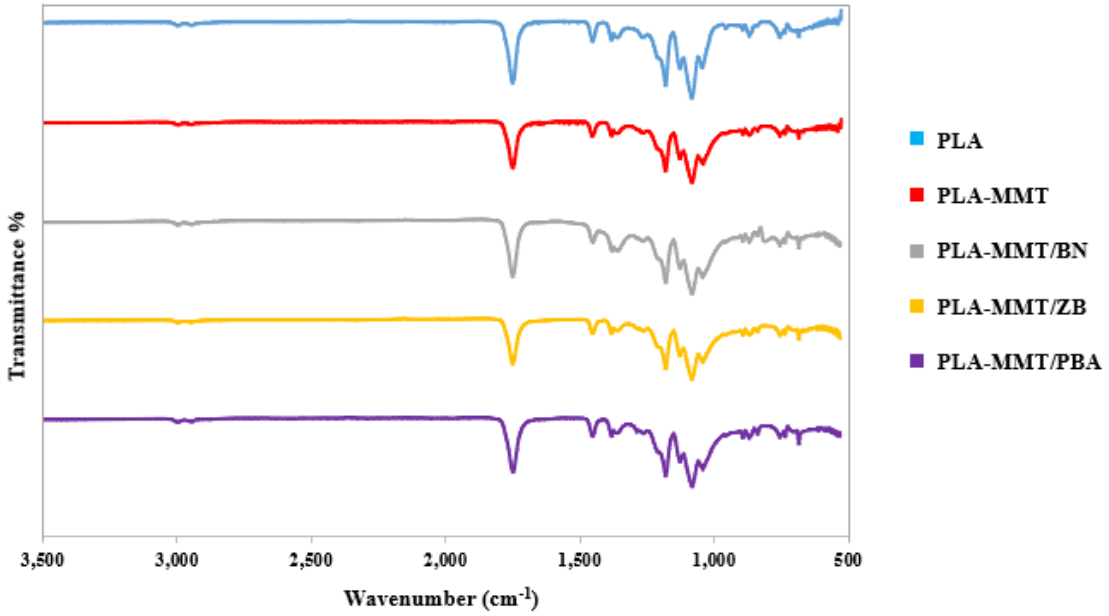

Figure 4.25. ATR-FTIR spectra of PLA and PLA-based hybrid composites of MMT obtained by electrospinning method.

4.6.2.2. EDX Analysis

The EDX spectra of fibrous scaffolds were given in Table 4.5.

Table 4.5. Summary of weigh percentages of each element in the structure of PLA, PLA-MMT, and PLA-MMT/B hybrid composites acquired from EDX spectra

Groups	C (%)	O (%)	Si (%)	Al (%)	B (%)	N (%)	Zn (%)
PLA	57.1	16.2	-	-	-	-	-
PLA-MMT	67.2	27.0	4.5	0.8	-	-	-
PLA-MMT/BN	52.2	24.0	1.2	0.3	18.2	3.9	-
PLA-MMT/ZB	57.0	22.5	0.5	1.0	18.7	-	0.2
PLA-MMT/PBA	63.5	15.7	0.6	0.1	19.9	-	-

By the addition of MMT to the polymeric matrix 0.8 and 4.5 weight amount (%) of aluminum and silicon were added to the structure of composite, respectively. All fibrous structures with a B compound in their structure demonstrated ~18% weight amount of the

B in their EDX spectra. In addition, for PLA-MMT/BN 3.9% nitrogen, and PLA-MMT/ZB, 0.2% zinc was present as well which proved the presence of B compounds in the fibrous structure of the composites. In PLA-MMT/PBA, the amount of carbon increased further due to the presence of carbon atoms in the PBA structure.

4.6.2.3. SEM Analysis

The morphological features of neat PLA and PLA composites with MMT, MMT/BN, MMT/ZB, and MMT/PBA fibers are depicted in Figure 4.27. As was explained before, the PLA nanofibers revealed bead-free, smooth, and continuous morphology where the PLA-MMT nanofibers were non-homogenous with a standard deviation higher than the mean value, and fibers contained numerous pores in their structure. The PLA-MMT/B nanofibers exhibited relatively similar morphology to the PLA-MMT. The PLA-MMT/BN fibers showed a porous structure. However, the fiber structure of the PLA-MMT/ZB and PLA-MMT/PBA nanofibers demonstrated grooved structures. This phenomenon occurred due to the difference in the electrospinning process parameters. The flow rate and needle-collector distance for PLA-MMT/ZB and PLA-MMT/PBA were relatively higher than PLA-MMT and PLA-MMT/BN groups. A volatile solvent can promote void formation because of its fast evaporation rate and phase separation. The higher flow rate and farther distance allow the jet to stay wet long enough to stretch, leading to the elongation of voids into grooved texture (Liu et al. 2015).

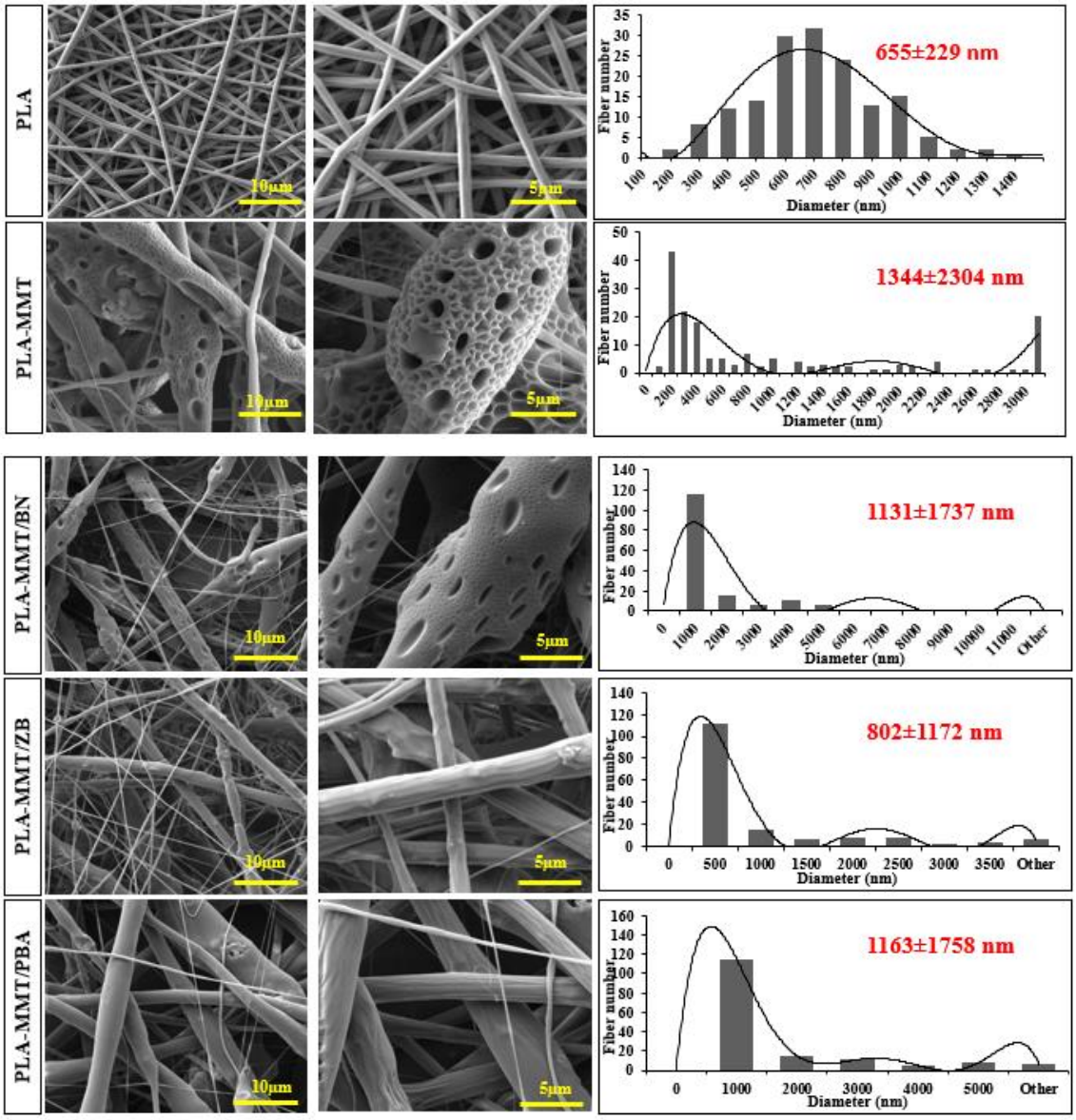

Figure 4.26. SEM images of PLA and PLA-based hybrid composites of MMT and B compounds at different magnifications with the optimized electrospinning conditions and diameter distribution graphs.

4.6.2.4. DSC Analysis

The differential scanning calorimetry analysis was carried out to determine glass transition temperature (T_g), melting temperature (T_m), and degree of crystallinity (%) of nanofibers, and the results were given in Table 4.6.

Table 4.6. The summary of differential scanning calorimetry results of PLA, and PLA-based hybrid composites of MMT and B compounds.

	Glass transition temperature (˚C)	**Melting temperature (˚C)**	**Crystallinity (%)**
PLA	60.93	175.52	48.00
PLA-MMT	81.66	176.85	28.00
PLA-MMT/BN	84.37	177.27	12.00
PLA-MMT/ZB	87.44	177.41	16.00
PLA-MMT/PBA	85.96	176.95	14.00

The incorporation of B compounds into the PLA matrix enhanced the T_g and T_m to a higher temperature. The T_g values of hybrid composites of PLA-MMT/BN, PLA-MMT/ZB, and PLA-MMT/PBA were 84.37, 87.44, and 85.96˚C, respectively, which were in higher temperatures when compared to neat PLA and PLA-MMT composite. The inclusion of fillers with high thermal stability and their interaction with the polymer matrix leads to the formation of heterophase nucleation, in which their nucleation is less affected by temperature. Furthermore, the B compounds restrict the migration of the PLA chains, which increases the T_m temperatures (Shen et al. 2020; Wang and Wen 2022). However, the degree of crystallinity decreased severely when B compounds were incorporated into the PLA matrix, which means more defect-ridden crystalline lamella, and irregularly shaped polymeric crystals were formed when MMT and B compounds were present. It is worth mentioning that the crystalline lamella formed in the presence of MMT/Bs were less ordered and defect ridden than OMMT/B because the reduction of the crystallinity % was more severe for the present group.

4.6.2.5. TGA

The thermal stability of scaffolds was investigated through TGA in the nitrogen atmosphere, and the results are given in Table 4.7.

Table 4.7. Summary of the thermogravimetric analysis for PLA, PLA-MMT and PLA-MMT/B hybrid composites

Groups	Mass loss I (%) / Onset temperature (˚C)	Mass loss II (%) / Onset temperature (˚C)
PLA	1.60 / 73.37	94.78 / 352.34
PLA-MMT	6.30 / 60.58	69.59 / 309.49
PLA-MMT/BN	6.03/57.86	62.48 / 307.30
PLA-MMT/ZB	8.92/58.85	71.85 / 292.45
PLA-MMT/PBA	10.78/60.03	73.22 / 309.97

For PLA-MMT/BN, PLA-MMT/ZB, and PLA-MMT/PBA a two-step thermal degradation trend was observed. In the case of PLA-MMT/BN and PLA-MMT/ZB, the onset degradation temperature of the first and second steps decreased, and the first step occurred at temperatures of 57 and 59 ˚C, and the second step occurred at temperatures of 307 and 292 ˚C, respectively. In contrast, the onset degradation temperature of PLA-MMT/PBA for both steps remained unchanged. However, the addition of BN increased the residual weight to 31.45% but the addition of ZB and PBA decreased the amount of residual to 19.30 and 16%, respectively. It can be concluded that the chemical bonding of PBA to MMT did not diminish the thermal degradation temperature of the composite, whereas the physical adsorption of BN and ZB decreased the decomposition temperatures to lower temperatures. Yet, BN improves the gas barrier properties of the matrix, which increases the thermal stability of the composite, and leads to further increment in the residual mass of the PLA-MMT/BN composite (Shen et al. 2020). The addition of BN did not affect the water amount present in the structure but the reduction in the onset degradation temperature of the first step suggested that adsorption of BN on MMT weakened the bonding of water molecules to the MMT. The same can be concluded in the case of ZB. However, the overall water content of PLA-MMT/ZB and PLA-MMT/PBA was higher than PLA-MMT (~ 9% and ~ 11%, respectively). This might be due to moister present in the hydrophilic structure of ZB and PBA and the water molecules generated during the chemical bonding of PBA and MMT. As explained in the previous section, the thermal degradation of PBA occurs at 272 ˚C. The reduction in the

excess residual mass of PLA-MMT/PBA in comparison to the other groups containing MMT and MMT/B compounds is due to the decomposition of PBA.

4.6.2.6. Water Uptake Capacity Test

The water uptake capacity of pristine polymer and its composites with MMT and MMT/B was measured in PBS, and the outcomes are illustrated in Figure 4.28.

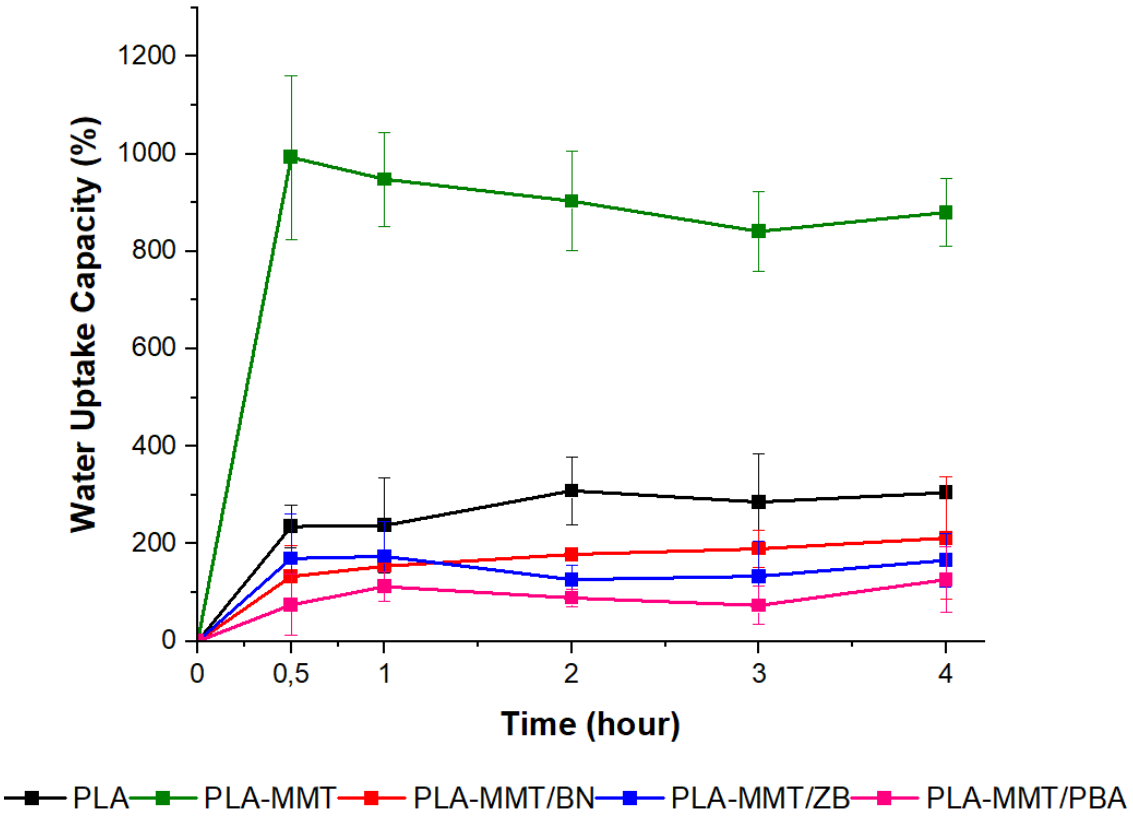

Figure 4.27. The water uptake capacities test results for PLA and PLA-based hybid composites of MMT and B compounds.

The water absorption of all samples increased by increasing submerging time and then reached equilibrium. It was observed previously that the inclusion of MMT clay improved the water uptake of the PLA-MMT composite due to the hydrophilic nature of MMT. Interestingly, the incorporation of B compounds to the composite decreased the water uptake of the composite to lower values than neat PLA. The affinity of MMT to water

depends on various factors such as the concentration of MMT, the nature of the interlayer cations, and layer structure and charge of MMT mineral (Caccamo et al. 2020; Chiou and Rutherford 1997). The concentration of MMT in PLA-MMT and PLA-MMT/B composites was 4% and 3% w/v, respectively. As the interlayer cations were unchanged for all samples, it can be assumed that the reduction of water affinity was associated with the lower concentration of MMT and the change in the charge and energy of the layers due to electrostatic and chemical absorption of the B compounds. It can be also assumed that in the conventional PLA-MMT/B composites, the presence of the B compound in the composite structure limited the penetration of the H_2O molecule in the interlayer space of the MMT and prevent the expansion of the layers and reduce the swelling property of the composite. Further evidence was provided by the biodegradability test, showing that B compounds limited the water penetration into the structure of hybrid composites.

4.6.2.7. Biodegradability Test

To evaluate the biodegradation behavior of the nanofibers before and after doping with MMT and MMT/B compounds, scaffolds were immersed in PBS that contained lysozyme and the mass loss of the nanofibers was weight at certain intervals.

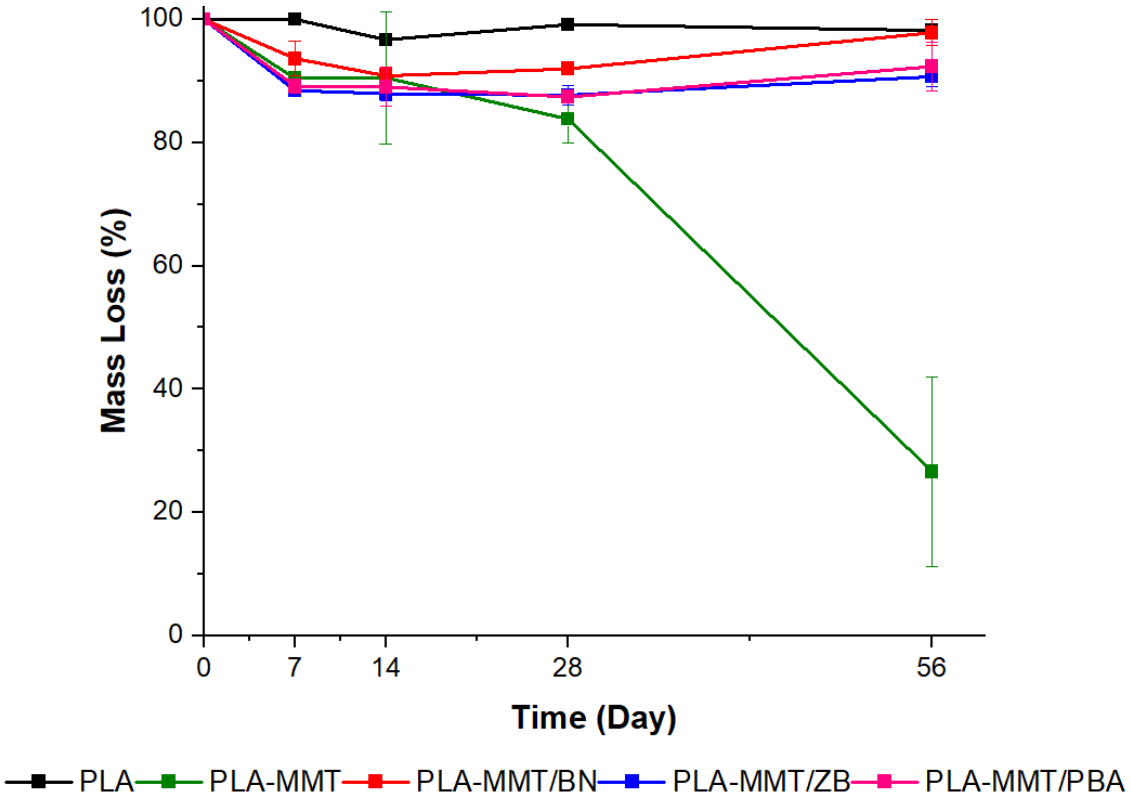

Figure 4.28. Enzymatic degradation results of PLA, PLA-MMT composite and PLA-MMT/B hybrid composites

Based on the results that were given in Figure 4.29. the degradation rate increased by corporation of MMT to the PLA matrix. The total mass loss after 28 days for PLA-MMT/BN, PLA-MMT/ZB, and PLA-MMT/PBA nanofibers were calculated to be 8.01±0.75%, 12.30±1.53%, 12.58±0.48%, respectively and the weight loss remained unchanged afterward. The results of biodegradability were constant with the results of water uptake capacity, demonstrating the shielding effect of B compounds against water diffusion, resulting in a reduced degradation rate and water uptake capacity. In addition to the proposed explanation, terminal hydroxyl groups of MMT are considered to be one of the main sites of the compound that increases the water uptake and accelerates the degradation process. The formation of phenyl boronate ester bonds occupied the hydroxyl groups of MMT; It is reasonable to assume that physical absorption of BN and ZB particles act as a barrier, preventing the interaction of H_2O and hydroxyl groups that led to the reduction of hydrolytic degradation of nanofibers.

In conclusion, the hydrolytic degradation of the neat PLA was improved by introducing a highly hydrophilic MMT compound. On contrary, the addition of B compounds decreased the biodegradability of the composites due to the shielding effect of B compounds on the penetration of water molecules and the resistance of the mentioned compound against hydrolytic and enzymatic degradation.

4.6.2.8. Mechanical Test

The scaffolds were mechanically characterized through the tensile test (Table 4.8.). As was discussed before, the tensile strength, toughness, and elastic modulous were negatively affected by the addition of MMT compound to PLA matrix.

In the case of the composites containing B in their structure, the results reveal a further decrease in tensile strength, elastic modulus, and breaking strain. This leads to the conclusion that the addition of the B compound decreased the molecular compatibilization between polymer and clay so that the composite materials were not able to transfer the applied stress evenly through the fiber which led to lower mechanical properties. Among the composites containing the B compound, PLA-MMT/PBA demonstrated better tensile strength, elastic modulus, and breaking strain values in comparison to PLA-MMT/BN and PLA-MMT/ZB. The results demonstrated the commanding effect of MMT and B compounds on the mechanical durability of the resulting composites, meaning the mentioned characteristic can be altered with the doping amount of MMT and B compounds.

Table 4.8. Mechanical characterization of PLA, PLA-MMT and PLA-MMT/B fibrous scaffolds.

Groups	Tensile Strength (MPa)	Breaking strain (%)	Toughness (MPa)	Elastic modulus (MPa)
PLA	14.95±1.41	132.87±12.72	3.92±1.06	591.10±183.72
PLA-MMT	4.52±0.91	147.88±10.35	1.89±0.81	88.20±6.26
PLA-MMT/BN	0.26±0.04	111.66±2.81	0.04±0.00	5.47±1.18
PLA-MMT/ZB	0.37±0.00	116.07±1.97	0.05±0.01	10.63±4.37
PLA-MMT/PBA	0.31±0.02	127.76±8.08	0.04±0.01	12.70±3.14

4.6.3. Antibacterial Study

The antibacterial assay was performed on PLA-MMT and PLA-MMT/B scaffolds against pathogenic *E. coli* and *S. aureus* bacteria through the agar disk diffusion (ADD) and optical density (OD) methods according to the Clinical & Laboratory Standards Institute (CLSI) standards.

The outcomes of ADD assay were elucidated in Figure 4.30. An inhibition zone of ~10 mm was formed around PLA-MMT/ZB, and PLA-MMT/PBA against *S. aureus*, however, no clear zone was formed for *E. coli*. PLA-MMT fails to demonstrate any clear zone formation for both bacteria species. The OD results of all groups containing MMT and B compounds in their structure exhibited toxicity toward the growth of both bacteria strains during 24 h. The inhibition was more pronounced for PLA-MMT/ZB scaffolds on the growth of both groups of bacteria. In contrast, the PLA-MMT/BN inhibited the growth of both bacteria strains but inhibited the growth of *E. coli* more significantly. The fraction of viable *E. coli* and *S. aureus* cells lessened for PLA-MMT/PBA group equally. In the case of scaffolds with the B compounds, BN nanoparticles are known for their similarity to graphene and there are various mechanisms suggested for the antibacterial effect of these materials. Preventing transmembrane transport of nutrients by wrapping bacterial cells, tearing the cellular envelope with sharp exposed edges, and causing oxidative stress are examples of the suggested mechanisms. Although the exact molecular

mechanism is not fully explained, tearing the cell membrane of bacteria apart by exposed sharp edges is a hypothesis that is mostly accepted. (Pandit et al. 2019).

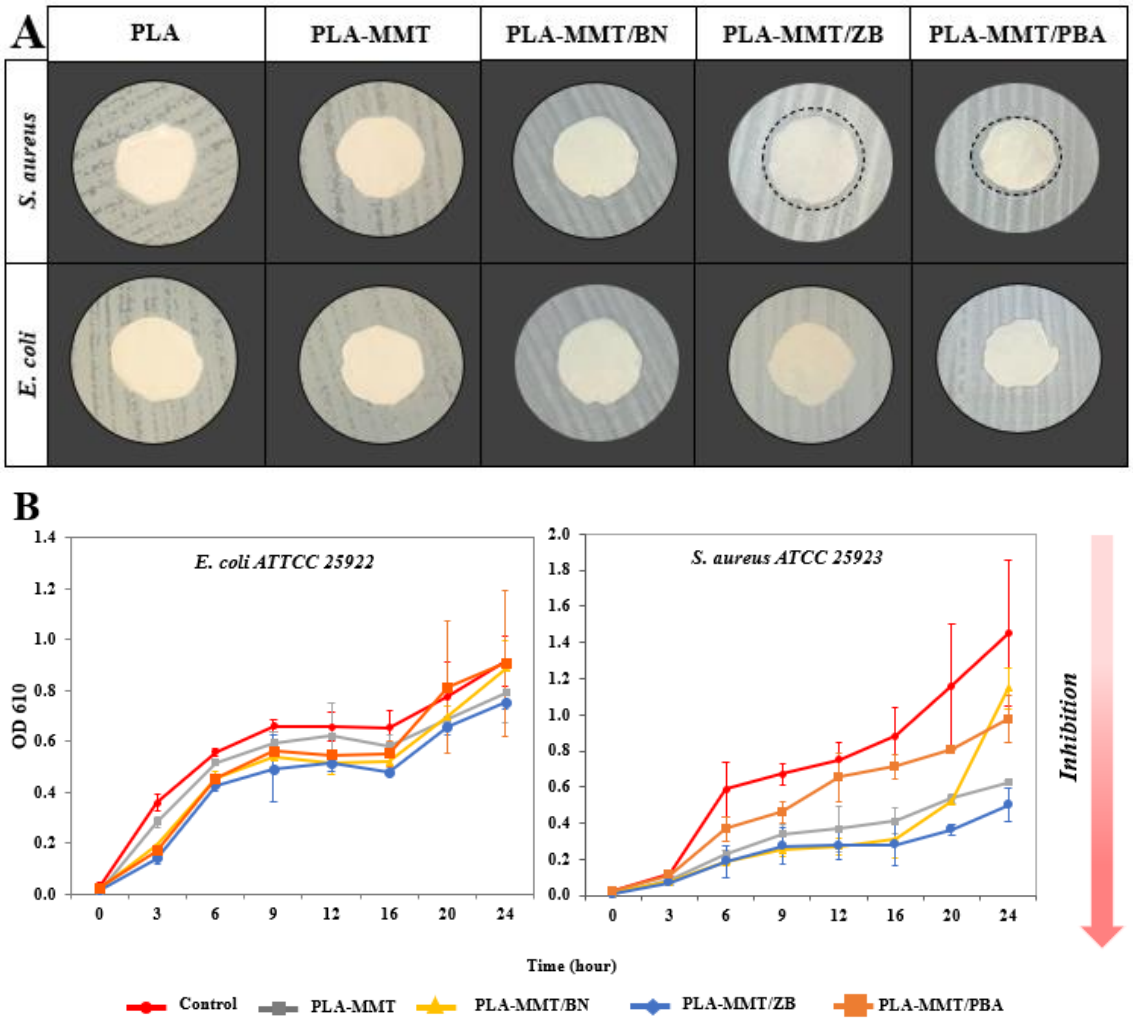

Figure 4.29. Antibacterial activity studies of MMT and B-containing fibrous scaffolds against pathogenic gram-negative *E. coli* and gram-positive *S. aureus* bacteria A) The disc diffusion method B) The optical density method

The antibacterial properties of materials containing Zn^{2+} are well known and there are several pass ways proposed for Zn^{2+} antibacterial effect, including Zn^{2+} effect to inhibit bacterial enzymes (Gajjar et al. 2009), penetrating the bacterial cell membrane and causing oxidative stress by generating reactive oxygen species (ROS) (Padmavathy and Vijayaraghavan 2008), and directly effecting cell membrane permeability and causing oxidative stress (Xie et al. 2011).

The inhibitory impact of the PBA compound against bacterial growth is related to the compound's capacity to form covalent bonds with glycoproteins of the bacterial cell as they contain diol groups, which interfere with the functions of pathogens' enzymes. (Adamczyk-Woźniak and Sporzyński 2020; Halbus et al. 2019). As explained before, PBA was chemically adsorbed on MMT through the terminal –OH groups. However, the newly formed covalent bond is reversible, depending on many variables, such as the concentration and structure of the compound containing diol groups. (Adamczyk-Woźniak and Sporzyński 2020). The concentration of the bacterial cells in the media increases gradually, so it can be assumed that PBA would bond with diol groups of glycoproteins of bacterial cells and demonstrate an antibacterial behavior. The exact molecular mechanism of B compounds for their antibacterial effect was not investigated in this study, however, results indicated the bacteriostatic properties of B-containing composites.

4.6.4. Cytotoxicity Test

The first step for deciding the biosafety of novel materials is the cell viability test since cell growth and survival are instantly influencing the amount of DNA, total number of proteins, and metabolic activity. (Kıvanç et al. 2018).

To be certain of the B compound's effect on the NHDFs, the cytotoxicity test was conducted for all the scaffolds and cells seeded on TCPS was used as a control group. The viability of the cells was monitored for 3 days for 100% extract of the scaffolds (Figure 4.31.). The results demonstrated that during the cytotoxicity test, the viability of NHDFs was higher than 90% for all groups of scaffolds. The cell viability continues to increase up to three days of culture, but no significant difference was detected between the experimental groups. Thus, the B compounds in the structure of the composites have no toxic effect on the proliferation of NHDF cells.

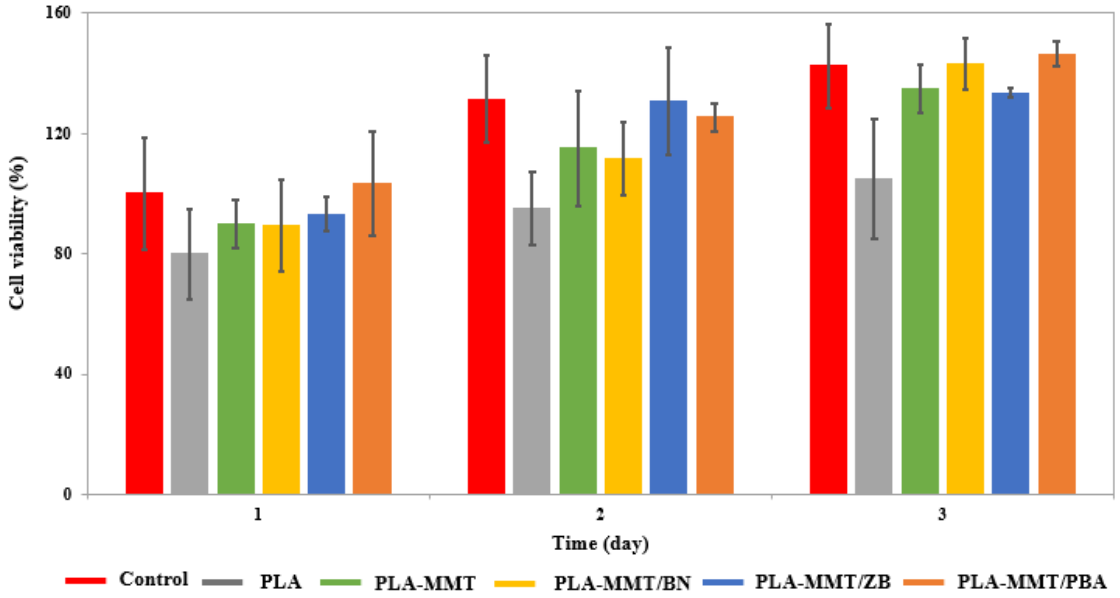

Figure 4.30. Cytotoxicity results of PLA, PLA-MMT, and PLA-MMT/B nanofibrous scaffolds for 3 days at 100% extract without dilution. Control indicates that cells were cultured on TCPS

4.6.5. *In-vitro* Cell Culture Studies

4.6.5.1. Cell Viability Test

After preliminary cytotoxicity test, *in-vitro* cell culture assay was conducted and PLA was used as control group. A dressing should provide a favorable microenvironment to protect the tissue from secondary damage, improve adhesion, migration, and proliferation of the cells in the wound site (Chen et al. 2022).

Viability and proliferation of NHDF on PLA and its composites were followed by MTT assay and the results were shown in Figure 4.32.

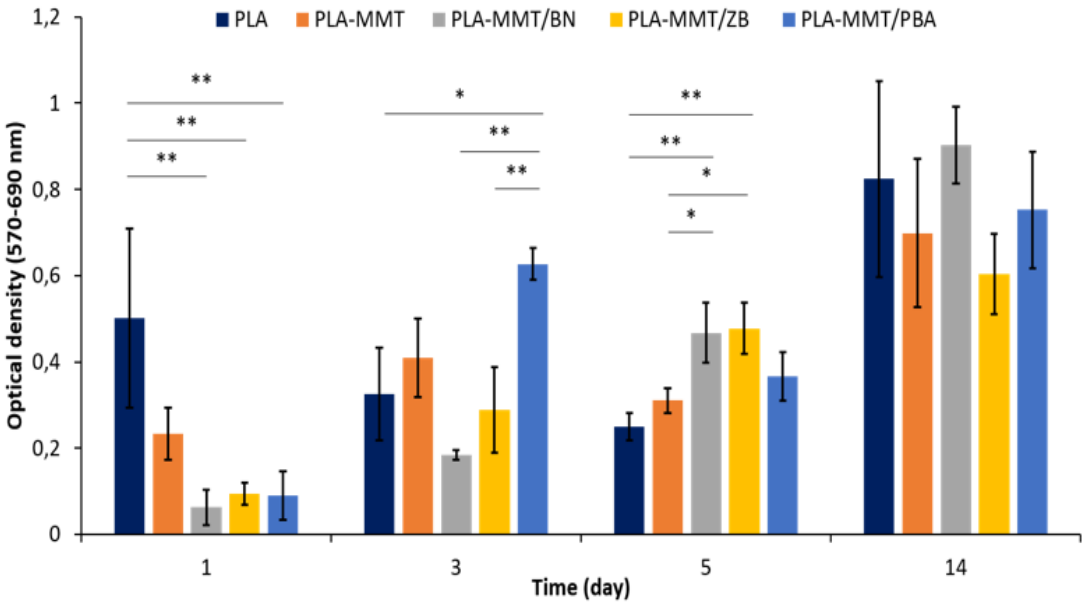

Figure 4.31. The MTT results of NHDF cells on the PLA-based scaffolds. Mitochondrial activities of cells increased in all groups during the cell culture but there was not statistically difference in cell viability among the groups at the end of 14th day. Statistically significant differences were observed between groups in the same analysis day: n = 3; $* p < 0.05$, $** p < 0.01$, $*** p < 0.001$, $**** p < 0.0001$.

In all types of scaffolds, optical densities increased gradually during 14 days of culture except for the PLA-MMT and PLA-MMT/PBA on the 5th day of culture that optical density decreased compared to 3rd day of culture, maybe differentiation mechanism was more dominant proliferation phase. It is well known that fibroblasts differentiate into myofibroblasts during the early stages of fibroblast growth. Myofibroblasts have a big role in the early stage of cutaneous wound healing to secrete a collagen matrix. (Jeong et al. 2013). So much so that a study showed the importance of boric acid dosage in myogenic differentiation (Wang et al. 2020). However, the highest optical density was observed on the 14th day for all groups. On the 3rd day of culture, cells seeded on the PLA-MMT/PBA scaffolds demonstrated the highest mitochondrial activity, which was significantly higher than neat PLA, PLA-MMT/BN, and PLA-MMT/ZB. On the 5th day of culture, cells seeded on both PLA-MMT/BN and PLA-MMT/ZB scaffolds indicated the highest mitochondrial activity that was significantly higher than PLA and PLA-MMT ($p < 0.01$). On the 14th day, the optical density of scaffolds containing BN compound was

higher than neat PLA and PLA-MMT however, the difference was not significant. These observations reflected the supportive effect of B compounds on the growth and proliferation of HDF on composite scaffolds.

4.6.5.2. SEM Analysis

Further investigation about cell adhesion was provided through SEM analysis. The images present in Figure 4.33. demonstrated well-spread cells on neat PLA, PLA-MMT, and PLA-MMT/PBA micro fibers, where a cell layer was formed on the scaffolds and a fibrillar ECM was observed. On contrary, PLA-MMT/BN and PLA-MMT/ZB scaffolds indicated fewer adhered cells on the scaffolds but the lamellipodia and filopodia observed on the surface of PLA-MMT/BN and PLA-MMT/ZB suggested that cells continue to adhere and spread.

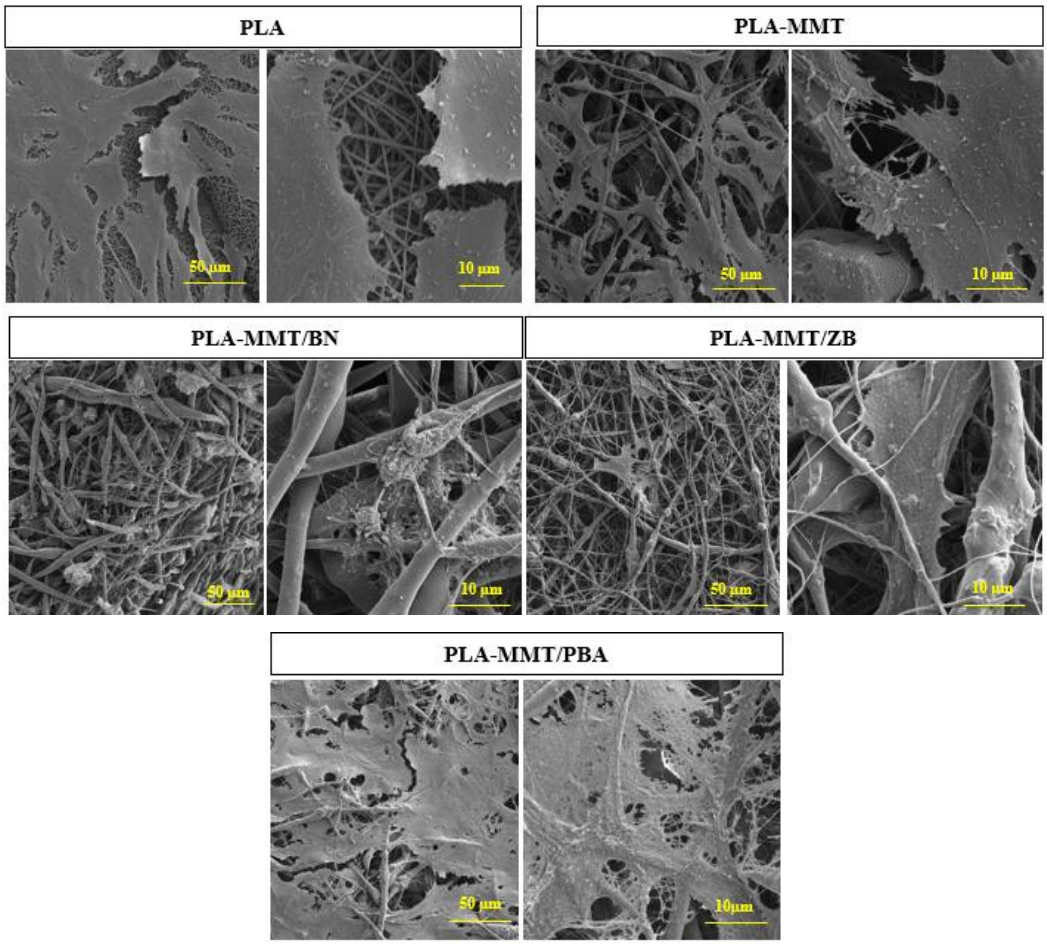

Figure 4.32. SEM images of NHDF cells seeded on PLA and PLA-based fibrous scaffolds of MMT and B compounds on the 5th day of culture

The difference in the cell adhesion behavior on different groups of scaffolds may be attributed to the difference in the nanotopography and mechanical properties of the scaffolds. Various researchers have reported that cells adhere and stretch better on the stiffer substrate and demonstrate a higher aspect ratio for the nucleus on 2D scaffolds (Jeong et al. 2013). The neat PLA demonstrated the highest stiffness among the scaffolds (highest elastic modulus) and PLA-MMT followed after the neat polymer. Among the PLA-MMT/Bs, PLA-MMT/PBA possessed the highest elastic modulus, which explains the cell adhesion behavior of NHDFs on scaffolds.

4.6.5.3. Live/Dead Staining

The cell viability and morphology of the NHDFs were evaluated by live/dead staining on the 5^{th} and 14^{th} day of culture. Based on the confocal microscopy images of NHDFs on the 5^{th} day, numerous viable cells were observed on the scaffold with healthy shape except for PLA-MMT/BN scaffold. Although viable cells were observed, the cell morphology was globular without extension. On the other hand, the images of the scaffolds on the 14^{th} day of culture demonstrate the viable cells with their natural stretched-out and spindle-like shape for all groups of scaffolds, especially PLA-MMT/BN which demonstrated the highest cell proliferation rate on MTT result.

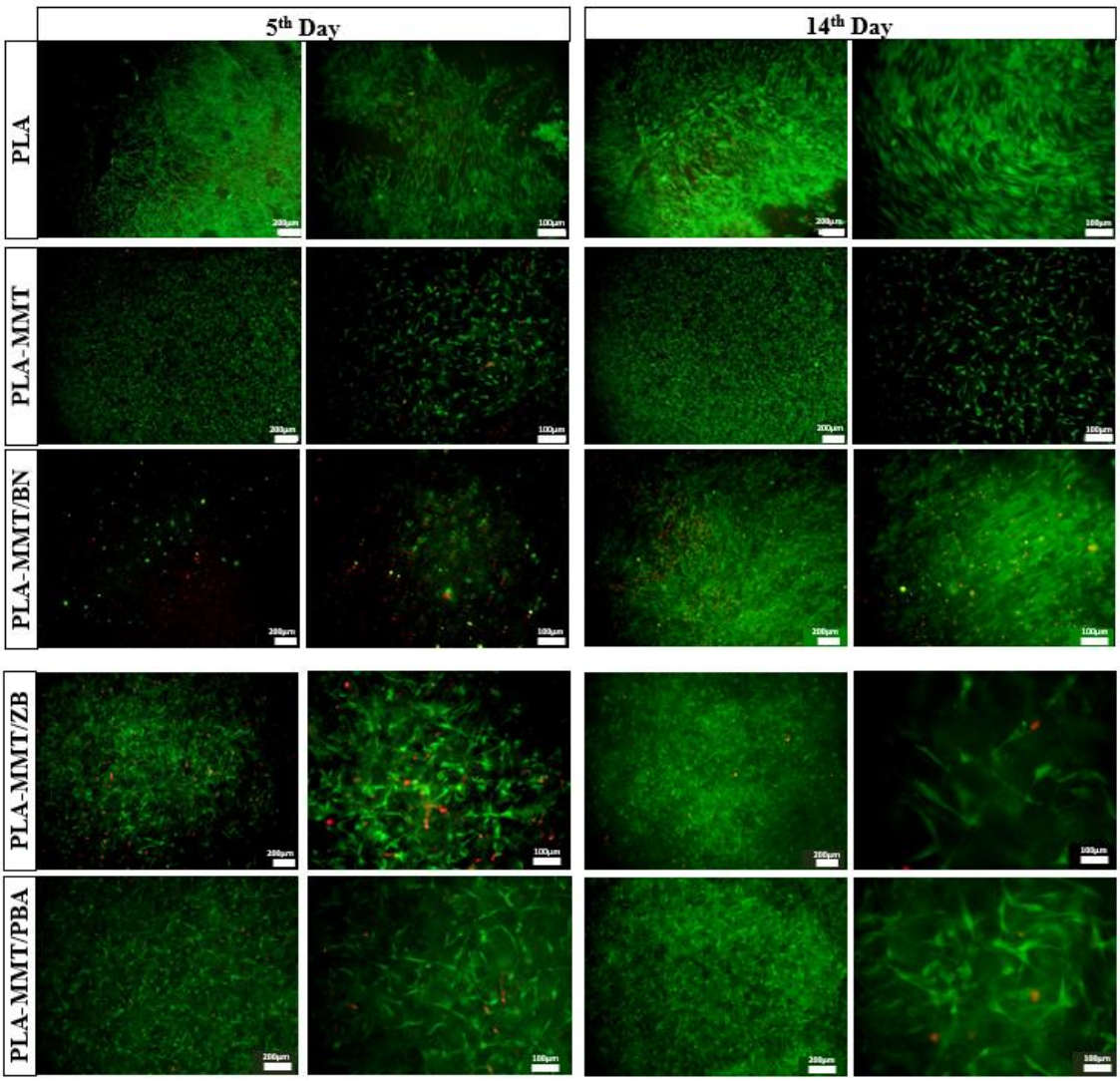

Figure 4.33. Live/dead staining images of NHDF cells on PLA and PLA-based fibrous scaffolds of MMT and B compounds on the 5th and 14th days of culture.

In conclusion, neat PLA scaffolds supported cell adhesion and proliferation due to the favorable mechanical properties. The inclusion of MMT into PLA did not hinder or increase cell viability and adhesion. Although the mechanical properties of the PLA-MMT composite were relatively lower than neat PLA, the presence of silicate layers in the nanofiber structure acts as focal adhesion sited for cells to adhere and spread (Gaharwar et al. 2012), which supported the cell growth on the scaffolds.

In the case of PLA-MMT/BN, some studies evaluated the dose-dependent effect of BN on NHDF cells demonstrating the favorable effect of BN on cell migration, proliferation, and filopodia formation (Şen et al. 2019). In our study, BN adsorbed onto MMT and later

doped in the PLA matrix. As a result, the loaded amount of BN (10 mg/mL in the fibrous scaffold) did not inhibit the cell growth, however, adhesion and spreading of the cells on the nanofibers took a longer time, which led to a slower proliferation rate of the cells on PLA-MMT/BN scaffold. It is worth mentioning that the highest mitochondrial activity belonged to PLA-MMT/BN scaffolds on the 5^{th} and 14^{th} days of the cell culture.

Similarly, it was reported that ZB particles have a dose-dependent effect on L929 fibroblast cells and no significant difference between zinc borate treated groups and non-zinc borate treated groups was observed (Aysel et al. 2019). The cells seeded on the PLA-MMT/ZB exhibited significantly higher cell viability on the 5^{th} day of culture according to the MTT results, which might be attributed to the release of Zn^{2+} which is an essential element for cell growth.

In the case of the PBA compound, it was reported that PBA selectively inhibits the proliferation of cancer and tumor cells, leaving healthy cells unaffected (Marasovic et al. 2017). In addition, it might accelerate cell attachment by binding to polysaccharides present on the cellular membrane. (Pan et al. 2014). Based on the MTT, SEM, and live/dead staining results, PLA-MMT/PBA was one of the best scaffolds that supported the cellular activity (e.g., attachment and proliferation) of NHDFs during the culture time. This can be because of unique features of PBA or wrinkled morphology of fibers similar to another study that was carried out with fibroblasts (Poyraz et al. 2022). Finally, the results of the cell culture study indicated that NHDFs grow and proliferate on the scaffolds while maintaining their healthy morphology.

5. CONCLUSION

In the present study, PLA-based micro/nanocomposites were fabricated by solvent-casting and electrospinning, utilizing MMT and B compounds. To reveal the difference between the modified and unmodified state of the MMT mineral, the B compounds were adsorbed on OMMT and neat MMT before being doped into the PLA matrix. The characteristic properties of fibrous scaffolds, as well as the impact of solvent-casting and electrospinning on the resulting micro/nanocomposites with the identical component were compared, observing the following results:

- The modification of the MMT reduced the CEC value of the clay mineral.
- After the adsorption process of the B compounds onto MMT and OMMT, the BN and ZB nanoparticles were physically absorbed on MMT and OMMT, while PBA nanoparticles were chemically bonded with clay minerals in both modified and unmodified states.
- The organomodification of MMT resulted in a better distribution of the OMMT particles in the polymeric matrix for both solvent-cast membranes and electrospun scaffolds. Neat MTT formed aggregates that were visible in the SEM micrographs of the membranes and increased the fiber diameter of the fibrous groups. However, the PLA-MMT fibrous scaffolds demonstrated porous structure, interestingly. After B addition, the OMMT/B particles dispersed homogeneously in the polymeric matrix of the membrane group and managed to remain nanosized in the fibrous group, indicating the formation of an intercalated type of nanocomposite. On the other hand, the MMT/B particles displayed similar behavior as MMT and formed fibers with uneven diameters and irregular shapes.
- The weight loss of electrospun fibers was more than membranes during 56 days of the biodegradation test. Although both MMT and OMMT improved the biodegradability of the PLA, it took some time for unmodified MMT to initiate the degradation process. The addition of B compounds hindered the biodegradation of the PLA-MMT/B and PLA-OMMT/B hybrid composites, but the inhibition was more pronounced for PLA-MMT/B micro composites.
- The mechanical durability of the membranes was fairly higher than fibrous groups, however, the absence of a dynamic environment during the composite production process resulted in the participation of clay and B-adsorbed clay minerals and the

formation of nonhomogeneous samples. The PLA-OMMT/ZB membranes indicated the lowest mechanical features among all groups. Yet, the modification of MMT led to the enhancement of mechanical characteristics in comparison to neat MMT, and the further addition of B compounds slightly increased the mechanical properties of PLA-OMMT/B nanofibers. In contrast, for PLA-MMT/B fibers, the existence of B reduced the mechanical features of hybrid composites.

- The water contact angle of membranes increased by the incorporation of clay in both states, but the addition of B compounds did not affect the water contact angle severely.
- Incorporation of thermally stable particles, such as MMT/OMMT and B compounds, enhanced the thermal properties of resulting micro/nanocomposites.
- The MMT and MMT/B particles decreased the crystallinity of PLA, but the OMMT nanoparticle increased the crystallinity. However, the OMMT/B incorporated hybrid composites indicated lower crystallinity.
- The water uptake capacity of composite improved when MMT was present in the structure, but the modification of MMT mineral decreased the water uptake capability of the PLA to values even lower than neat PLA. Boron adsorption reduced the water uptake capacity of PLA-MMT/B hybrid composites, however, in the case of PLA-OMMT/B nanocomposites, the presence of B compound increased the water uptake capacity.
- The modification of MMT led to the formation of scaffolds with high antibacterial activity against gram-positive *S. aureus bacteria*. Hybrid composites with ZB nanoparticles in their structure indicated the best antibacterial properties though, scaffolds with BN and PBA demonstrated antibacterial features as well.
- The PLA-OMMT scaffold inhibited the proliferation of NHDF cells due to the release of TMOD salt in the media in a long-term application, however, giving to the high antibacterial properties of mentioned scaffolds and non-toxicity of them in the short-term application, it was concluded that these scaffolds are suitable for short time applications. In contrast, PLA-MMT and PLA-MMT/B scaffolds were non-toxic under any condition and supported cell proliferation and adhesion, which makes them convenient for long-term applications. The PLA-MMT/PBA scaffolds showed the best results for *in-vitro* cell culture assay.

In conclusion, based on the results, electrospinning was a better method for fabricating tissue-engineered composite materials as potential dressings. The inclusion of clay nanoparticles (both on modified and unmodified states) and B compounds into the polymer matrix enhanced the bioactivity of the micro/nanocomposites, leading to the production of hybrid composites with multiple unique characteristics that can be improved even more in later studies. The organomodification of MMT nanoparticles not only changed the properties of clay minerals but also altered the prevailing properties of resulting composite and hybrid composites, where sometimes the properties of modified and unmodified clay-containing hybrid composites were exact opposites.

6. REFERENCES

Abniki, M., Shirkavand Hadavand, B., Najafi, F., Ghasedi, I., 2022. Synthesis of the effective flame retardant via modification of epoxy resin with phenylboronic acid. Journal of Macromolecular Science, Part A, 1-10.

Adamczyk-Woźniak, A., Sporzyński, A., 2020. The influence of ortho-substituents on the properties of phenylboronic acids. Journal of Organometallic Chemistry 913, 121202.

Adamczyk-Woźniak, A., Kaczorowska, E., Kredátusova, J., Madura, I., Marek, P.H., Matuszewska, A., Sporzyński, A., Uchman, M., 2018. Dehydration of ortho-, meta-and para-Alkoxy Phenylboronic Acids to their Corresponding Boroxines. European Journal of Inorganic Chemistry 2018(13), 1492-1498.

Adeli, H., Khorasani, M.T., Parvazinia, M., 2019. Wound dressing based on electrospun PVA/chitosan/starch nanofibrous mats: Fabrication, antibacterial and cytocompatibility evaluation and in vitro healing assay. International journal of biological macromolecules 122, 238-254.

Akdere, Ö.E., Shikhaliyeva, İ., Gümüşderelioğlu, M., 2019. Boron mediated 2D and 3D cultures of adipose derived mesenchymal stem cells. Cytotechnology 71(2), 611-622.

Annaidh, A.N., Bruyère, K., Destrade, M., Gilchrist, M.D., Otténio, M., 2012. Characterization of the anisotropic mechanical properties of excised human skin. Journal of the mechanical behavior of biomedical materials 5(1), 139-148.

Arida, I.A., Ali, I.H., Nasr, M., El-Sherbiny, I.M., 2021. Electrospun polymer-based nanofiber scaffolds for skin regeneration. Journal of Drug Delivery Science and Technology 64, 102623.

Arslan, A., Çakmak, S., Gümüşderelioğlu, M., 2018. Enhanced osteogenic activity with boron-doped nanohydroxyapatite-loaded poly (butylene adipate-co-terephthalate) fibrous 3D matrix. Artificial cells, nanomedicine, and biotechnology 46(sup2), 790-799.

Ayoob, R., Alhabill, F., Andritsch, T., Vaughan, A., 2018. Enhanced dielectric properties of polyethylene/hexagonal boron nitride nanocomposites. Journal of materials science 53(5), 3427-3442.

Aysel, U., CEYLAN, O., Boran, R., AYRİKCİL, S., Saraç, N., YİLMAZ, D., 2019. A new approach for prevention the oxidations and mutations: Zinc borate. Journal of Boron 4(4), 196-202.

Belaid, H., Nagarajan, S., Barou, C., Huon, V., Bares, J., Balme, S., Miele, P., Cornu, D., Cavaillès, V., Teyssier, C., 2020. Boron nitride based nanobiocomposites: design by 3D printing for bone tissue engineering. ACS Applied Bio Materials 3(4), 1865-1874.

Benderdour, M., Bui-Van, T., Dicko, A., Belleville, F., 1998. In vivo and in vitro effects of boron and boronated compounds. Journal of trace elements in medicine and biology 12(1), 2-7.

Bergaya, F., Lagaly, G., 2006. General introduction: clays, clay minerals, and clay science. Developments in clay science 1, 1-18.

Bernatchez, S.F., 2014. Care of peripheral venous catheter sites: advantages of transparent film dressings over tape and gauze. Journal of the Association for Vascular Access 19(4), 256-261.

Białek, M., Czauderna, M., Krajewska, K., Przybylski, W., 2019. Selected physiological effects of boron compounds for animals and humans. A review. Journal of Animal and Feed Sciences 28(4), 307-320.

Blacklow, S., Li, J., Freedman, B., Zeidi, M., Chen, C., Mooney, D., 2019. Bioinspired mechanically active adhesive dressings to accelerate wound closure. Science advances 5(7), eaaw3963.

Boddupalli, A., Zhu, L., Bratlie, K.M., 2016. Methods for Implant Acceptance and Wound Healing: Material Selection and Implant Location Modulate Macrophage and Fibroblast Phenotypes. Advanced Healthcare Materials 5(20), 2575-2594.

Bozoğlu, Ü.Ç., Kiremitçi, A.S., Yurtsever, M.Ç., Gumusderelioglu, M., Peek Dental Implants Coated with Boron-Doped Nano-Hydroxyapatites: Investigation of In-Vitro Osteogenic Activity.

Budak, E., 2018. Low temperature synthesis of hexagonal boron nitride by solid state reaction in the presence of lithium salts. Ceramics International 44(11), 13161-13164.

Caccamo, M.T., Mavilia, G., Mavilia, L., Lombardo, D., Magazù, S., 2020. Self-assembly processes in hydrated montmorillonite by FTIR investigations. Materials 13(5), 1100.

Calcagno, C., Mariani, C., Teixeira, S., Mauler, R., 2008. The role of the MMT on the morphology and mechanical properties of the PP/PET blends. Composites Science and Technology 68(10-11), 2193-2200.

Chen, B.-K., Shih, C.-C., Chen, A.F., 2012. Ductile PLA nanocomposites with improved thermal stability. Composites Part A: Applied Science and Manufacturing 43(12), 2289-2295.

Chen, B., 2004. Polymer–clay nanocomposites: an overview with emphasis on interaction mechanisms. British Ceramic Transactions 103(6), 241-249.

Chen, L., Zhang, D., Cheng, K., Li, W., Yu, Q., Wang, L., 2022. Photothermal-responsive fiber dressing with enhanced antibacterial activity and cell manipulation towards promoting wound-healing. Journal of Colloid and Interface Science 623, 21-33.

Cheng, X., Zhu, S., Pan, Y., Deng, Y., Shi, L., Gong, L., 2020. Fire retardancy and thermal behaviors of Cellulose nanofiber/zinc borate aerogel. Cellulose 27(13), 7463-7474.

Chiou, C.T., Rutherford, D.W., 1997. Effects of exchanged cation and layer charge on the sorption of water and EGME vapors on montmorillonite clays. Clays and Clay Minerals 45(6), 867-880.

Chong, W.J., Shen, S., Li, Y., Trinchi, A., Pejak, D., Kyratzis, I.L., Sola, A., Wen, C., 2022. Additive manufacturing of antibacterial PLA-ZnO nanocomposites: Benefits, limitations and open challenges. Journal of Materials Science & Technology 111, 120-151.

Colwell, A.S., Longaker, M.T., Lorenz, H.P., 2005. Mammalian fetal organ regeneration. Regenerative Medicine I, 83-100.

Cui, Y., Liu, X., Tian, Y., Ding, N., Wang, Z., 2012. Controllable synthesis of three kinds of zinc borates and flame retardant properties in polyurethane foam. Colloids and Surfaces A: Physicochemical and Engineering Aspects 414, 274-280.

Dąbrowska, A., Spano, F., Derler, S., Adlhart, C., Spencer, N.D., Rossi, R.M., 2018. The relationship between skin function, barrier properties, and body-dependent factors. Skin Research and Technology 24(2), 165-174.

Ebrahimi, F., Ramezani Dana, H., 2021. Poly lactic acid (PLA) polymers: From properties to biomedical applications. International Journal of Polymeric Materials and Polymeric Biomaterials, 1-14.

Eng, C.C., Ibrahim, N.A., Zainuddin, N., Ariffin, H., Yunus, W.M., Wan, Z., Then, Y.Y., Teh, C.C., 2013. Enhancement of mechanical and thermal properties of polylactic acid/polycaprolactone blends by hydrophilic nanoclay. Indian Journal of Materials Science 2013.

Ersan, A.C., Yildirim, M., Kipcak, A.S., Tugrul, N., 2016. A novel synthesis of zinc borates from a zinc oxide precursor via ultrasonic irradiation. Acta Chimica Slovenica 63(4), 881-890.

Fan, C., Xu, Q., Hao, R., Wang, C., Que, Y., Chen, Y., Yang, C., Chang, J., 2022. Multi-functional wound dressings based on silicate bioactive materials. Biomaterials 287, 121652.

Fang, Y., Zhu, X., Wang, N., Zhang, X., Yang, D., Nie, J., Ma, G., 2019. Biodegradable core-shell electrospun nanofibers based on PLA and γ-PGA for wound healing. European Polymer Journal 116, 30-37.

Fukushima, K., Tabuani, D., Dottori, M., Armentano, I., Kenny, J., Camino, G., 2011. Effect of temperature and nanoparticle type on hydrolytic degradation of poly (lactic acid) nanocomposites. Polymer degradation and stability 96(12), 2120-2129.

Gaharwar, A.K., Kishore, V., Rivera, C., Bullock, W., Wu, C.J., Akkus, O., Schmidt, G., 2012. Physically crosslinked nanocomposites from silicate-crosslinked PEO: mechanical properties and osteogenic differentiation of human mesenchymal stem cells. Macromolecular bioscience 12(6), 779-793.

Gajjar, P., Pettee, B., Britt, D.W., Huang, W., Johnson, W.P., Anderson, A.J., 2009. Antimicrobial activities of commercial nanoparticles against an environmental soil microbe, Pseudomonas putida KT2440. Journal of biological engineering 3(1), 1-13.

Ganguly, S., Dana, K., Ghatak, S., 2010. Thermogravimetric study of n-alkylammonium-intercalated montmorillonites of different cation exchange capacity. Journal of Thermal Analysis and Calorimetry 100(1), 71-78.

Gaskell, E.E., Hamilton, A.R., 2014. Antimicrobial clay-based materials for wound care. Future medicinal chemistry 6(6), 641-655.

Ghadiri, M., Chrzanowski, W., Rohanizadeh, R., 2015. Biomedical applications of cationic clay minerals. RSC advances 5(37), 29467-29481.

Ghaemi, N., Madaeni, S.S., Alizadeh, A., Rajabi, H., Daraei, P., 2011. Preparation, characterization and performance of polyethersulfone/organically modified montmorillonite nanocomposite membranes in removal of pesticides. Journal of Membrane Science 382(1-2), 135-147.

Ghobril, C., Grinstaff, M., 2015. The chemistry and engineering of polymeric hydrogel adhesives for wound closure: a tutorial. Chemical Society Reviews 44(7), 1820-1835.

Golafshan, N., Rezahasani, R., Esfahani, M.T., Kharaziha, M., Khorasani, S., 2017. Nanohybrid hydrogels of laponite: PVA-Alginate as a potential wound healing material. Carbohydrate polymers 176, 392-401.

González-Henríquez, C.M., Sarabia-Vallejos, M.A., Rodriguez-Hernandez, J., 2019. Polymers for additive manufacturing and 4D-printing: Materials, methodologies, and biomedical applications. Progress in Polymer Science 94, 57-116.

Griffin, M., Leung, B., Premakumar, Y., Szarko, M., Butler, P., 2017. Comparison of the mechanical properties of different skin sites for auricular and nasal reconstruction. Journal of Otolaryngology-Head & Neck Surgery 46(1), 1-6.

Gültan, T., Yurtsever, M.Ç., Gümüşderelioğlu, M., 2020. NaOH-etched/boron-doped nanohydroxyapatite-coated PEEK implants enhance the proliferation and differentiation of osteogenic cells. Biomedical Materials 15(3), 035019.

Gümüşderelioğlu, M., Tunçay, E.Ö., Kaynak, G., Demirtaş, T.T., Aydın, S.T., Hakkı, S.S., 2015. Encapsulated boron as an osteoinductive agent for bone scaffolds. Journal of Trace Elements in Medicine and Biology 31, 120-128.

Gurtner, G.C., Werner, S., Barrandon, Y., Longaker, M.T., 2008. Wound repair and regeneration. Nature 453(7193), 314-321.

Haider, A., Kwak, S., Gupta, K.C., Kang, I.-K., 2015. Antibacterial activity and cytocompatibility of PLGA/CuO hybrid nanofiber scaffolds prepared by electrospinning. Journal of Nanomaterials 2015.

Halbus, A.F., Horozov, T.S., Paunov, V.N., 2019. Strongly enhanced antibacterial action of copper oxide nanoparticles with boronic acid surface functionality. ACS applied materials & interfaces 11(13), 12232-12243.

Hong, Y., Zhou, F., Hua, Y., Zhang, X., Ni, C., Pan, D., Zhang, Y., Jiang, D., Yang, L., Lin, Q., 2019. A strongly adhesive hemostatic hydrogel for the repair of arterial and heart bleeds. Nature communications 10(1), 1-11.

Jaffar Al-Mulla, E.A., 2011. Preparation of new polymer nanocomposites based on poly (lactic acid)/fatty nitrogen compounds modified clay by a solution casting process. Fibers and Polymers 12(4), 444-450.

Jedrzejczak-Silicka, M., Trukawka, M., Piotrowska, K., Mijowska, E., 2020. Few-Layered Hexagonal Boron Nitride: Functionalization, Nanocomposites, and Physicochemical and Biological Properties. Biochemical Toxicology-Heavy Metals and Nanomaterials. IntechOpen.

Jeong, J.H., Liang, Y., Jang, M., Cha, C., Chu, C., Lee, H., Jung, W., Kim, J.W., Boppart, S.A., Kong, H., 2013. Stiffness-modulated water retention and neovascularization of dermal fibroblast-encapsulating collagen gel. Tissue Engineering Part A 19(11-12), 1275-1284.

Ji, Y., Ghosh, K., Li, B., Sokolov, J.C., Clark, R.A., Rafailovich, M.H., 2006. Dual-syringe reactive electrospinning of cross-linked hyaluronic acid hydrogel nanofibers for tissue engineering applications. Macromolecular bioscience 6(10), 811-817.

Jung, S., Day, T., Boone, T., Buziak, B., Omar, A., 2019. Anti-biofilm activity of two novel, borate based, bioactive glass wound dressings. Biomedical glasses 5(1), 67-75.

Kalra, A., Lowe, A., Al-Jumaily, A., 2016. Mechanical behaviour of skin: a review. J. Mater. Sci. Eng 5(4), 1000254.

Khalili, P., Liu, X., Tshai, K.Y., Rudd, C., Yi, X., 2019. Development of fire retardancy of natural fiber composite encouraged by a synergy between zinc borate and ammonium polyphosphate. Composites Part B: Engineering 159, 165-172.

Kim, A., Lee, H., Jones, C.F., Mujumdar, S.K., Gu, Y., Siegel, R.A., 2017. Swelling, mechanics, and thermal/chemical stability of hydrogels containing phenylboronic acid side chains. Gels 4(1), 4.

Kim, H.S., Sun, X., Lee, J.-H., Kim, H.-W., Fu, X., Leong, K.W., 2019. Advanced drug delivery systems and artificial skin grafts for skin wound healing. Advanced drug delivery reviews 146, 209-239.

Kıvanç, M., Barutca, B., Koparal, A.T., Göncü, Y., Bostancı, S.H., Ay, N., 2018. Effects of hexagonal boron nitride nanoparticles on antimicrobial and antibiofilm activities, cell viability. Materials Science and Engineering: C 91, 115-124.

Koç, S., Çakmak, S., Gümüşderelioğlu, M., Ertekin, T.S., Çalış, M., Yılmaz, M.M., Akcan, G., Çaylı, S., 2021. Three dimensional nanofibrous and compressible poly (L-lactic acid) bone grafts loaded with platelet-rich plasma. Biomedical Materials 16(4), 045012.

Kozak, M., Domka, L., 2004. Adsorption of the quaternary ammonium salts on montmorillonite. Journal of Physics and Chemistry of Solids 65(2-3), 441-445.

Laurano, R., Boffito, M., Ciardelli, G., Chiono, V., 2022. Wound Dressing Products: a Translational Investigation from the Bench to the Market. Engineered Regeneration.

Lee, H., Dellatore, S.M., Miller, W.M., Messersmith, P.B., 2007. Mussel-inspired surface chemistry for multifunctional coatings. science 318(5849), 426-430.

Lee, J.W., Kim, M.H., Choi, W.M., Park, O.O., 2006. Effects of organoclay modification on microstructure and properties of polypropylene–organoclay nanocomposites. Journal of applied polymer science 99(4), 1752-1759.

Lin, P.-H., Sermersheim, M., Li, H., Lee, P.H., Steinberg, S.M., Ma, J., 2017. Zinc in wound healing modulation. Nutrients 10(1), 16.

Liu, W., Huang, C., Jin, X., 2015. Electrospinning of grooved polystyrene fibers: effect of solvent systems. Nanoscale research letters 10(1), 1-10.

Lou, D., Pang, Q., Pei, X., Dong, S., Li, S., Tan, W.-q., Ma, L., 2020. Flexible wound healing system for pro-regeneration, temperature monitoring and infection early warning. Biosensors and Bioelectronics 162, 112275.

Lu, J., Zhuang, W., Li, L., Zhang, B., Yang, L., Liu, D., Yu, H., Luo, R., Wang, Y., 2019. Micelle-embedded layer-by-layer coating with catechol and phenylboronic acid for tunable drug loading, sustained release, mild tissue response, and selective cell fate for re-endothelialization. ACS applied materials & interfaces 11(10), 10337-10350.

Malachová, K., Praus, P., Pavlíčková, Z., Turicová, M., 2009. Activity of antibacterial compounds immobilised on montmorillonite. Applied Clay Science 43(3-4), 364-368.

Malachová, K., Praus, P., Rybková, Z., Kozák, O., 2011. Antibacterial and antifungal activities of silver, copper and zinc montmorillonites. Applied Clay Science 53(4), 642-645.

Marasovic, M., Ivankovic, S., Stojkovic, R., Djermic, D., Galic, B., Milos, M., 2017. In vitro and in vivo antitumour effects of phenylboronic acid against mouse mammary adenocarcinoma 4T1 and squamous carcinoma SCCVII cells. Journal of enzyme inhibition and medicinal chemistry 32(1), 1299-1304.

Morgado, P.I., Lisboa, P.F., Ribeiro, M.P., Miguel, S.P., Simões, P.C., Correia, I.J., Aguiar-Ricardo, A., 2014. Poly (vinyl alcohol)/chitosan asymmetrical membranes: Highly controlled morphology toward the ideal wound dressing. Journal of membrane science 469, 262-271.

Mousa, M., Evans, N.D., Oreffo, R.O., Dawson, J.I., 2018. Clay nanoparticles for regenerative medicine and biomaterial design: A review of clay bioactivity. Biomaterials 159, 204-214.

Müller, K., Bugnicourt, E., Latorre, M., Jorda, M., Echegoyen Sanz, Y., Lagaron, J.M., Miesbauer, O., Bianchin, A., Hankin, S., Bölz, U., Pérez, G., Jesdinszki, M., Lindner, M., Scheuerer, Z., Castelló, S., Schmid, M., 2017. Review on the Processing and Properties of Polymer Nanocomposites and Nanocoatings and Their Applications in the Packaging, Automotive and Solar Energy Fields. Nanomaterials 7(4), 74.

Murugesan, S., Scheibel, T., 2020. Copolymer/clay nanocomposites for biomedical applications. Advanced Functional Materials 30(17), 1908101.

Mushtaq, M., Saba, H., Wang, W., Naeem, M.A., Wei, Q., 2020. Fabrication and characterization of electrospun membranes from poly (lactic acid) and hexadecyl

trimethyl ammonium chloride-modified montmorillonite clay. Journal of Industrial Textiles 50(3), 415-424.

Naseri, E., Ahmadi, A., 2022. A review on wound dressings: antimicrobial agents, biomaterials, fabrication techniques, and stimuli-responsive drug release. European Polymer Journal, 111293.

Neto, W.A.R., Pereira, I.H., Ayres, E., de Paula, A.C., Averous, L., Góes, A.M., Oréfice, R.L., Bretas, R.E.S., 2012. Influence of the microstructure and mechanical strength of nanofibers of biodegradable polymers with hydroxyapatite in stem cells growth. Electrospinning, characterization and cell viability. Polymer degradation and stability 97(10), 2037-2051.

Nim, B., Sreearunothai, P., Petchsuk, A., Opaprakasit, P., 2018. Preparation of TiO2-loaded electrospun fibers of polylactide/poly (vinylpyrrolidone) blends for use as catalysts in epoxidation of unsaturated oils. Journal of Nanoparticle Research 20(4), 1-15.

Nzietchueng, R.M., Dousset, B., Franck, P., Benderdour, M., Nabet, P., Hess, K., 2002. Mechanisms implicated in the effects of boron on wound healing. Journal of trace elements in medicine and biology 16(4), 239-244.

Op't Veld, R.C., Walboomers, X.F., Jansen, J.A., Wagener, F.A., 2020. Design considerations for hydrogel wound dressings: strategic and molecular advances. Tissue Engineering Part B: Reviews 26(3), 230-248.

Opalenik, S.R., Davidson, J.M., 2005. Fibroblast differentiation of bone marrow-derived cells during wound repair. The FASEB Journal 19(11), 1561-1563.

Ozbek, B., Erdogan, B., Ekren, N., Oktar, F.N., Akyol, S., Ben-Nissan, B., Sasmazel, H.T., Kalkandelen, C., Mergen, A., Kuruca, S.E., 2018. Production of the novel fibrous structure of poly (ε-caprolactone)/tri-calcium phosphate/hexagonal boron nitride composites for bone tissue engineering. Journal of the Australian Ceramic Society 54(2), 251-260.

Padmavathy, N., Vijayaraghavan, R., 2008. Enhanced bioactivity of ZnO nanoparticles—an antimicrobial study. Science and technology of advanced materials.

Palak, H., Aktürk, B., Kayaoğlu, B.K., Göcek, İ., 2021. Fabrication of montmorillonite nanoclay-loaded electrospun nanofibrous mats for UV protection. Journal of Industrial Textiles, 15280837211020826.

Pan, G., Guo, B., Ma, Y., Cui, W., He, F., Li, B., Yang, H., Shea, K.J., 2014. Dynamic introduction of cell adhesive factor via reversible multicovalent phenylboronic acid/cis-

diol polymeric complexes. Journal of the American Chemical Society 136(17), 6203-6206.

Pandit, S., Gaska, K., Mokkapati, V., Forsberg, S., Svensson, M., Kádár, R., Mijakovic, I., 2019. Antibacterial effect of boron nitride flakes with controlled orientation in polymer composites. RSC advances 9(57), 33454-33459.

Pang, Q., Lou, D., Li, S., Wang, G., Qiao, B., Dong, S., Ma, L., Gao, C., Wu, Z., 2020. Smart flexible electronics-integrated wound dressing for real-time monitoring and on-demand treatment of infected wounds. Advanced Science 7(6), 1902673.

Percival, N.J., 2002. Classification of wounds and their management. Surgery (Oxford) 20(5), 114-117.

Poyraz, Ş., Altınışık, Z., Çakmak, A.S., Şimşek, M., Gümüşderelioğlu, M., 2022. Random/aligned electrospun PCL fibrous matrices with modified surface textures: Characterization and interactions with dermal fibroblasts and keratinocytes. Colloids and Surfaces B: Biointerfaces 218, 112724.

Qiao, Z., Lv, X., He, S., Bai, S., Liu, X., Hou, L., He, J., Tong, D., Ruan, R., Zhang, J., 2021. A mussel-inspired supramolecular hydrogel with robust tissue anchor for rapid hemostasis of arterial and visceral bleedings. Bioactive materials 6(9), 2829-2840.

Qiu, J., Liu, D., Wang, Y., Chen, G., Jiang, S., Li, G., Wang, Y., Wang, W., Wu, P., Liu, X., 2020. Comprehensive characterization of the structure and gel property of organo-montmorillonite: effect of layer charge density of montmorillonite and carbon chain length of alkyl ammonium. Minerals 10(4), 378.

Ramazani, S.A., Rahimi, A., Frounchi, M., Radman, S., 2008. Investigation of flame retardancy and physical–mechanical properties of zinc borate and aluminum hydroxide propylene composites. Materials & Design 29(5), 1051-1056.

Ramesh, P., Prasad, B.D., Narayana, K., 2020. Effect of MMT clay on mechanical, thermal and barrier properties of treated aloevera fiber/PLA-hybrid biocomposites. Silicon 12(7), 1751-1760.

Rashid, T.U., Gorga, R.E., Krause, W.E., 2021. Mechanical properties of electrospun fibers—A critical review. Advanced Engineering Materials 23(9), 2100153.

Ray, C.G., Ryan, K.J., 2010. Sherris medical microbiology. McGraw-Hill.

Rezvani Ghomi, E., Khalili, S., Nouri Khorasani, S., Esmaeely Neisiany, R., Ramakrishna, S., 2019. Wound dressings: Current advances and future directions. Journal of Applied Polymer Science 136(27), 47738.

Robson, M.C., Ortiz, R.T., Moffatt, L.T., Jordan, M.H., Shupp, J.W., Ochs, D., Uberti, M.G., Donate, G.A., Abercrombie, M., Wolvos, T., 2012. Innovations for wound bed preparation: the role of Drawtex hydroconductive dressings. Proceedings of a Symposium of Investigators.

Rousselle, P., Braye, F., Dayan, G., 2019. Re-epithelialization of adult skin wounds: Cellular mechanisms and therapeutic strategies. Advanced Drug Delivery Reviews 146, 344-365.

Sanusi, O.M., Benelfellah, A., Bikiaris, D.N., Ait Hocine, N., 2021. Effect of rigid nanoparticles and preparation techniques on the performances of poly (lactic acid) nanocomposites: A review. Polymers for Advanced Technologies 32(2), 444-460.

Seaman, S., 2002. Dressing Selection in Chronic Wound Management. Journal of the American Podiatric Medical Association 92(1), 24-33.

Şen, Ö., Emanet, M., Çulha, M., 2018. One-step synthesis of hexagonal boron nitrides, their crystallinity and biodegradation. Frontiers in bioengineering and biotechnology 6, 83.

Şen, O.z., Emanet, M., Çulha, M., 2019. Stimulatory effect of hexagonal boron nitrides in wound healing. ACS Applied Bio Materials 2(12), 5582-5596.

Sha, D., Xu, J., Yang, X., Xue, Y., Liu, X., Li, C., Wei, M., Liang, Z., Shi, K., Wang, B., 2021. Synthesis and antibacterial activities of quaternary ammonium salts with different alkyl chain lengths grafted on polyvinyl alcohol-formaldehyde sponges. Reactive and Functional Polymers 158, 104797.

Shao, M., Fan, Y., Zhang, K., Hu, Y., Xu, F.-J., 2021. One nanosystem with potent antibacterial and gene-delivery performances accelerates infected wound healing. Nano Today 39, 101224.

Shen, D., Yu, H., Wang, L., Chen, X., Feng, J., Zhang, Q., Xiong, W., Pan, J., Han, Y., Liu, X., 2021. Biodegradable phenylboronic acid-modified ε-polylysine for glucose-responsive insulin delivery via transdermal microneedles. Journal of Materials Chemistry B 9(30), 6017-6028.

Shen, W., Wu, W., Liu, C., Wang, Y., Zhang, X., 2020. Thermal conductivity enhancement of PLA/TPU/BN composites by controlling BN distribution and annealing treatment. Plastics, Rubber and Composites 49(5), 204-213.

Sheng, L., Zhang, Z., Zhang, Y., Wang, E., Ma, B., Xu, Q., Ma, L., Zhang, M., Pei, G., Chang, J., 2021. A novel “hot spring”-mimetic hydrogel with excellent angiogenic properties for chronic wound healing. Biomaterials 264, 120414.

Siebert, L., Luna-Cerón, E., García-Rivera, L.E., Oh, J., Jang, J., Rosas-Gómez, D.A., Pérez-Gómez, M.D., Maschkowitz, G., Fickenscher, H., Oceguera-Cuevas, D., 2021. Light-Controlled Growth Factors Release on Tetrapodal ZnO-Incorporated 3D-Printed Hydrogels for Developing Smart Wound Scaffold. Advanced Functional Materials 31(22), 2007555.

Silva, M.M.P., Aguiar, M.I.F.d., Rodrigues, A.B., Miranda, M.D.C., Araújo, M.Â.M., Rolim, I.L.T.P., 2018. The use of nanoparticles in wound treatment: a systematic review. Revista da Escola de Enfermagem da USP 51.

Sood, A., Granick, M.S., Tomaselli, N.L., 2014. Wound dressings and comparative effectiveness data. Advances in wound care 3(8), 511-529.

Stloukal, P., Pekařová, S., Kalendova, A., Mattausch, H., Laske, S., Holzer, C., Chitu, L., Bodner, S., Maier, G., Slouf, M., 2015. Kinetics and mechanism of the biodegradation of PLA/clay nanocomposites during thermophilic phase of composting process. Waste management 42, 31-40.

Sun, H., Zhang, J., Li, L., Xu, J., Sun, D., 2013. Surface modification of natural Na-montmorillonite in alkane solvents using a quaternary ammonium surfactant. Colloids and Surfaces A: Physicochemical and Engineering Aspects 426, 26-32.

Szewczyk, P.K., Stachewicz, U., 2020. The impact of relative humidity on electrospun polymer fibers: From structural changes to fiber morphology. Advances in Colloid and Interface Science 286, 102315.

Tarhan, T., Şen, Ö., Ciofani, M.E., Yılmaz, D., Çulha, M., 2021. Synthesis and characterization of silver nanoparticles decorated polydopamine coated hexagonal boron nitride and its effect on wound healing. Journal of Trace Elements in Medicine and Biology 67, 126774.

Tarus, B.K., Fadel, N., Al-Oufy, A., El-Messiry, M., 2020. Investigation of mechanical properties of electrospun poly (vinyl chloride) polymer nanoengineered composite. Journal of Engineered Fibers and Fabrics 15, 1558925020982569.

Tavakoli, S., Klar, A.S., 2020. Advanced hydrogels as wound dressings. Biomolecules 10(8), 1169.

Tottoli, E.M., Dorati, R., Genta, I., Chiesa, E., Pisani, S., Conti, B., 2020. Skin wound healing process and new emerging technologies for skin wound care and regeneration. Pharmaceutics 12(8), 735.

Tunçay, E.Ö., Demirtaş, T.T., Gümüşderelioğlu, M., 2017. Microwave-induced production of boron-doped HAp (B-HAp) and B-HAp coated composite scaffolds. Journal of Trace Elements in Medicine and Biology 40, 72-81.

Ul-Islam, M., Khan, T., Khattak, W.A., Park, J.K., 2013. Bacterial cellulose-MMTs nanoreinforced composite films: novel wound dressing material with antibacterial properties. Cellulose 20(2), 589-596.

Velnar, T., Bailey, T., Smrkolj, V., 2009. The wound healing process: an overview of the cellular and molecular mechanisms. Journal of international medical research 37(5), 1528-1542.

Wang, B., Wang, X., Lou, W., Hao, J., 2012. Thermal conductivity and rheological properties of graphite/oil nanofluids. Colloids and Surfaces A: Physicochemical and Engineering Aspects 414, 125-131.

Wang, D., Zhang, N., Meng, G., He, J., Wu, F., 2020. The effect of form of carboxymethyl-chitosan dressings on biological properties in wound healing. Colloids and Surfaces B: Biointerfaces 194, 111191.

Wang, H., You, W., Wu, B., Nie, X., Xia, L., Wang, C., You, Y.-Z., 2022. Phenylboronic acid-functionalized silver nanoparticles for highly efficient and selective bacterial killing. Journal of Materials Chemistry B 10(15), 2844-2852.

Wang, J., Ma, F., Sun, M., 2017. Graphene, hexagonal boron nitride, and their heterostructures: properties and applications. RSC advances 7(27), 16801-16822.

Wang, M., Wang, C., Chen, M., Xi, Y., Cheng, W., Mao, C., Xu, T., Zhang, X., Lin, C., Gao, W., 2019. Efficient angiogenesis-based diabetic wound healing/skin reconstruction through bioactive antibacterial adhesive ultraviolet shielding nanodressing with exosome release. Acs Nano 13(9), 10279-10293.

Wang, S., Wen, B., 2022. Effect of functional filler morphology on the crystallization behavior and thermal conductivity of PET resin: A comparative study of three different shapes of BN as heterogeneous nucleating agents. Composites Science and Technology 222, 109346.

Whitney, J.D., 2005. Overview: acute and chronic wounds. Nursing Clinics 40(2), 191-205.

Xie, W., Gao, Z., Pan, W.-P., Hunter, D., Singh, A., Vaia, R., 2001. Thermal degradation chemistry of alkyl quaternary ammonium montmorillonite. Chemistry of materials 13(9), 2979-2990.

Xie, Y., He, Y., Irwin, P.L., Jin, T., Shi, X., 2011. Antibacterial activity and mechanism of action of zinc oxide nanoparticles against Campylobacter jejuni. Applied and environmental microbiology 77(7), 2325-2331.

YALÇINKAYA, S.E., Yildiz, N., Sacak, M., Calimli, A., 2010. Preparation of polystyrene/montmorillonite nanocomposites: optimization by response surface methodology (RSM). Turkish Journal of Chemistry 34(4), 581-592.

Yang, W., Sherman, V.R., Gludovatz, B., Schaible, E., Stewart, P., Ritchie, R.O., Meyers, M.A., 2015. On the tear resistance of skin. Nature communications 6(1), 1-10.

Yang, Y., Zhang, H., Zeng, F., Jia, Q., Zhang, L., Yu, A., Duan, B., 2022. A quaternized chitin derivatives, egg white protein and montmorillonite composite sponge with antibacterial and hemostatic effect for promoting wound healing. Composites Part B: Engineering 234, 109661.

Yang, Z., Wang, W., Tai, X., Wang, G., 2019. Preparation of modified montmorillonite with different quaternary ammonium salts and application in Pickering emulsion. New Journal of Chemistry 43(29), 11543-11548.

Younis, A., 2022. Evaluation flammability, mechanical and electrical properties of polypropylene after using zinc borates and montmorillonite. Journal of Thermoplastic Composite Materials 35(2), 177-191.

Yu, B., Xing, W., Guo, W., Qiu, S., Wang, X., Lo, S., Hu, Y., 2016. Thermal exfoliation of hexagonal boron nitride for effective enhancements on thermal stability, flame retardancy and smoke suppression of epoxy resin nanocomposites via sol–gel process. Journal of Materials Chemistry A 4(19), 7330-7340.

Yu, C., Gao, H., Li, Q., Cao, X., 2020. Injectable dual cross-linked adhesive hyaluronic acid multifunctional hydrogel scaffolds for potential applications in cartilage repair. Polymer Chemistry 11(18), 3169-3178.

Zeng, Q., Qi, X., Shi, G., Zhang, M., Haick, H., 2022. Wound Dressing: From Nanomaterials to Diagnostic Dressings and Healing Evaluations. ACS nano 16(2), 1708-1733.

Zeng, Y., Zhu, C., Tao, L., 2021. Stimuli-Responsive Multifunctional Phenylboronic Acid Polymers Via Multicomponent Reactions: From Synthesis to Application. Macromolecular Rapid Communications 42(18), 2100022.

Zhang, J., Song, M., Wang, X., Wu, J., Yang, Z., Cao, J., Chen, Y., Wei, Q., 2016. Preparation of a cellulose acetate/organic montmorillonite composite porous ultrafine

fiber membrane for enzyme immobilization. Journal of Applied Polymer Science 133(33).

Zhong, Y., Xiao, H., Seidi, F., Jin, Y., 2020. Natural polymer-based antimicrobial hydrogels without synthetic antibiotics as wound dressings. Biomacromolecules 21(8), 2983-3006.

Zhou, C., Tong, D., Yu, W., 2019. Smectite nanomaterials: preparation, properties, and functional applications. Nanomaterials from Clay Minerals, pp. 335-364. Elsevier.

Zhou, Q., Xanthos, M., 2009. Nanosize and microsize clay effects on the kinetics of the thermal degradation of polylactides. Polymer Degradation and Stability 94(3), 327-338.

Zhou, T., Wang, N., Xue, Y., Ding, T., Liu, X., Mo, X., Sun, J., 2016. Electrospun tilapia collagen nanofibers accelerating wound healing via inducing keratinocytes proliferation and differentiation. Colloids and Surfaces B: Biointerfaces 143, 415-422.